

POLITECNICO DI MILANO
Scuola di Ingegneria Industriale e dell'Informazione
Corso di Laurea Magistrale in Ingegneria Chimica



POLITECNICO
MILANO 1863

**Effectiveness of the passivation treatment of a cobalt-based
catalyst active in the Fischer-Tropsch synthesis**

Relatore: Prof. Enrico Tronconi

Co-relatore: Dr. Ing. Laura Fratolocchi

Prof. Luca Lietti

Candidato: Barbara Boccia

Matricola: 876381

Anno Accademico 2017/2018



The project leading to this Thesis has received funding from the European Research Council under Grant Agreement no. 694910 (INTENT).

Index

<i>Preface</i>	1
<i>Chapter 1: Introduction</i>	3
<i>1.1 Energy Scenario</i>	3
<i>1.1.1 Energy Outlook to 2040</i>	4
<i>1.1.2 Fulfilling the need for future supplies</i>	6
<i>1.2 Fischer-Tropsch Synthesis</i>	11
<i>1.2.1 History</i>	11
<i>1.2.2 Active Catalysts</i>	14
<i>1.2.3 Chemistry</i>	16
<i>1.2.3.1 Main Side Reactions</i>	17
<i>1.2.3.2 Mechanism</i>	18
<i>1.2.4 Product distribution</i>	25
<i>1.2.5 Influence of process conditions on the selectivity</i>	34
<i>1.2.6 LTFT and HTFT operations</i>	36
<i>1.2.7 FT reactors</i>	38
<i>1.2.7.1 Multi-tubular fixed bed reactor (MTFBR)</i>	39
<i>1.2.7.2 Circulating fluidized bed reactor (CFBR)</i>	41
<i>1.2.7.3 Slurry bubble column reactor</i>	43
<i>1.2.8 Overview of industrial Fischer-Tropsch processes</i>	44
<i>1.2.8.1 Processes based on conventional reactors</i>	45
<i>1.2.8.2 Processes based on unconventional reactors</i>	49
<i>Bibliography</i>	54
<i>Chapter 2: State of Art</i>	57
<i>2.1 FT catalysts</i>	58
<i>2.1.1 Cobalt-based catalysts</i>	59
<i>2.1.2 Composition of industrial Co-based catalysts</i>	61
<i>2.2 Cobalt oxidation</i>	63
<i>2.3 Reduction</i>	80

2.4 Passivation	82
Bibliografy	91
Chapter 3: Lab-Scale Rig and Experimental Procedures	96
3.1 Fixed bed lab-scale rig	96
3.1.1 Feed zone	97
3.1.2 Reaction zone	101
3.1.3 Product analysis zone	102
3.2 Experimental procedures	108
3.2.1 Catalyst preparation	108
3.2.2 Reactor preparation	109
3.2.3 Catalyst reduction and passivation	109
3.3 Catalyst characterization	110
3.3.1 ICP-MS	110
3.3.2 BET	110
3.3.3 XRD	111
3.3.5 H₂-Chemisorption	113
Chapter 4: Results and Discussion	114
4.1 Characterization of the calcined Co/Pt/Al₂O₃^(s) catalyst	114
4.2 Characterization of the catalyst reduced at 400 and 300 °C	119
4.3 Catalyst passivation	121
4.4 Catalytic testing at high pressure lab-scale FT plant	130
Bibliography	134
Conclusions	135

Preface

In a worldwide scenario characterized by a constant increase in energy demand, the interest in XtL (X to Liquids) processes is considerably growing. These processes convert natural gas (GtL), coal (CtL) or biomasses (BtL) into high molecular weight hydrocarbons. The Fischer–Tropsch synthesis (FTS) is the key technology in providing synthetic hydrocarbon fuels and chemicals from coal, natural gas, and biomass. Virtually, any source of (hydro)carbon feedstock can be converted into a mixture of synthesis gas (CO and H₂). The FTS is the reaction from synthesis gas to predominantly straight-chain hydrocarbons, such as paraffins (from CH₄ to waxes, C_nH_{2n+2} with n=1, ...,100), olefins (from ethylene to longer molecules, C_nH_{2n} with n>2)). The low temperature Fischer-Tropsch (LTFT) synthesis is the key technology of the GtL processes and is the subject of this thesis. GtL fuels offer significant environmental benefits over the fuels derived from crude oil. In fact, they are free of nitrogen, sulphur, aromatics and metals. This low-emission, premium-grade fuel can be used either “pure” or as a fuel additive in diesel engines. Furthermore, GtL diesel can be used in existing vehicles and fuel delivery systems without modifications. GtL fuels have boosted performances (high cetane number). The more used catalyst for operations between 200 and 240 °C, (Low Temperature Fischer-Tropsch synthesis, LTFT) is the Co-based catalyst, which favours the formation of heavier hydrocarbons (e.g., waxes) that can be upgraded to the diesel and jet fuel range. The WGS activity of Co-based catalysts is low with this type of catalyst and its selectivity to the higher hydrocarbons is high. Cobalt is an expensive material and thus it is important to obtain a suitable dispersion on the catalytic support. The activity in the FTS is strongly related to the number of Co⁰ surface sites. The amounts of Co⁰ sites is influenced by the activation procedure, the addition of promoters, the type of support and the several pre-treatments used, as calcination, reduction and passivation. The catalyst support used in this thesis work is γ -Al₂O₃ stabilized with inactive CoAl₂O₄ species and promoted with Pt. The catalyst is obtained by incipient wetness impregnation (IWI) and consecutive calcination at high temperature in static air. Then, the catalyst is reduced under a flow of pure hydrogen at 400°C. The passivation treatment is then studied on the reduced sample. The passivated catalyst has a protective thin film of Co oxides covering the metallic catalyst surface that

allows its storage in air atmosphere for several days without any changes of the catalyst morphology and grants, at the same time, its re-reduction at lower temperatures. This manuscript is divided into five sections:

- Chapter 1: an introduction to the world energy scenario is presented, followed by a general overview of the Gas to Liquids process and in particular a description of the FT process in its fundamental aspects is offered.
- Chapter 2: an overview on the cobalt based catalysts used for the FTS and on the cobalt oxidation, reduction and passivation processes is given.
- Chapter 3: a description of the laboratory plant used to conduct the experimental tests described in this work is presented. Furthermore, all the procedures used for the management of the plant and the methods for analysing the reaction products are described.
- Chapter 4: the characterization of the used catalyst samples and the results linked to reduction and passivation procedures are discussed in this chapter.
- Conclusions: the most important conclusions of this thesis work are shown.

Chapter 1

Introduction

1.1 Energy Scenario

Up until the last decades of the XIX century, coal used to be the most important worldwide source of energy. It was used for both domestic and industrial purposes and as a fuel for the civil and military industry. From the beginning of the XX century, oil has gradually replaced coal as the primary source of energy. Expansion and development in the transportation sector combined with industrial growth and increasing urbanization have created the need for an energy source characterized by a high specific energy content and a better environmental compatibility with respect to coal: liquid fuels. Today approximately 85% of the energy demand still comes from fossil fuels. Due to multiple factors such as technological progress, population growth and middle-class expansion, energy demand is expected to significantly increase in the coming years thus creating more issues related to sources, efficiency and delivery of energy. Furthermore, this century has seen tremendous advances in energy technology, including those that unlocked North America's vast resources of unconventional oil and gas, thereby ushering an era of energy abundance and diversity. Along with these matters, other issues regard the environmental problems, with CO₂ emissions that will probably peak around 2030. Therefore, how to provide additional energy and to deliver it in a global market with both economic and environmental sustainability is one of the most crucial challenges of this century; since a lot of this depends on scientific development and technological skills as well as social and political matters, it is a question of interest for everyone on this planet.

1.1.1 Energy Outlook to 2040

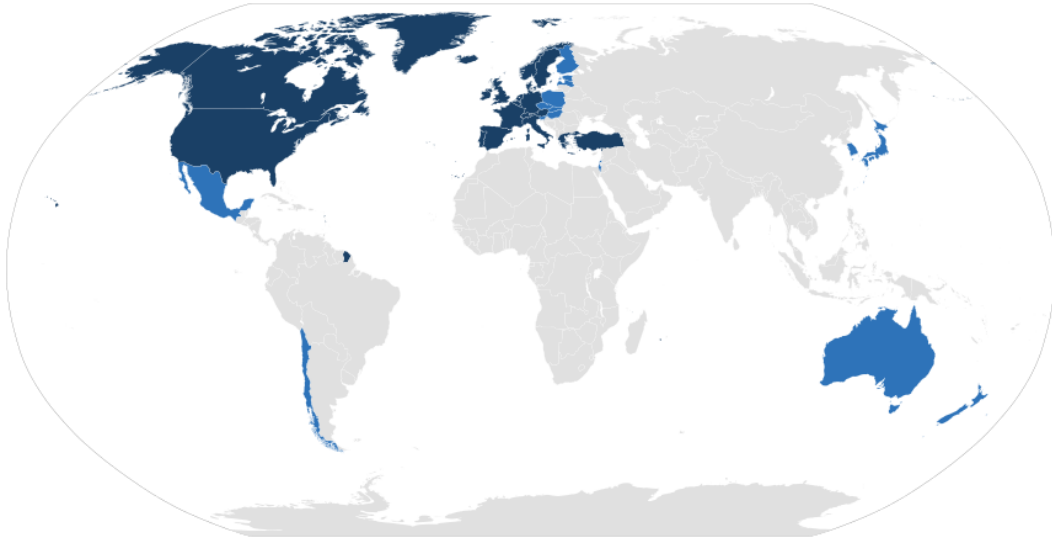


Figure 1. List of OECD countries (dark blue: founding member countries, 1961; light blue: others member).

(1)

In order to have better knowledge of the energy challenge, it is essential to understand ongoing scenarios and to predict, as closely as possible, future trends with an outlook on the next decades.

The period going from now to 2040 is expected to reflect a dramatic expansion of the world's population and the global middle class. Improvement in living conditions will give millions of people access to electricity and global demand is expected to rise by 25%: an equivalent increase to the total energy used in North America and Latin America today. It would have been far higher (exceeding 110%) if we had not foreseen significant improvements in energy efficiency across all sectors. Demand growth is expected to increase by 45% in non-OECD (*Office of Economic Cooperation and Development*) countries while demand in OECD countries will remain essentially the same. As growth is strongly asymmetric, it implies considerable changes in market structure as well as in international policies.

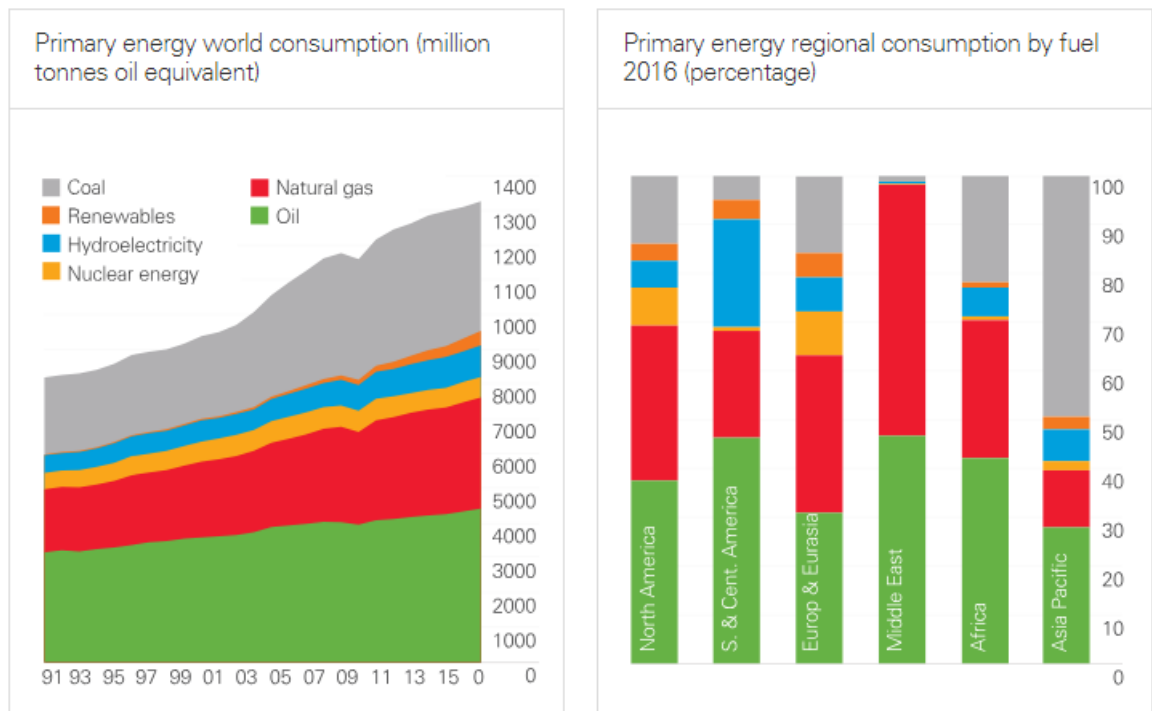


Figure 2. Energy world consumption by fuel. (2)

By 2040 world population is expected to increase up to 9 billion (a 1.8 billion increase as compared to today's figures) and global GDP (*Gross Domestic Product*) more than double. Furthermore, in most regions, those aged under-14 will decrease in number due to declining birth rates and the over-65 population will increase, due to a rise in life expectancy. To keep pace with demand, the world will need to pursue all economic energy sources due to new technologies that will require policies to promote innovation, investment and free commerce. The most important sectors in terms of energy demand are transportation, residential/commercial and industrial. Global energy demand for transportation is forecast to increase by about 30% from 2014 to 2040, essentially due to the contribution of non-OECD countries. Nowadays, there are about 1 billion *light-duty*

vehicles (LDV) in the world, expected to rise to 1.8 billion in the next 25 years, with about 90% of this growth outside the 32 OECD countries. As a result of improved fuel economy, the energy demand for LDVs is expected to peak around 2020 and then decline to nearly 10% in the following 20 years along with the increase of hybrid car market share. Even with an increase in efficiency, combined demand of residential and commercial energy is expected to rise by nearly 25% from 2014 to 2040. A high rise of households in Asia and other developing regions will drive such demand and, as incomes increase, so will the purchase of appliances and air conditioners. For instance, while in 1985 one out of fifty Chinese homes had refrigerators, today more than 80% do. Globally, industrial activity accounts for 30% of primary energy and 50% of electricity demand and it is forecast to rise mostly in two sectors: heavy industry and chemicals, due to rising standards in developing countries. In particular, the production of chemicals is the fastest growing use of energy in the industrial sector.

1.1.2 Fulfilling the need for future supplies

Oil, natural gas and coal are expected to cover almost 80% of the world's energy demand throughout the next 25 years due to their reliability, affordability, versatility, transportability and due to their capability of providing a lot of energy with a relatively low volume. Among them, oil will remain the most used fuel with gas moving into second place ahead of coal. The latter, currently the second-largest fossil fuel resource, is expected to see global demand peak around 2025 and then begin to decline, owing to improved energy efficiency and environmental sustainability in the power generation sector and a switch to fuels with lower CO₂ emissions. By 2040, coal will account for 20% of the global energy demand, down from about 25% in 2014.

Natural gas, on the other hand, is expected to rise to 50% and meet around 40% of the global demand in the same period. Nuclear energy is a pillar of the electricity production in many countries and accounts for about 10% of today's world electricity. As nuclear plants provide electricity with low CO₂ emissions and expanding nuclear capacity would enable nations to diversify their energy supplies, the nuclear sector will see strong gains in the coming decades. The figures have more than doubled since 2014 with China accounting for nearly half of this growth. Modern renewable energy sources - wind, solar and biofuels

– are also growing rapidly and will more than triple from now to 2040. The largest volume growth will come from wind, which by 2040 is expected to supply about 2% of the world’s energy and around 10% of electricity. Together nuclear and renewables are likely to account for almost 40% of the growth in the global energy demand up to 2025. In addition to expanding its supplies, the world is also continuing to enhance its ability of trading energy among different regions. Much of this growth is related to the expanding global LNG (*Liquefied Natural Gas*) network - the liquefaction plants, tankers and re-gasification terminals which enable abundant natural gas to reach markets around the world.

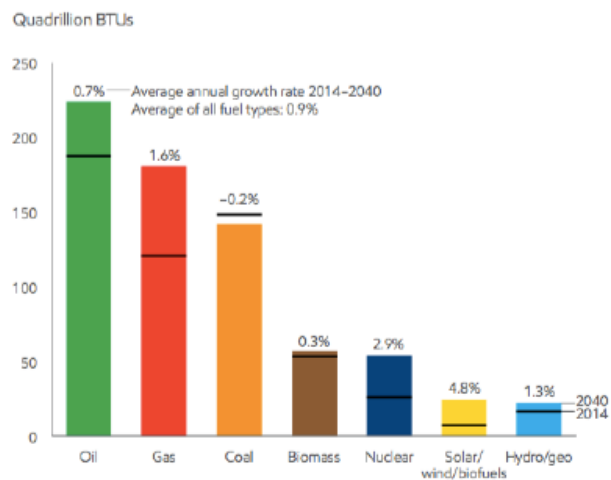


Figure 3. Projection of global fuel demand in 2040. (3)

• LIQUIDS

Global liquid output is seen as rising to 112 MBD (Million Barrels per Day) in 2040, up from 93 MBD in 2014. Most of the growth is expected to come from technology-driven supplies including tight oil, Natural Gas Liquids (NGL), oil sands and deep-water production, reaching 40% of global liquid supply up from 25% today. Despite a decade ago tight oil, dispersed in shale and other tight rock formation, was barely seen on the radar screen, it will probably account for 10% of the world’s liquid production by 2040. Most of this oil will come from North America, the birthplace of the tight oil industry, where crude output has risen by about 75% since then and in 2014 tight liquid production overcame the total production of any other OPEC country except Saudi Arabia. The past few years have seen considerable improvement in the performance of tight oil wells and drilling efficiency; tight oil is now an established and globally competitive source of liquid fuels. Unlike some conventional or more complex projects, tight oil production can also adjust

relatively quickly to changes in demand. The spread of this new technology has and will change the role of North America, once a massive importer and great exporter in few years. By 2040, the number of resources yet to be exploited will still be far higher than the total demand before 2040, even if this rises more than 20%.

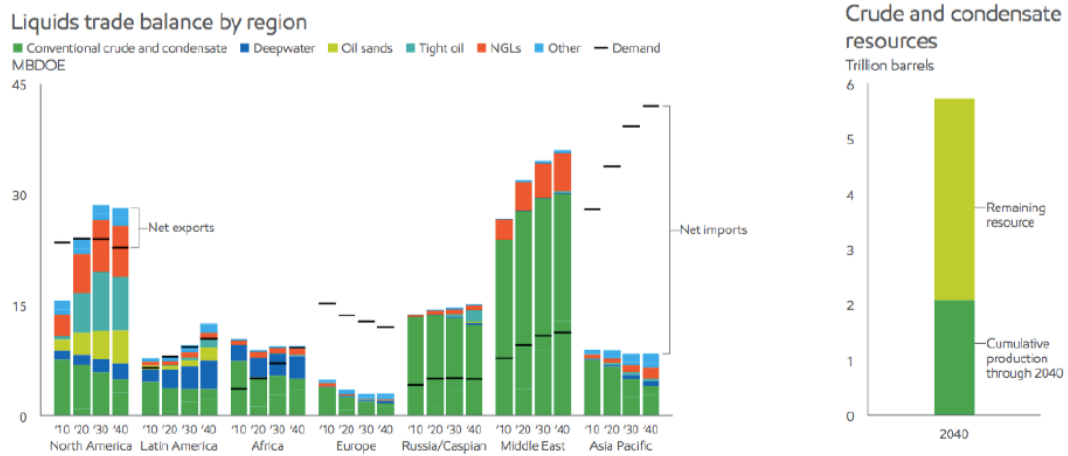


Figure 4. Liquid trade balance and resources. (2)

- **NATURAL GAS**

Global demand for natural gas (NG) is seen as rising by 50% in the next 25 years, faster than any other fossil fuels. The most important reasons are versatility, reduced environmental impact and geographically scattered reservoirs. Natural gas can run generators to produce electricity or it can be directly used in homes, offices and factories simply as a fuel; its very low carbon content makes it an effective and proven tool for curbing CO₂ emissions, particularly in the electricity generation sector. It emits up to 60% less CO₂ than coal and is geographically diverse: North America, Latin America, Russia/Caspian, Asia Pacific, the Middle East and Africa each hold 10% or more of the resources.

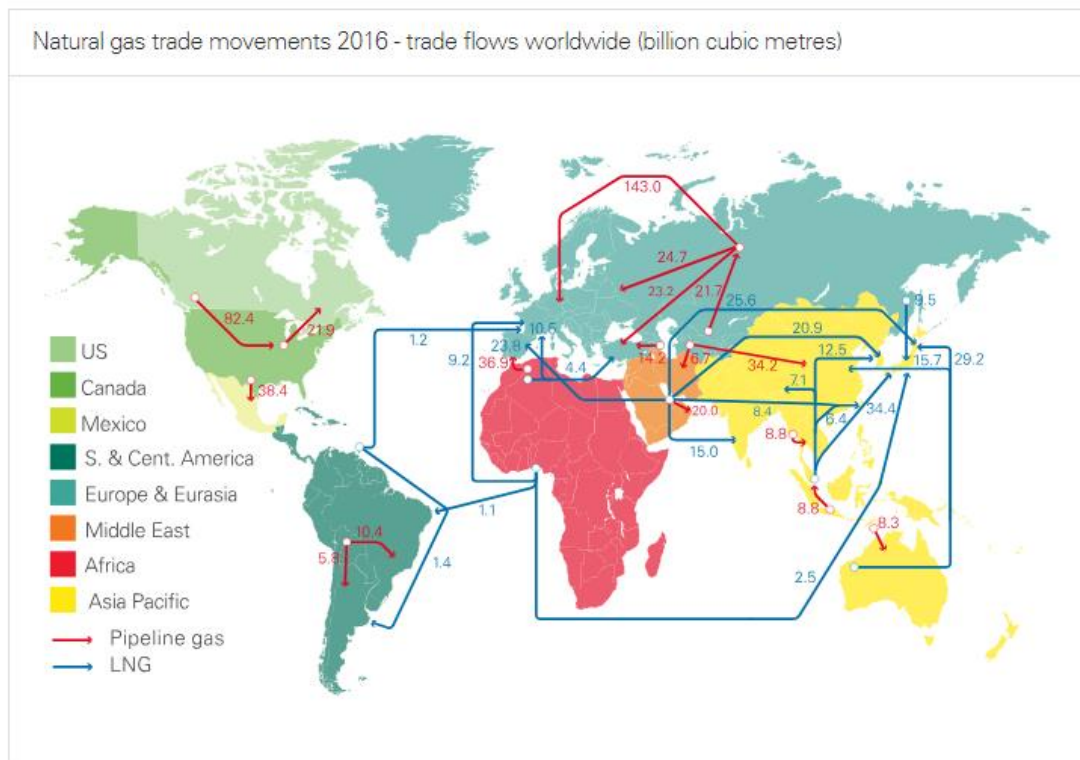


Figure 5. Natural gas trade movements 2016 - trade flows worldwide in billion cubic meters. (2)

Nearly half of the growth in global gas demand through 2040 is expected to be met through interregional trade, most using LNG (*Liquefied Natural Gas*) technology. Until the first LNG shipping and receiving terminals opened in 1964, inter-regional gas trading was confined to areas connected by pipeline. With LNG technology, natural gas can be super-cooled to liquid and safely shipped via tanker to receiving terminals anywhere in the world. LNG exports are expected to triple in the next years and most of which will go to competitive markets in Asia Pacific, followed by United States, East Africa and Australia. Today, around 70% of NG consumption is delivered through pipelines operating at pressures around 80 MPa and flow rates of $106 \text{ Nm}^3 \text{ h}^{-1}$; shipping becomes convenient when distances make the pipeline costs higher than that of liquefaction, transportation and regasification.

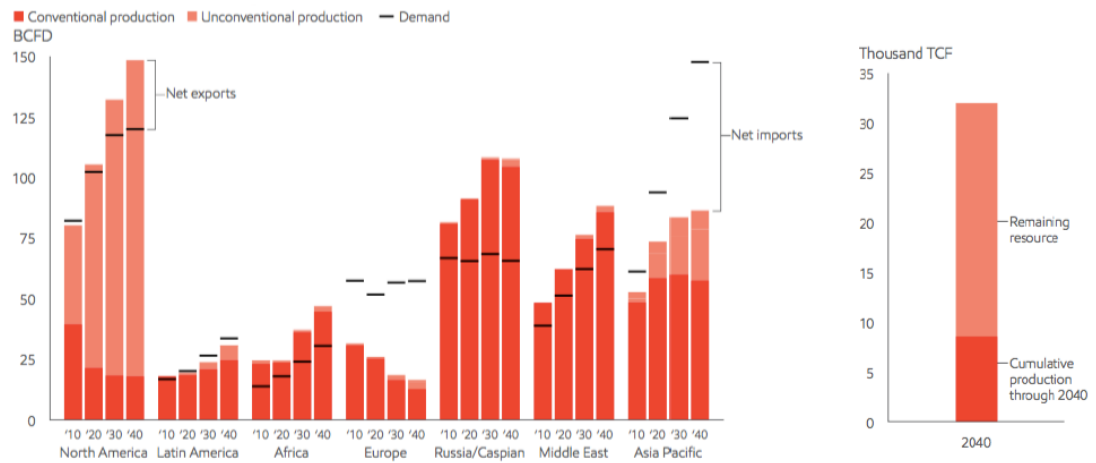


Figure 6. Gas trade by region and natural gas resources. (3)

One further solution to the problem of complete exploitation of NG resources and related transportation is the so-called GTL (*Gas-to-Liquids*) technology. Particularly suitable for small gas reserves, GTL consists of a chemical liquefaction of natural gas which significantly upgrades the economic value of the latter and eases its access to the transportation fuels market. Additionally, it could mitigate some environmental concerns by displacing higher-sulfur fuels, obtained from crude oil, with essentially sulfur-free fuels. Additionally, GTL technology could allow refineries to convert some of their gaseous waste products (*flare gas*) into valuable transportation fuels and lubricants.

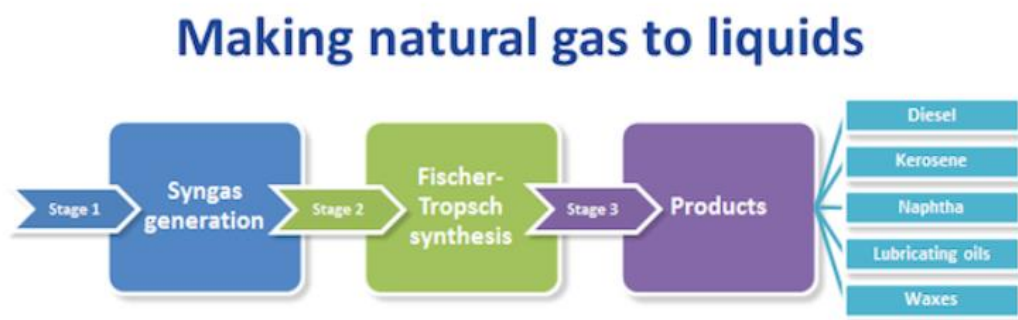


Figure 7. Flow scheme of GTL technology. (4)

Three are the fundamental steps that make up the GTL technology. First natural gas is catalytically converted into a mixture of carbon monoxide and hydrogen, known as *syngas*, via processes as *Partial Oxidation (POX)*, *Autothermal Reforming (ATR)* or *Steam*

Methane Reforming (SMR). Syngas is then converted, in a catalytic reactor, into a mixture of valuable hydrocarbon products. The last stage is cracking or isomerization, which “tailors” the molecule chain into products with desired properties.

Depending on the reaction involved in the second step, four main families can be accounted under the name of GTL technologies:

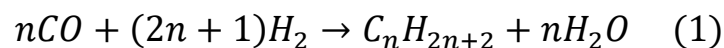
- a. *Gas to Methanol*
- b. *Gas to Olefins*
- c. *Gas to Dimethyl-Ether (DME)*
- d. *Gas to Hydrocarbons*

Fischer-Tropsch synthesis is the core of the Gas to Hydrocarbon technology.

1.2 *Fischer-Tropsch Synthesis*

Fischer-Tropsch synthesis (FTS) is one of the most important and complex processes in the chemical industry. This technology allows indirect liquefaction of carbon sources as coal, natural gas and biomass via syngas production and it is mainly used to synthesize clean (sulfur-free) diesels with high-cetane number (NCFTS = 75 vs NCSTD = 50).

It consists of a catalytic reaction between a mixture of H₂ and CO (syngas) giving liquid long chain hydrocarbons. The general stoichiometry is the following:



Main products are n-paraffins in a range between C₁ and C₆₀₊ (waxes) and n-olefins. The product mixture is triphasic at ambient temperature as it consists of light gases, liquid hydrocarbons and waxes.

1.2.1 *History*

The first decades of the XX century have seen the transition from coal to oil as primary source of energy for the global energy market. Both the development in the transportation sector and the industrial growth has led to the need of cheap, easy transportable and high density source of energy.

In such environment, especially in countries rich in coal fields as Germany, the interest into production of liquid synthetic fuels started to grow. Amongst many routes proposed to achieve this goal, the most important ones are ascribed to three German scientists: Friedrich Bergius (Nobel Prize in Chemistry, 1931), Franz Fischer and Hans Tropsch. The first one found a way for the liquefaction of coal via hydrogenation at high pressures. A couple of years later Bergius himself, together with Fischer and Tropsch, found a way to use coal to produce a mixture of hydrocarbons (5). Production of liquid hydrocarbons over a cobalt catalyst was first reported in 1913 on a patent granted to *BASF*, related to a catalytic hydrogenation of CO at 300-400 °C and 120 atm with ceria-, cobalt-, molybdenum-based catalysts giving a mixture of hydrocarbons, alcohols, ketones and acids. During the following years, until *World War I* (WWI), many studies had been performed on reduction of CO in an iron based catalytic environment at high temperatures (400-450 °C) and pressures (100-150 atm). With the goal of increasing the alkane content, Fischer and Tropsch observed that oxygenated product fraction could have been lowered by performing the reaction at lower pressures, around 7 atm. In the attempt of solving the problem of decreasing catalytic activity at lower pressures, the two German scientists developed a new cobalt-iron catalyst; this first way of obtaining a mixture with high hydrocarbon content led to the origin of the Fischer-Tropsch Synthesis. In the subsequent decades, catalyst technology has advanced from a simple cobalt oxide supported on asbestos to sophisticated, high-activity, highly-optimized cobalt catalyst supported on carefully-modified alumina, silica or titania and promoted with noble metals and basic oxides. With outstanding improvements in the experimental layout, catalyst design has evolved from a trivial trial and error procedure to a scientific, nanoscale design founded on activity-structure relationship.

Advances in cobalt catalyst design can be conveniently subdivided in six historical periods (6):

1. Discovery (1902-1928). Cobalt catalysts were established as the most active and selective for FTS.
2. Commercial development of cobalt and iron catalysts (1929-1949). Mostly developed by the Nazis in Germany by *Ruhrchemie* and *IG Farben* (group including *BASF* at that time), where it contributed to gasoline and chemical production from coal during WWII and subsequently in USA. In 1928 the US company *Kellogg* made a first scale

up of the reactor, building a 13 m, high-circulating fluidized bed (CFB) reactor, soon shut down due to rising costs of natural gas. In these years, also 9 German plants were closed for the same reasons.

3. The “iron age” (1950-1974). Apartheid forced South Africa to take the lead in the field with its company *Sasol*, which in 1955 started performing FTS in the famous *Sasol I* plant. This employed three reactors in parallel, two CFB (with the same technology developed by *Kellogg*) and a FB (fixed bed). During the 1960’s, oil price decreased thus leading to a partial abandoning of GTL technologies.
4. Rediscovery of cobalt (1975-1990). In 1973 OPEC embargo and the following energetic crisis renewed the interest in synthetic fuels, with Sasol playing a leading role with the construction of *Sasol II* plant in 1974, consisting of a CFB reactor three times bigger than those in *Sasol I*. Few years later the production was doubled with *Sasol III* plant (1980).
5. GTL and return to cobalt (1991-2014). After a new phase of stagnation, interest in FTS was raised again starting from the 90’s with a renewed focus on conversion of natural gas to clean liquid fuels, both due to increasing oil prices and stricter environmental legislations. In 1993 *Shell*’s first plant in Bintulu started operating with a production of 12500 [bpd], followed in 2006 by *Sasol-Oryx* GTL plant, which produces 34000 [bpd].
6. Economic and oil crisis (2014-present day). From the second half of 2014, oil prices dropped 100\$ per barrel to less than 30\$ in a few weeks, thus strongly limiting the economic interest of FTS, which it is estimated to require to be competitive, with current technologies, values around 90\$ per barrel (7).

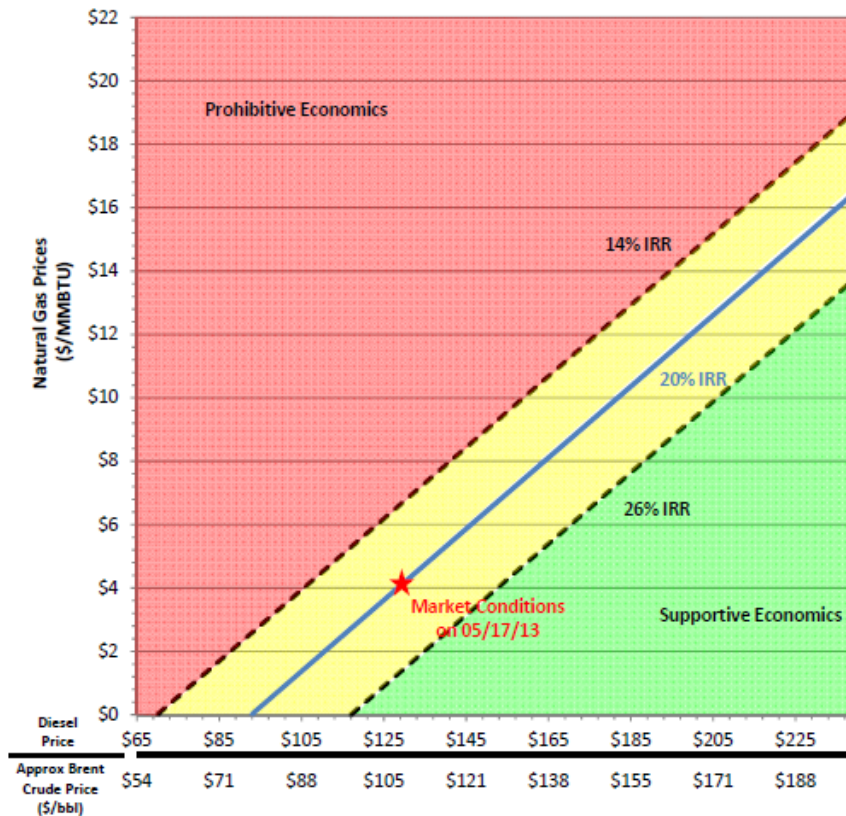


Figure 8. Viability envelope for GTL projects. (7)

1.2.2 Active Catalysts

It is well known that all Group VIII transition metals are active in FT synthesis. However, the only catalysts that have sufficient hydrogenation activity for commercial applications have Ni, Co, Fe or Ru as the active metal phase (8). A common feature of these materials is their strong interaction with CO and the ability to dissociate adsorbed carbon monoxide. It should be noticed that CO adsorption should be neither too strong nor too weak, since this would lead to methanation rather than chain growth (9). Coupling of partially hydrogenated surface intermediates leads to the formation of long-chain surface species, which upon desorption form a mixture of organic product compounds. The exact choice of the metal to be used in a particular catalyst formulation depends on a number of parameters including the source of carbon used for making syngas (i.e. the syngas H₂/CO ratio), price and end product desired. Industrially, only Co-based and Fe-based catalysts are employed due to their optimal compromise between activity and costs. Ni has too high hydrogenation activity resulting in high yields of methane while Ru usage in industrial FT applications is questionable due to its prohibitive cost. Cobalt is three times more active than iron:

however, its price is almost 250 times higher. It has to be considered that FTS is always accompanied with the secondary *Water Gas Shift (WGS)* reaction, the relevance of which cannot be neglected for the catalyst choice. Catalysts for the conversion of syngas obtained from a carbon-rich source, such as coal, are usually Fe-based due to the high WGS activity of iron, which tends to re-equilibrate the H₂/CO ratio to the stoichiometric value needed for FTS. Co-based catalysts are preferred for the production of heavy paraffins, due to their high selectivity towards hydrocarbons with high molecular weight. They require a relatively clean feedstock and produce much less oxygenates than Fe catalysts, due higher hydrogenation activity of Co compared to that of Fe. On the other hand, if linear olefins are wanted as end-product, Fe-based catalysts are the best choice because hydrogenation of the primary formed olefins is less favoured. However, Fe based catalysts have the disadvantage of producing aromatics and oxygenates as by-products. Another difference between Co and Fe is related to their sensitivity towards impurities in the gas feed, such as H₂S: Fe-catalysts are by far more resistant than cobalt catalysts. On the other hand, Co-based catalysts are known to be more resistant towards oxidation and more stable against deactivation by water.

Table 1. Overview of some features of Ni, Fe, Co and Ru-based FT catalyst.

<u>Active Metal Price FT activity WGS activity Hydrogenation activity</u>				
	Price	FT Activity	WGS Activity	Hydrogenation Activity
Ni	++++	+	+/-	+++++
Fe	+	+	+++	+
Co	+++	+++	+/-	+++
Re	+++++	+++++	+/-	+++

It is remarkable that, despite the large body of papers and patents published in the last decades about possible improvements of Co-based catalysts, the modern FT catalysts are still very similar to the early ones prepared by Fischer and co-workers, consisting of

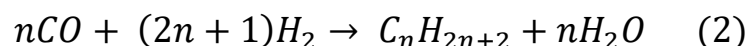
promoted cobalt particles supported on a metal oxide. Most of Co-based catalysts consist of the following components:

- Metallic cobalt (Co^0) as the active phase;
- High surface area support: typically, alumina (Al_2O_3), titania (TiO_2) and silica (SiO_2). Its function is to provide mechanical strength and thermal stability while contributing to a high Co dispersion;
- Promoter metals (typically noble metals such as Ru, Re, Pd Pt, Rh): their roles may vary much, depending on the metal employed. For instance, platinum and ruthenium facilitate reduction of cobalt clusters thus increasing the number of cobalt active sites during reaction.

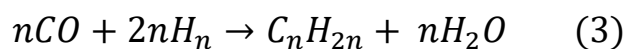
1.2.3 Chemistry

Although the chemistry of the Fischer-Tropsch synthesis is quite complex, the fundamental features can be represented with the overall stoichiometry:

Alkanes formation:



Alkenes formation:

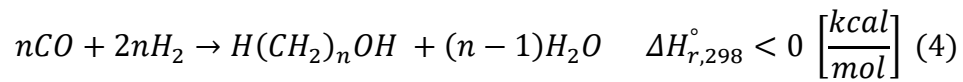


The production of a specific hydrocarbon, other than methane, has not yet been achieved: what is formed is always a mixture of hydrocarbons with different chain lengths and so different molecular weights. Characteristic of the Fischer-Tropsch reactions is their high exothermicity: the formation of one mole of $-\text{CH}_2-$ is accompanied by a significant heat release of about 40 kcal.

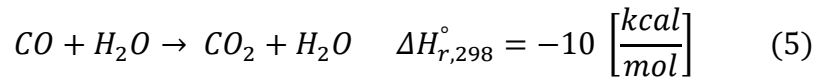
1.2.3.1 Main Side Reactions

Along with the main reactions, some side reactions also occur:

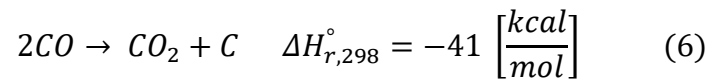
Alcohols formation:



Water gas shift (WGS) reaction:



Boudouard reaction:



Methanation reaction:



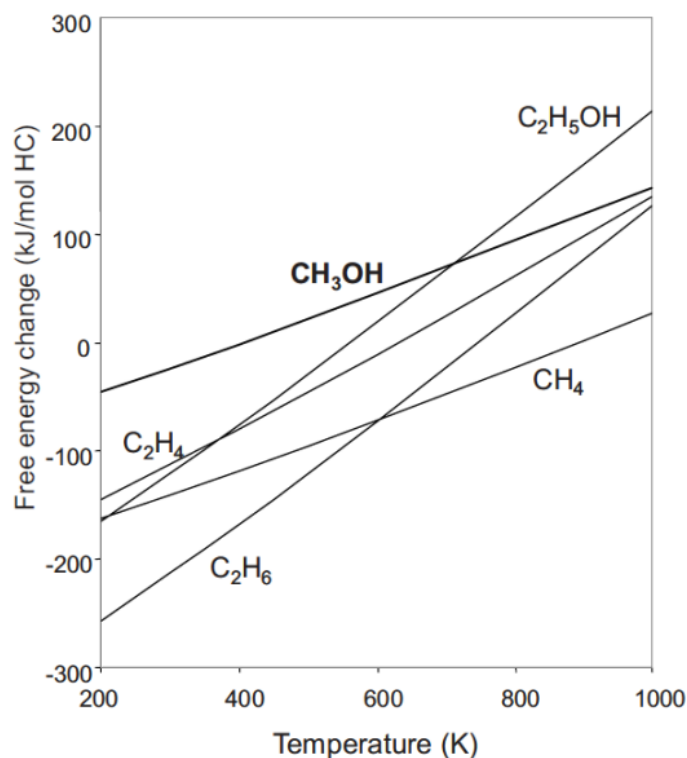


Figure 9. Products from CO and H₂, standard free energy of formation. (10)

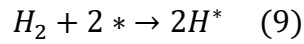
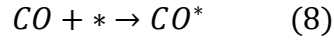
From the Francis diagram, reported in Figure 9, it is clear that thermodynamically both hydrocarbons and alcohols can be formed starting from syngas: for this reason, the choice of proper catalyst and operating conditions is very important. The WGS reaction is responsible both for the production on CO₂ and the adjustment of the H₂/CO ratio. For example, in the Fe-catalyzed Fischer-Tropsch synthesis, the reverse-WGS, favoured by the metal function, helps to bring the reactant ratio of a usually H₂-poor syngas (produced from biomass or coal) towards the stoichiometric value. The *Boudouard* reaction is undesired as it produces CO₂ and coke; the latter covers the catalyst surface, leading to deactivation. Problems linked to the methanation reaction are the high exothermicity and the production of CH₄, a hydrocarbon of little value in the product distribution.

1.2.3.2 Mechanism

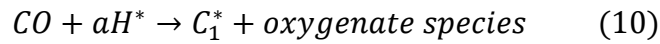
What really occurs on the surface of the catalyst during Fischer-Tropsch synthesis is still much debated among scientists. Many theories have been formulated to describe the evolution of the system during the reaction: although differences occur between them, the common element is the concept of a stepwise addition of monomeric C₁ units to a growing

chain. The parallelism of a polyaddition mechanism is not far from the concept at issue, as in fact the product distribution is modelled from this similarity. The usual steps involved in the mechanism are the following (* is referred to as the catalyst active site):

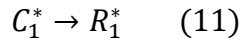
Reactant adsorption:



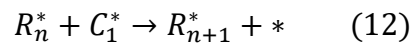
In situ monomer formation:



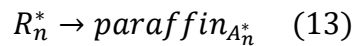
Chain initiation:



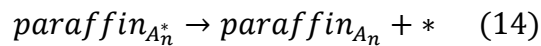
Chain propagation:

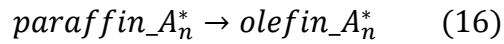
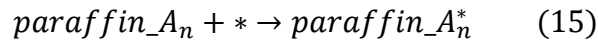


Chain termination:

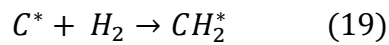
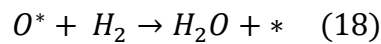
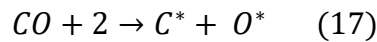


Product desorption:



Product re-adsorption and secondary reactions:

The earliest hypothesis for the FTS mechanism was proposed by Fischer and Tropsch themselves in 1926 and is known as the “carbide theory”. The first step is suggested to be the CO dissociative adsorption leaving an oxide and a carbide site, which would then both react with H₂ forming water and an adsorbed methylene species, respectively:



The methylene species, assumed as the C₁* monomer, is then inserted into a C_n growing chain, leaving an adsorbed C_{n+1} hydrocarbon species and a free active site:

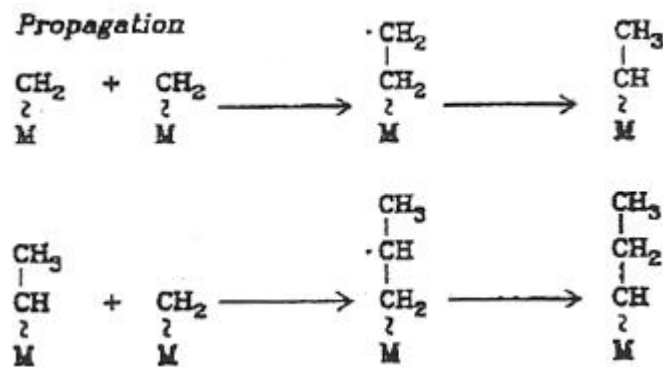


Figura 10. Propagation in the Carbide theory. (11)

Finally, the alkyl desorption proceeds via either dissociative β -H-abstraction or associative α -H addition, leaving an α -olefin or a paraffin respectively:

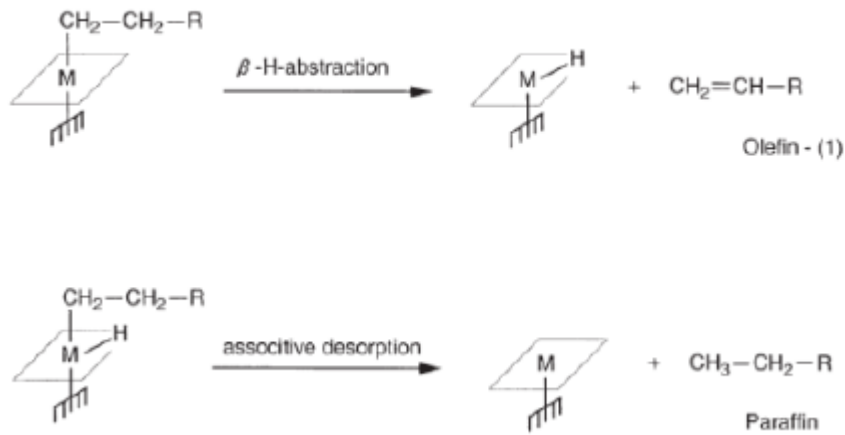


Figure 11. Termination in the carbide theory. (12)

The main limitation of this theory is the impossibility of predicting the formation of oxygenate species, which are always present in the product mixture in rather small amounts. Nevertheless, experimental studies ((13) - (14)) which involved application of sophisticated surface analysis techniques are in accordance with the carbide theory. In fact, the general agreement is that carbenes (CH_2^*) are actually involved in the chain growth mechanism with CO insertion accounting for the formation of oxygenate compounds (15). In the 1950s a new mechanism proposed by *Eiidus* (15), acknowledged as the “enol theory”, gained widespread acceptance. It involves the chemisorption of CO which is then partially hydrogenated generating the C_1^* monomer unit (enol) active in the chain growth mechanism.

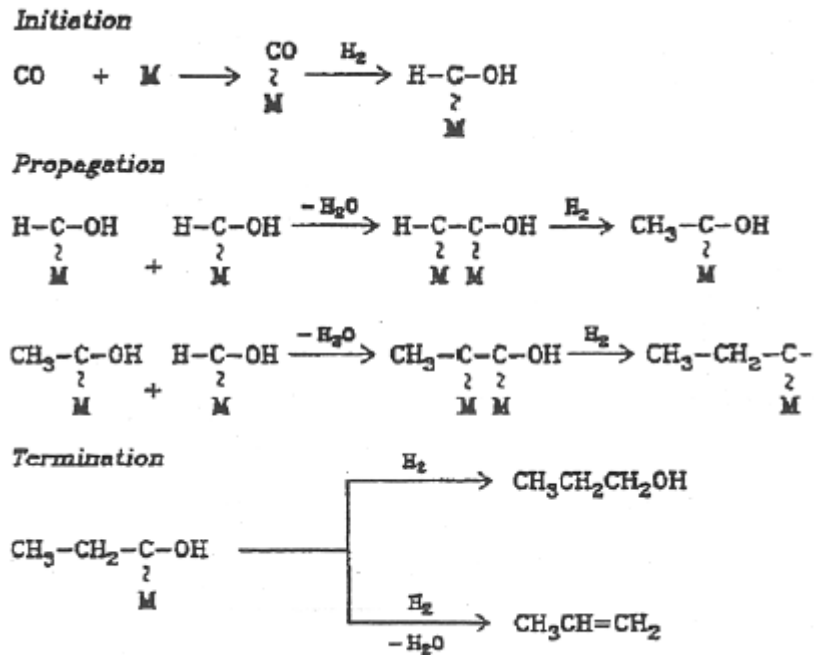
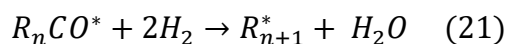
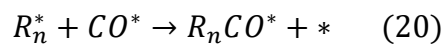


Figure 12. Scheme of the enol mechanism. (11)

The propagation occurs via subsequent condensation of monomer units with the growing chain. Main benefit of this mechanism is the possibility of forecasting all the species produced during FTS: in fact, alcohols are generated by hydrogenation of the hydroxyl-carbene units, aldehydes by direct desorption and hydrocarbons by a double step of hydrogenation and condensation. Another important theory is known as the “direct insertion theory”, proposed by *Pichler et al.* (16) and later taken up by *Wender et al.* (17). It proposes the insertion of the adsorbed CO molecule between the catalyst active site and the C atom of the adsorbed alkyl species, as per the reaction. The acyl group $R_n\text{CO}^*$ is later hydrogenated forming an adsorbed alkyl chain with an additional methylene unit:



The advantage of this theory is the same as the enolic, because it is capable of foreseeing formation of both hydrocarbon and oxygenate species. Some alternative theories aim to couple the early hypothesis proposed by Fischer and Tropsch with the experimentally

observed formation of oxygenate compounds. For example, *Dry* (15) proposed an additional chain growth mechanism, parallel to the carbide mechanism, leading to the formation of alcohols, aldehydes and carboxylic acids:

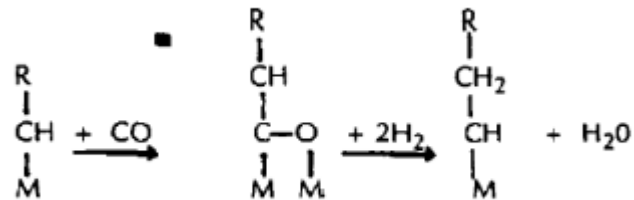


Figure 13. Chain growth proposed by Dry. (15)

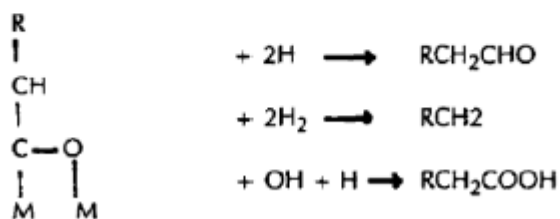
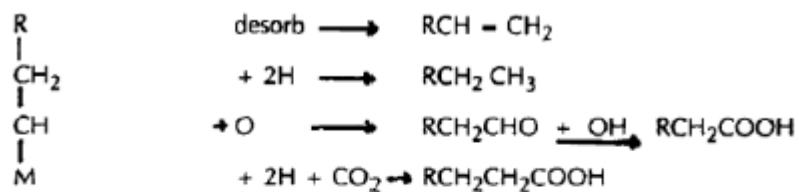
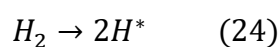
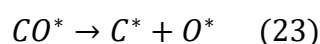
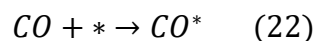


Figure 14. Termination proposed by Dry. (15)

Although it may seem difficult that all of the above termination reactions do actually occur, the author defends his hypothesis ascribing it to the heterogeneity of the working surface of a FT catalyst, over which many different intermediates are likely to present.

An alternative mechanism that accounts for the oxygenates formation is the one proposed by *Schulz and Van Steen* (18). Differently from *Dry* (15), a second series of reactions that lead to the solely formation of hydrocarbons is assumed to occur: in this way the larger presence of hydrocarbons against that of oxygenates is explained.



The incapacity of the theory of predicting the formation of alcohols, aldehydes and carboxylic acids is ascribed to the exclusive O* desorption in the form of CO₂ and water. In addition, more recent studies seem in contrast with this mechanism as they suggest, instead of a simple molecular adsorption, an hydrogen assisted CO dissociation to form the active monomer (19).

The difficulty of some of the theories in describing the whole product range and the different

catalytic behaviour of the metals industrially employed has led some scientists to speculate on the presence multiple key intermediates in FT synthesis (20). In particular, it has been proposed that the direct CO insertion mechanism is responsible of the oxygenates formation, while the hydrocarbons are formed as stated by the carbide theory. More recent studies (21) have led to the definition of an innovative kinetic mechanism in which the adsorbed CO can follow two reaction pathways, depending on the hydrogen role in its activation.

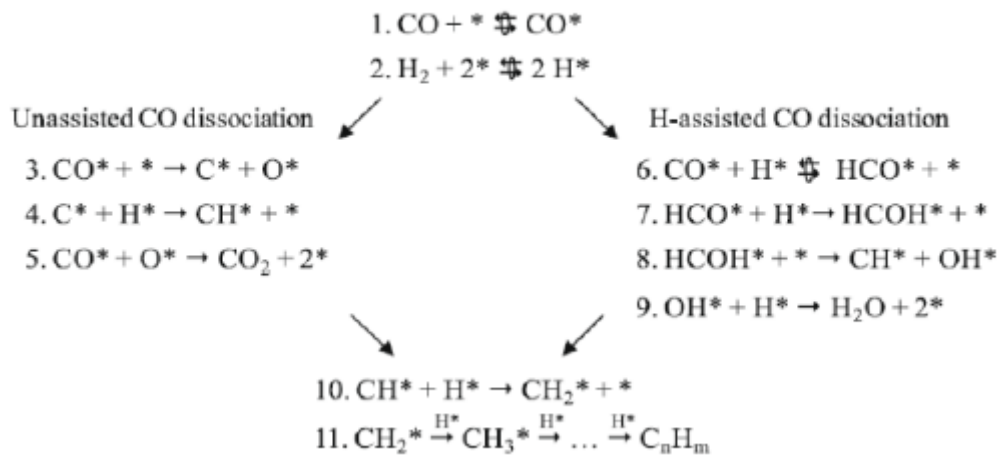


Figure 15. Chain growth mechanism according to Iglesia et al. (21)

The unassisted dissociation leads to the formation of two intermediates, C^* and O^* , from an adsorbed CO molecule. C^* further reacts with hydrogen forming the active monomer, whereas O^* reacts with another CO^* molecule forming carbon dioxide. In the parallel mechanism, referred to as the “H-assisted CO dissociation”, a formyl (HCO^*) intermediate is formed: it is then hydrogenated forming an hydroxymethylene (HCOH^*) species which subsequently dissociates forming CH^* and OH^* . The latter are then hydrogenated forming, respectively, the active monomer and water.

In addition, Iglesia et al. (21) could prove, through theoretical and kinetic studies, that the CO dissociation mechanisms are different depending on the catalyst employed. Iron is known to be more selective towards CO_2 : the reason of this behaviour is ascribed to a lower activation energy for the unassisted CO dissociation pathway. On the other hand, the H-assisted CO dissociation is predominant when using cobalt catalysts: this is perfectly in line with the much lower CO_2 productivity compared to that obtained using iron.

1.2.4 Product distribution

Various mechanisms have been proposed to describe the product distribution of the FT synthesis. However, no matter what the exact mechanism is, the growth of a hydrocarbon

chain is assumed to occur by a stepwise addition of a C₁ unit derived from CO to the end of the growing chain. The widely recognised statistical model is the one formulated by Flory (22) and then further developed by Anderson and Schulz (23), known as the ASF distribution. The theory is based on the parallelism between the chain growth mechanism of the FT synthesis and that of a poly-addition reaction. In addition, some simplifications are also taken into account:

- Absence of branched products
- No difference between the growth of olefins and paraffins
- Absence of secondary reactions
- Relative probability of chain growth and termination independent of the carbon number

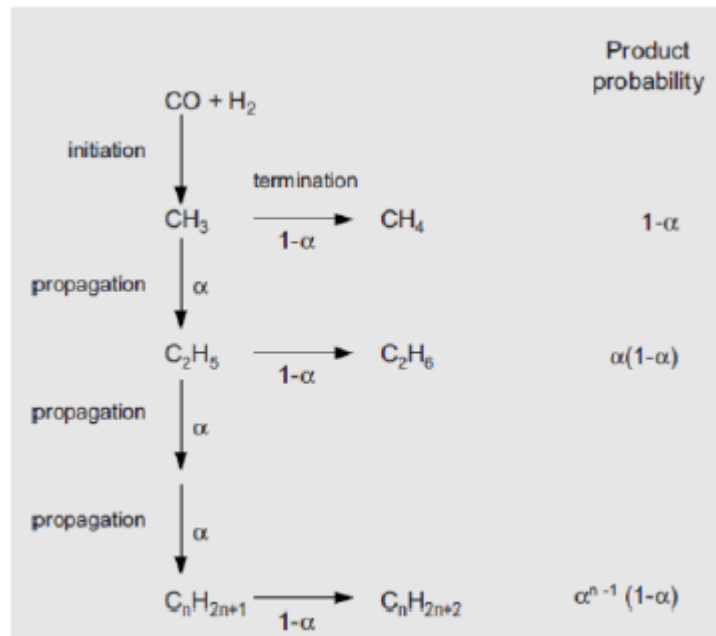


Figure 16. Chain growth mechanism for FT synthesis: ASF (10)

The relative probability of chain growth is identified in the ASF model with the greek letter α . It is defined by:

$$\alpha = \frac{R_P}{R_P + R_T} \quad (28)$$

Where R_P and R_T correspond to the propagation and termination rate, respectively. α is a

dimensionless parameter, independent of the carbon number, which assumes values in the range 0÷1. Typical values (24) for Co and Fe catalysts are around 0.5÷0.85.

As shown in the Figure 16, a single chain growth step has a probability α , whereas the termination reaction has a probability $(1 - \alpha)$. The null value of α corresponds to a 100% termination probability, whereas the unity value corresponds to a 100% propagation probability. Therefore, the probability of obtaining a hydrocarbon with N carbon atoms in its chain (P_N) is given by the achievement of $(N-1)$ polymerization steps followed by a termination step. As each step is regarded as a statistically independent event, the probability of obtaining P_N is given by the probability product of the events associated to the formation of P_N :

$$P_N = \alpha^{(N-1)} * (1 - \alpha) \quad (29)$$

The probability P_N can be referred to as a molar fraction of the CN species. It is possible to switch to mass fractions by means of a constant denoted with A :

$$\omega_n = A * P_N * n \quad (30)$$

The constant A can be found by imposing the stoichiometric balance in the reaction:

$$\int_0^{\infty} \omega_n dn = 1 \quad (31)$$

$$\int_0^{\infty} (A * P_N * n) dn = 1 \quad (32)$$

By substituting the expression of P_N and solving the integral, the expression assumed by A is the following:

$$A = \frac{\alpha \log^2 \alpha}{1 - \alpha} \quad (33)$$

Substituting the value of A into the mass fraction expression (Eq. 30) and rearranging the terms the final equation of the ASF model is obtained:

$$\log\left(\frac{\omega_n}{n}\right) = \log(\log^2 \alpha) + n \log \alpha \quad (34)$$

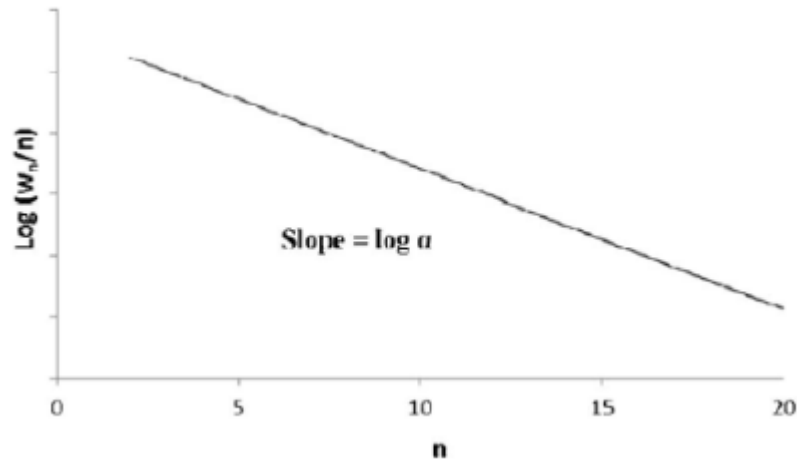


Figure 17. Classical ASF product distribution. (24)

Being α a value between 0 and 1, and thus negative the slope, a decreasing profile is obtained. The closer is α to one, the richer will be the product mixture of heavy hydrocarbons. With the ASF equation, all the complexity of the FTS kinetics governing the product distribution is conveniently lumped into the single parameter α .

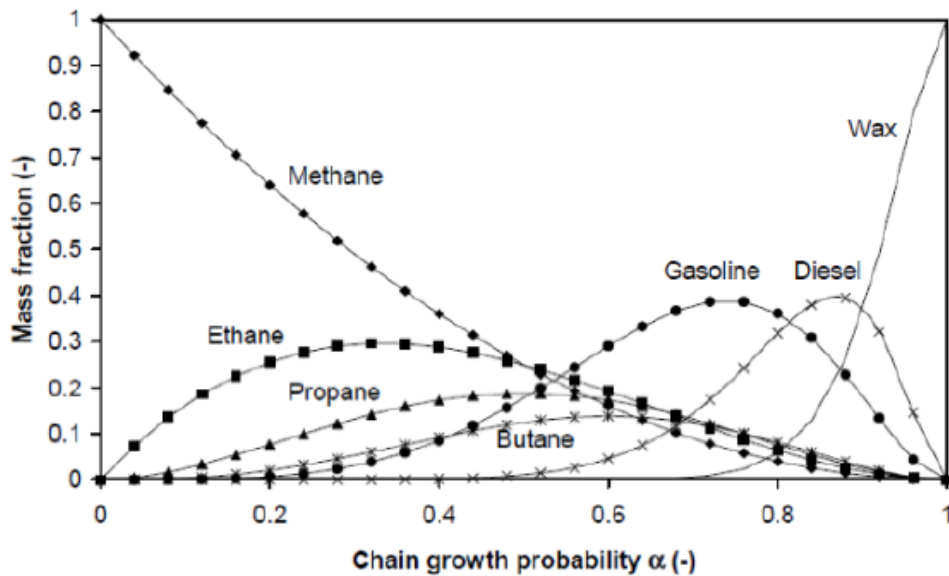


Figure 18. Product mass fraction profiles as a function of α (25)

Industrially, as diesel and waxes are the desired products, the catalyst and process conditions are tailored to obtain α values around $0.8 \div 0.9$. More recently the aim has shifted towards maximum yield just in waxes ($\alpha \approx 0.95$), which can be obtained with higher selectivity than diesel and can then be further converted into valuable products (10). At the expenses of its high simplicity, the ASF model unfortunately presents some discrepancies when compared to the experimental data obtained in FT conditions.

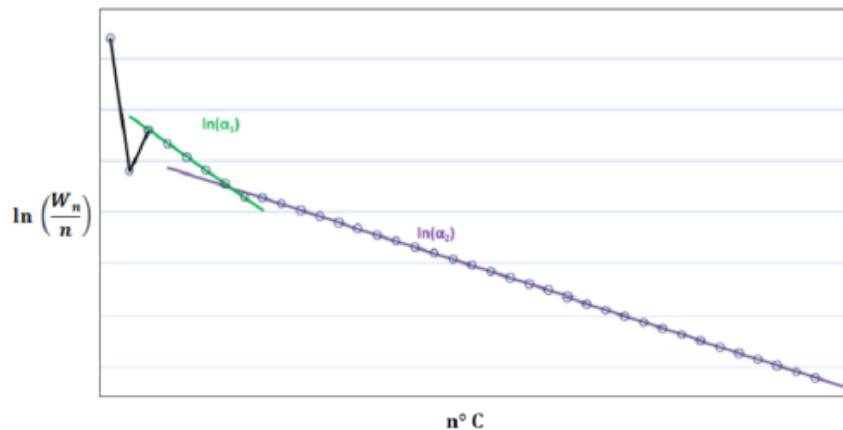


Figure 19. Typical experimental distribution of FT products. (26)

In particular:

- The methane yield is underestimated
- The ethylene yield is overestimated
- The value of α increases when increasing the carbon number

An addition, neglecting the assumptions made concerning olefins and paraffins, one would observe a decreasing trend in their ratio when increasing the carbon number. The following paragraphs focus on the main reasons for which the ASF theory lacks in correctly describing the whole hydrocarbon yield.

- *Deviation of C_1*

It is clear from Figure 20 that the ASF model underestimates the experimental methane production. This behaviour can be at first ascribed to the possible activity of FT catalysts towards hydrogenolysis reactions of paraffins and olefins. In addition, also diffusive limitations can play an important role: as H_2 molecular diffusivity is way higher than that

of CO, deep in the catalyst pores the H₂/CO ratio may lie above the optimal one, thus favouring the methanation reaction. Other theories attribute the excessive methane production to the formation of local hot-spots on the catalyst.

- *Deviation of C₂*

The experimental data on the C₂ selectivity are instead overvalued by the ASF model. This overestimation is ascribed to re-adsorption mechanisms of ethylene which is then reintroduced into the polymerization pathway. Alternatively, the deviation can be attributed to the high reactivity and surface mobility of the C₂ precursors.

- *Variation of chain growth probability and olefin to paraffin ratio*

The main lumped kinetic approaches dealing with deviations from the ASF distribution can be divided into two schools of thought: the first asserts the presence of a bimodal distribution of α in the ASF (double- α chain growth models), the second ascribes the discrepancy of the olefin to paraffin ratio to n-olefin readsorption mechanisms which would favour paraffin formation (olefin readsorption models).

- *Double- α models*

Since experimentally an increase of the chain growth probability was often observed at carbon numbers around 10, some authors decided to describe the total hydrocarbon yield by means of two ASF distributions. In particular, *Madon and Taylor* (27) credited the double- α behaviour to the presence of structurally different active sites on the catalyst surface: one over which the C₁-C₁₀ production dominates (α_1), another where heavier products are more likely formed (α_2). The same hypothesis was made by *Wojciechowski* (28): each active site has its own chain growth probability and, depending on the termination reaction by adding either hydrogen or a methyl group, different product distributions are obtained.

Other authors (29) associated the double- α behaviour to different chain growth mechanisms.

Nevertheless, it is worth noticing that, even though these theories can explain the change of α in the ASF distribution, they are unable to predict the related drop in the olefin to paraffin ratio.

- *Olefin-readsorption models*

A more likely explanation of the deviation from the ASF distribution involves secondary reactions (reinsertion, hydrogenation, hydrogenolysis and isomerization) of olefins. The olefin-readsorption models could in this way fill the lack of the double- α models, predicting both the increase of the chain growth probability and the decrease of the olefin to paraffin ratio. The qualitative profile of the latter can be expressed with the empiric law formulated by *Kuipers et al.* (30):

$$\frac{O_N}{P_N} \propto e^{-C \cdot N} \quad (35)$$

Where C is a constant while O_N and P_N are the molar fractions of an olefin and a paraffin, respectively, with N carbon atoms in its chain. This theory is strengthened by experimental evidence of olefin readsorption on the active sites, which results in a heavier and more paraffinic product mixture. These secondary reactions that cause the deviations in the ASF distribution are generally accepted to be chain-length dependent. Three different phenomena influenced by the chain length have been proposed by *Kuipers et al.* (30):

- The diffusion of olefins within the catalyst pores filled with liquid product
- The solubility of olefins into the liquid product
- The physisorption of olefins in the proximity of the catalyst surface

It is evident from these phenomena the importance of the interfacial effects of the reactive olefins with the gas-liquid and the liquid-catalyst surface interfaces.

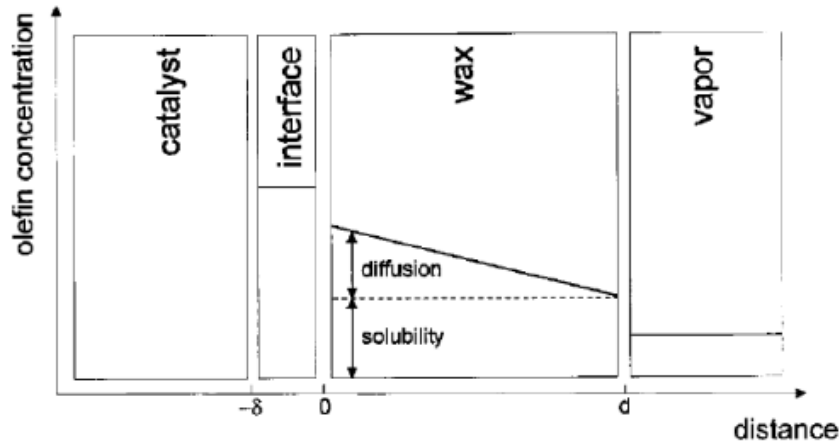


Figure 20. Olefins concentration profile across the phases. (30)

Figure 20 is a schematic representation of the olefin concentration profile in the reaction environment. Within the film of liquid product ($0 < x < d$) over the catalyst an olefin concentration gradient is established: it is dependent of the olefin formation rate, the layer thickness and the liquid phase diffusivity (\mathfrak{D}_N). The latter is in turn function of the chain length via the following relation, proposed by Van der Laan et al. (24):

$$\mathfrak{D}_N \propto N^{-0.5} \quad (36)$$

A similar relation is proposed by *Iglesia et al.* (31), who use an exponential function with a different coefficient:

$$\mathfrak{D}_N \propto \mathfrak{D}_0 \cdot e^{-0.6 N} \quad (37)$$

Where \mathfrak{D}_0 is the reference diffusion coefficient ($[m^2/s]$). The physisorption of olefins is in turn referred to as a chain length independent phenomenon which occurs on the catalyst surface ($x = \delta$). *Iglesia* stated that the real reason of the decrease in the ON/PN ratio is to be imputed to diffusion limitations. As shown by Eq. 37, increasing N , the mobility of olefins in the liquid phase exponentially decreases: as a consequence, the contact time with the catalyst surface increases, resulting in a higher re-adsorption probability. However, the relation obtained by *Iglesia et al.* (31), even with its strong chain length dependency for the

diffusion coefficients, cannot predict the strong decrease in the olefin to paraffin ratio found experimentally. Moreover, other studies (32) have shown more reasonable chain length dependencies of the diffusion coefficients and using these diffusivities the model by *Iglesia et al.* (31) appears to underestimate the O_N/P_N ratio.

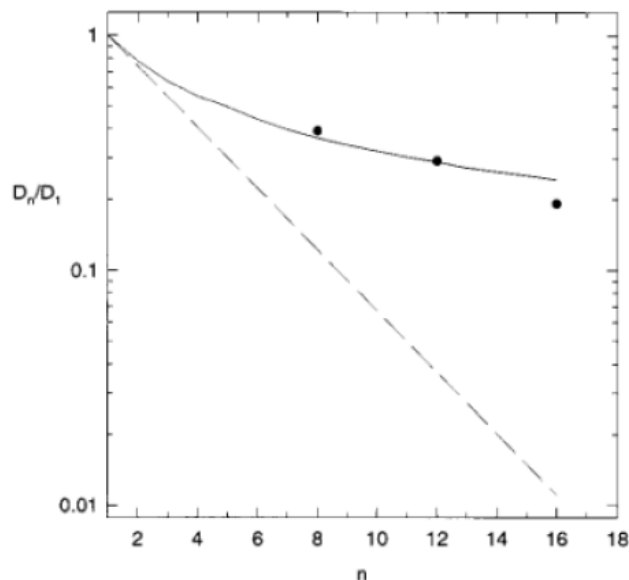


Figure 21. Diffusivities of *n*-paraffins in solid wax at 540 K. (24)

Furthermore, *Kuipers et al.* (30) measured the O_N/P_N ratio for the FTS on a polycrystalline cobalt foil, which structurally cannot generate diffusion limitations, and still found a strong exponential decrease with the chain length. Apparently, not only diffusion limitations have to be taken into account for the description of the product distribution, but also solubility and physisorption become relevant. *Van der Laan* (24) proposed the so-called “Olefin VLE model”, in which the chain length dependence of the olefin re-adsorption rate is credited to their increasing solubility in the FT waxy products. Generally, the most common species in the hydrocarbon phase are olefins with carbon numbers around $23 \div 30$: as a consequence, the solubilisation of heavier olefins is the most favoured, due to the high affinity of the latter with the hydrocarbon solvent. Likewise, also physisorption phenomena appear to affect the olefin to paraffin ratio. *Keldsen et al.* (24) measured the adsorption enthalpies of paraffins and found that the energetic levels for the adsorbent-adsorbate interactions vary with N according to the following equation:

$$-\Delta H_{ADS} = 12.6 + 8.7 \cdot N \quad (38)$$

Therefore, a high concentration of heavy products is found across the catalyst-liquid interface.

1.2.5 Influence of process conditions on the selectivity

It is widely accepted that the chain growth probability varies with the process conditions.

A

recapping table showing the main effects is reported by *Van der Laan and Beenackers* (24):

Table 2: Selectivity control in FTS by process conditions. (24)

Parameter	Chain length	Chain branching	Olefin selectivity	Alcohol selectivity	Carbon deposition	Methane selectivity
Temperature	↓	↑	*	↓	↑	↑
Pressure	↑	↓	*	↑	*	↓
H ₂ /CO	↓	↑	↓	↓	↓	↑
Conversion	*	*	↓	↓	↑	↑
Space velocity	*	*	↑	↑	*	↓
Alkali content iron catalyst	↑	↓	↑	↑	↑	↓

Note: Increase with increasing parameter: ↑. Decrease with increasing parameter: ↓. Complex relation: *.

- *Temperature*

Although an increase in temperature would favour the FT kinetics, the main drawback is a decrease in the chain growth probability, due to the increasing desorption rates favoured by the high temperature. The model derived by *Song et al.* (33) as a linear interpolation of experimental data, which were obtained by *Van der Laan and Beenackers* (24), emphasises the temperature dependence of the α parameter:

$$\alpha = \left(A \frac{y_{CO}}{y_{CO} + y_{H_2}} + B \right) [1 - 0.0039 (T - 533)] \quad (39)$$

Being $A = 0.2332 \pm 0.0740$, $B = 0.6330 \pm 0.0420$, T the temperature [K], y_{CO} and y_{H_2} the molar fraction of the feed gas. Figure 22 represents how the product distribution varies with

temperature, at a fixed syngas composition ($H_2/CO = 2$), as predicted by *Song et al.* (33):

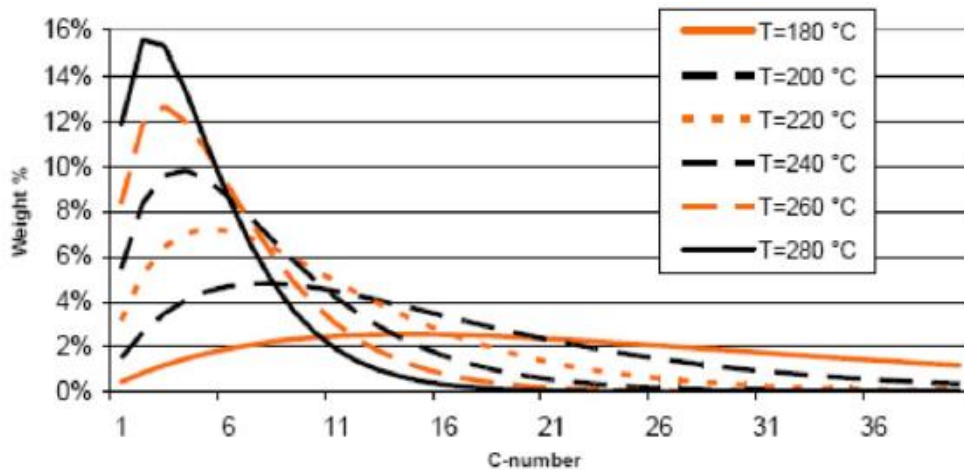


Figure 22. Product distribution as a function of temperature.

- *Partial pressure of CO and H₂*

It is widely recognized that the chain growth probability increases when increasing pressure: this behaviour can be credited to the limited desorption rate at higher pressures. In this manner, the product remains longer on the catalyst surface and grows its chain. Thus, in principle, the higher the pressure, the higher would be α . In the industrial process, though, the pressure choice is made in view of other major drawbacks of high operating pressures, which are significant pumping costs, high pressure drops and necessity of resistant materials. Industrial FT processes are commonly operated at $20 \div 25$ bar. In terms of partial pressures, H_2 is known to favour hydrogenation reactions, i.e. termination reactions, so high H_2/CO ratios tend to lower the chain growth probability. Figure 23 shows the product distribution as a function of the partial pressures of CO and H_2 :

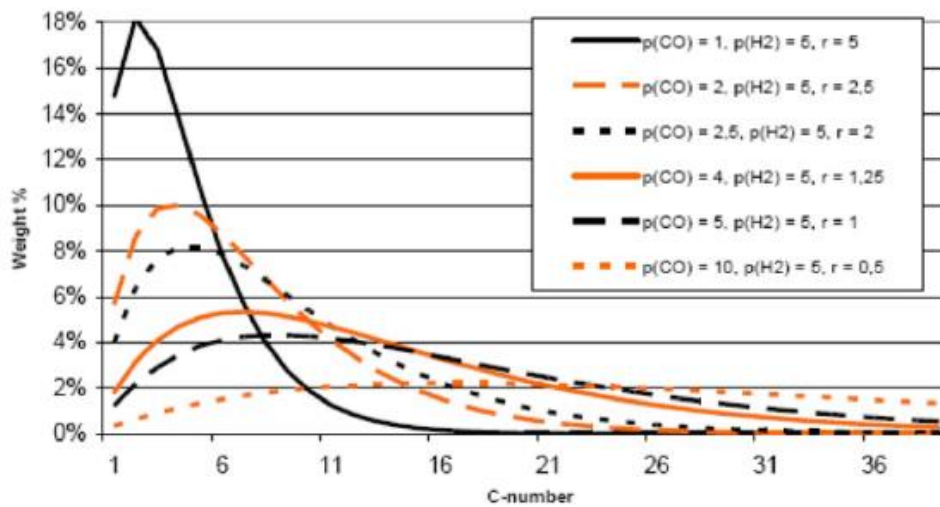


Figure 23. Product distribution as a function of the H₂/CO inlet ratio r .

- *Space velocity*

The effect of space velocity has been studied by various authors. *Kuipers et al.* (34) found an increase of the O_N/P_N ratio when decreasing the contact time (i.e. increasing the space velocity) and *Iglesia et al.* (31) measured an increase in the average product molecular weight when increasing the contact time. Thus, apparently, low space velocities favour the yield in the desired product: again, industrially the main drawback of operations with low gas flows is the inefficient heat removal, due to the low heat transfer coefficients. In such a highly exothermic process as FTS temperature control is a major concern, thus gas velocities need to be kept high: so, in order to ensure both the contact time needed for a good selectivity and high heat transfer coefficient, high flows and long tubes are industrially employed.

1.2.6 LTFT and HTFT operations

Usually FT processes can be classified, according to the operating temperatures, into *Low Temperature FT (LTFT)* and *High Temperature FT (HTFT)*. LTFT processes are usually operated at $T = 200 \div 240$ °C and aim at the production of heavy hydrocarbons, which are then upgraded to a high quality diesel. The reaction environment of a LTFT process is three-phasic: it comprises a gaseous phase, consisting of syngas and light products, a liquid phase, rich of waxy products, and a solid phase, which is the catalyst. HTFT processes

operate at significantly higher temperatures ($T = 300 \div 350 \text{ }^\circ\text{C}$) and aim to produce light hydrocarbon products in the range $\text{C}_2 \div \text{C}_{11}$, which are then upgraded to gasoline. Such high temperatures are needed to guarantee gas-solid operations. Figure 24 shows typical product distributions for both the process choices, compared to the composition of a light crude oil:

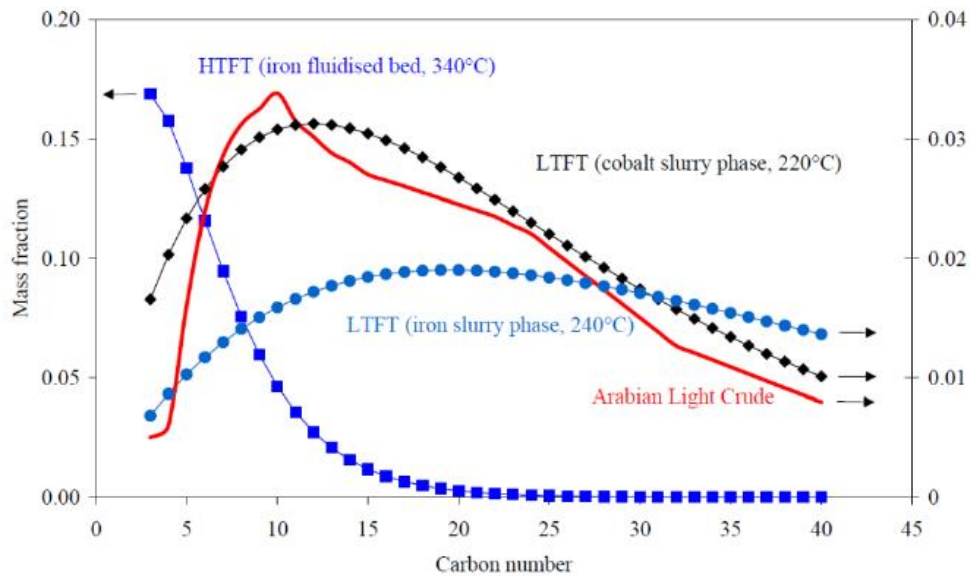


Figure 24. FT product distribution: HTFT vs LTFT. (35)

The closest composition to that of the Arabian Light Crude appears to be the syncrude obtain at low temperatures using Co-based catalyst. Along with the product distribution, also the catalyst choice is strictly related to the operating conditions. More in particular:

- Co is employed at low temperature (Co-based LTFT)
- Fe is used both at high and low temperatures (Fe-based LTFT & Fe-based HTFT)

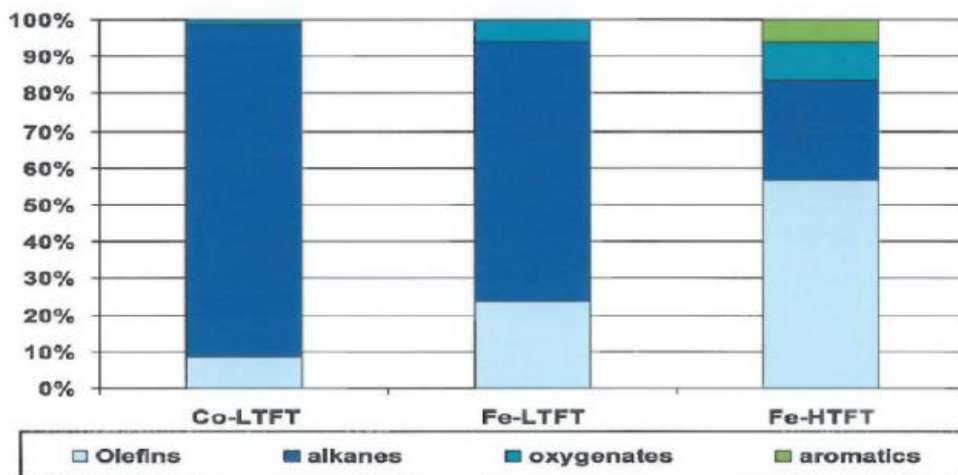


Figure 25. Product yield with different processes. (36)

1.2.7 FT reactors

When designing reactors for Fischer-Tropsch synthesis, the major concern is always temperature control. Being the reaction strongly exothermic, the objective is to minimise the temperature rise along the bed: to achieve this requires a rapid heat removal in the direction perpendicular to the reactant flow. Being FT synthesis kinetically controlled, the objective of keeping the temperature down is not related to equilibrium considerations such as in other industrial processes, like methanol or ammonia production. The reasons for the strict temperature control are instead mainly related to the catalyst activity and product selectivity. As in most exothermic processes, the heat removal is performed via heat exchangers, fed with water, which produce useful steam for the process. The higher the temperatures at of the heat exchange, the higher the pressure of the steam produced and the higher the overall thermal efficiency of the process. To achieve rapid heat transfer from the reaction zone to the heat exchanger wall, different configurations are industrially employed:

- *Multi-tubular fixed bed reactor (MTFBR)*
- *Circulating fluidized bed reactor (CFBR)*
- *Slurry bubble column reactor (SBCR)*

1.2.7.1 Multi-tubular fixed bed reactor (MTFBR)

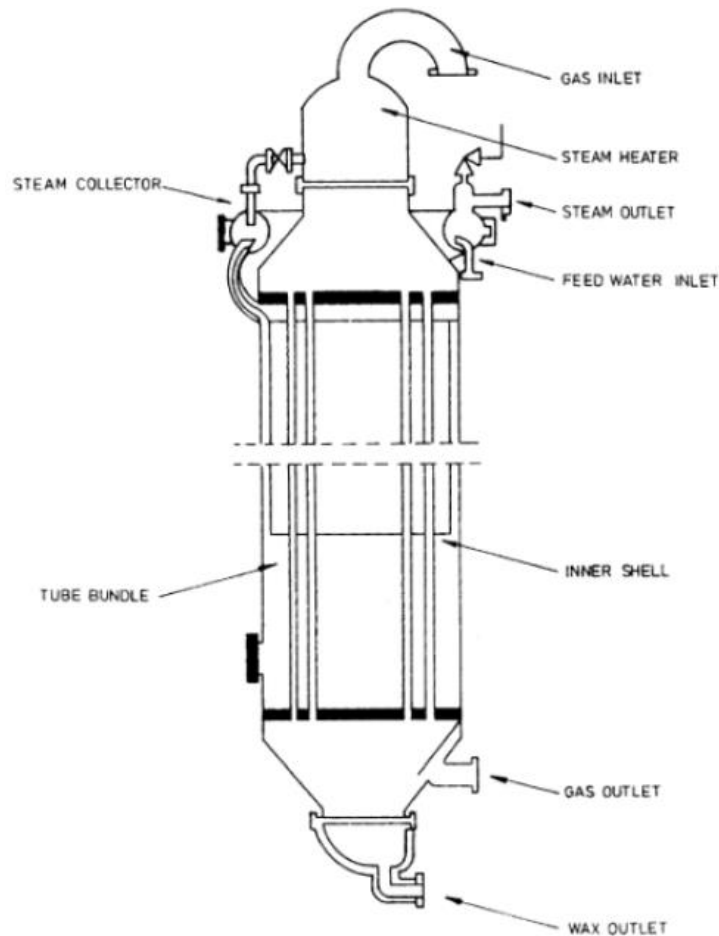


Figure 26. Multitubular fixed bed reactor. (27)

The multi-tubular reactor design comprises thousands of long (12 ÷ 20 m) and narrow (2 in) tubes, filled with catalyst particles, inserted into a vessel in which flows cooling water shell-side. The syngas mixture flows tube-side and reacts along the catalyst bed, producing heat. Typical operating conditions of these units are reported below:

Table 3: Multitubular Fixed Bed Reactor: operating conditions:

Temperature [°C]	200 ÷ 220
Pressure [bar]	25
Active Phase of Catalyst	Iron / Cobalt

The advantage of using narrow tubes is the reduction of the distance between the centre of the tube, where usually the hot spots occur, and the tube wall, surrounded by the coolant. In addition, for the same bed volume, a higher number of tubes results in a higher heat transfer area, ensuring a better heat removal.

Also, high gas velocity produces a turbulent flow, which increases heat transfer coefficients and minimizes the thickness of the stagnant layer, over the catalyst surface and the tube wall, of reactants and products: this layer has to be minimized as it limits the heat transfer.

The advantages of a MTFBR design are as follows. They are easy to operate. There is no problem of catalyst-product separation. The liquid product trickles down the reactor and is collected at the bottom, where it is easily separated from the gas phase via a knock-out vessel: for this reason, the MTFBR design is suitable for wax production. On the other hand, many are the economical disadvantages. The construction cost is substantial. The high flow rate, needed for an efficient heat transfer, results in large pressure drops along the bed, which, coupled with the gas recycle, make the compression costs rise significantly. As FT is diffusion limited, the use of small particles would increase the catalyst efficiency and thus the production: however, this would result in an even higher differential pressure over the reactor.

Another major drawback is linked to the catalyst replacement: the latter is, due to the narrow tubes employed, a challenging operation that cannot be performed on-line. Obviously, the longer the downtimes, the greater the economic loss for the plant.

1.2.7.2 *Circulating fluidized bed reactor (CFBR)*

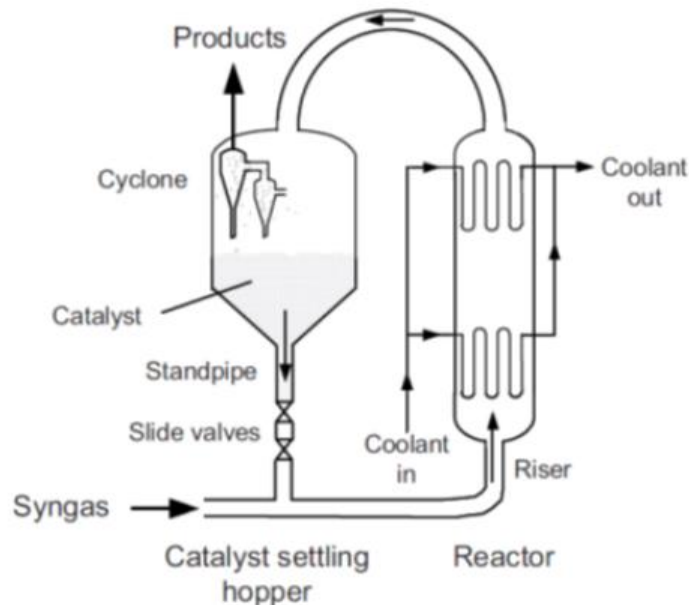


Figure 27. Circulating fluidized bed reactor. (10)

An alternative way to ensure an efficient heat transfer is to fluidize the catalyst bed and “move” it to the heat exchanger. This reactor design consists of two main zones: the reaction and the catalyst separation zone. In the reaction zone the syngas mixture is contacted with the catalyst particles and the reaction occurs: heat is removed by cooling water circulating in coils. The small catalyst particles are entrained by the gas flow and pushed upwards, towards the catalyst separation zone.

Here the cross section increases and the catalyst particles fall down, whilst the gaseous products are recovered from the top; a system of cyclones ensures an efficient gas-solid separation. The catalyst at the bottom of the separation zone is then sent back to the reaction zone for another cycle. The bed fluidization would be impossible if a liquid phase were involved: for this reason, the CFBR design is employed only in HTFT operations.

Table 4 Circulating Fluidized Bed Reactor: operating conditions.

Temperature [°C]	330
Pressure [bar]	20 ÷ 40
Active Phase of Catalyst	Iron

The main advantages of this reactor choice are as follows. The investment cost is lower compared to that of a MTFBR. The direct physical contact between catalyst particles and heat exchanger walls, along with the high flow rates needed to fluidize the system, contribute to a significant improvement in the temperature control, when compared to that of the MTFBR. The higher the heat transfer efficiency, the lower is the exchange area required and, in turn, the investment cost. Once the catalyst particles are fluidized, further increases in the space velocity do not affect the pressure drops, which are in any case lower than that of a fixed bed reactor: also, the compression costs are less. Furthermore, the fluidized bed operation makes the catalyst replacement easier and feasible on-line: losses due to down-time and labour intensive turn-arounds are in this way eliminated.

The main disadvantages of CFBR are linked to the small dimensions of the catalyst particles (100 μm). The latter are subjected to high mechanical stresses due to the high gas flow rates and the frequent collisions with the walls. Even though cyclone efficiencies are well above 99%, some of the small fines formed may be entrained by the gas flow exiting the reactor. For this reason, an additional separation unit based on oil scrubbing has to be placed downstream of the reactor: usually these units are complex and energy intensive, resulting in a lower thermal efficiency of the whole process.

1.2.7.3 *Slurry bubble column reactor*

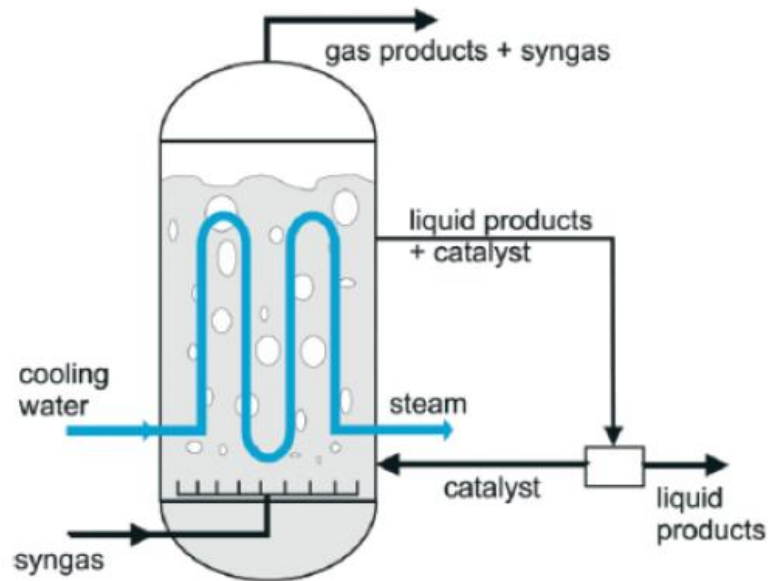


Figure 28. Slurry Bubble Column Reactor. (37)

The slurry reactor is another version of the fluidized bed reactor. However, differently from the latter, it is operated as a three-phase system. For this reason, the SBCR is preferred for wax production (LTFT). The finely divided catalyst is suspended in the product waxy medium and syngas bubbles upwards from the bottom of the reactor. The heat produced is removed by boiler feed water, which circulates in coils placed inside the reaction environment. The volatile hydrocarbons and unreacted syngas are recovered from the top, while the liquid, and the catalyst suspended in it, are sent to a separation unit where the catalyst is recovered and sent back to the reactor.

Table 5: Slurry Bubble Column Reactor: operating conditions

Temperature [°C]	200 ÷ 250
Pressure [bar]	25
Active Phase of Catalyst	Iron / Cobalt

The main advantages for this reactor design are as follows. The construction cost of equivalent capacity reactors is 40% less for the slurry (38): therefore, large scale design is

preferred. The excess liquid wax offers a large heat sink, which provides a very efficient temperature control and almost isothermal conditions in the entirety of the reactor. The pressure drop is significantly lower than that of the MTFBR and this translates to lower compression costs. As for the CFBR, the catalyst replacement is rather simple and can be done on-line.

Along with these advantages, there are also some important drawbacks. The catalyst-product

separation is challenging: the density difference between the two, that is about 0.7 [g/cm³] for Fe catalyst and 0.68 [g/cm³] for waxes, is too small to have a simple gravitational separation. The catalyst is subjected to high mechanical stresses. The presence of sulphur affects all the reaction environment, leading to a faster deactivation: in MTFBR these problems would only affect the initial part of the catalyst bed.

Table 6 recaps typical dimensions and operating conditions for the described conventional reactor designs:

Table 6: Typical dimensions and operating conditions of FT reactors (Fe catalyst). (10)

	Multitubular fixed bed reactor	Slurry-phase reactor	Circulating fluidized bed reactor
<i>Dimensions</i>			
Reactor height (m)	12	22	46
Reactor diameter (m)	3	5	2.3
Tube diameter (m)	0.05	—	—
Number of tubes	>2000	—	—
Catalyst size	1–3 mm	10–150 μm	40–150 μm
Reactor capacity (b/d)	600	2500	1500
Potential reactor capacity (b/d)	3000	30 000	8000 ^a
<i>Conditions</i>			
Inlet T (K)	496	533	593
Outlet T (K)	509	538	598
Pressure (bar)	27	15	22
H ₂ /CO feed ratio (mol/mol)	1.7–1.8	≥ 0.7	2.5–3

^aCapacities of CFB reactors at the Sasol II and III plants were 7500 b/d.

1.2.8 Overview of industrial Fischer-Tropsch processes

The objective of this paragraph is to provide an overview on the main process technologies aimed at the production on synthetic fuels and inspired to the original Fischer Tropsch process, with some differences in terms of catalyst, reactor and operating conditions.

Various companies are active today in FT research and development, but only few are currently running industrial processes:

Table 7: Currently operating and planned Fischer-Tropsch plants. (10)

Company	Location	Feedstock	Reactor (catalyst)	Operation	Current liquids output (b/d)
Sasol (I)	Sasolburg, South Africa	initially coal, currently natural gas	fixed bed (Fe) CFB (Fe) slurry (Fe)	1955 – present 1957–1993 1993 – present	5000
Sasol (Sasol Synfuels ^a)	Secunda, South Africa	coal, currently supplemented by natural gas	CFB (Fe) FFB (Fe)	1980–2000 1995 – present	160 000
PetroSA ^b	Mossel Bay, South Africa	natural gas	CFB (Fe)	1991 – present	30 000
Shell	Bintulu, Malaysia	natural gas	fixed bed (Co)	1993 – present	14 700
Sasol-Chevron/Qatar Petroleum (Oryx)	Ras Laffan, Qatar	natural gas	slurry (Co)	2007 – present	34 000
Shell/Qatar Petroleum (Pearl)	Qatar	natural gas	fixed bed (Co)	2011/2012	140 000
Sasol-Chevron	Escravos, Nigeria	natural gas	slurry (Co)	2013	34 000

^aFormerly Sasol II and Sasol III.

^bFormerly MossGas.

1.2.8.1 Processes based on conventional reactors

- *Sasol I*

The original *Sasol I* plant, based in Sasolburg (South Africa), went on-stream in 1955: it processed coal, of which South African has large reserves, producing synthetic fuels (5000 [bpd]). The plant design was rather complex, as it comprised both the high temperature and low temperature FT technologies. In the 2000s, the plant was readjusted to process natural gas instead of coal, becoming in effect a GTL plant for chemicals and waxes production.

Figure 29 shows the simplified flow block diagram of the original plant:

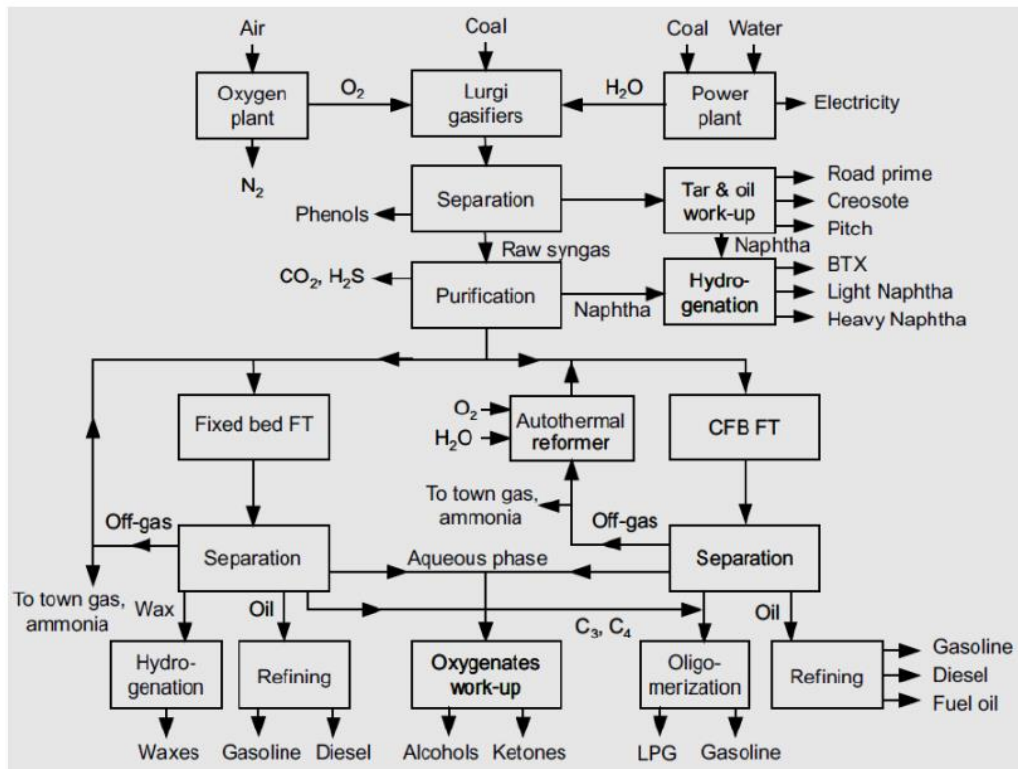


Figure 29 Simplified flow block diagram of Sasol I plant. (10)

Coal is gasified with pure oxygen, coming from the air separation unit, into a Lurgi reactor. The raw syngas produced is then cooled to remove water and tars, and purified from CO_2 , H_2S and hydrocarbons in the naphtha boiling range: the latter are hydrotreated and then blended into the gasoline pool or sold as BTX solvents. The purified syngas is sent to the FT reactors: the HTFT unit employs circulating fluidized bed reactors, while the LTFT unit adopts fixed bed reactors. The product effluent from the reactors is cooled and oil and water are condensed. While the aqueous phase is sent to the oxygenate recovery unit to produce alcohols and ketones, the hydrocarbon product is sent to the refining zone where valuable fuels are obtained. It is noteworthy to describe how the off gases from the different reactors are handled. The ones from the LTFT, being rich in syngas due to low conversions and a heavier product distribution for LTFT operations, are in part recycled directly to the fixed bed reactors. On the other hand, being the off gases from the HTFT rich in light hydrocarbons, they are sent to the autothermal reforming (ATR) unit where recycle syngas is produced.

- *Shell Middle Distillate Synthesis (SMDS) Process*

Shell has been the first company worldwide to build a GTL plant, targeting to the exploitation of the off-shore natural gas fields. Their first FT plant was constructed in Bintulu (Malaysia) in 1993 and produced 14700 bpd of liquid fuels.

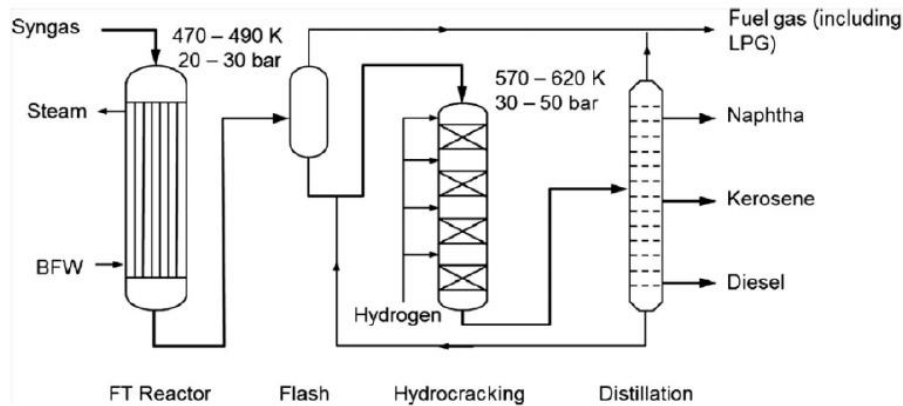


Figure 30. Simplified scheme of the SMDS process. (39)

The syngas is produced via partial oxidation of methane with oxygen: being the H_2/CO ratio attained below the required stoichiometric value for FTS (1.7 vs 2.15), the syngas composition is adjusted by mixing it with the hydrogen-rich syngas obtained by catalytic steam reforming of the methane produced in the FT reactors (27). The latter are multitubular fixed bed reactors containing over 10000 tubes filled with cobalt catalyst: this reactor and catalyst design, along with the low temperature, favour the production of waxes. The liquid product, after being separated from the light fractions, is heated up and sent to a mild hydrocracking unit. Here, transportation fuels are produced: the more severe the operating conditions in the hydrocracker, the lighter the product mixture. A subsequent distillation step separates the fuels according to their boiling range.

- *Pearl GTL*

Developed by *Shell* and *Qatar Petroleum* and based in Ras Laffan Industrial City (Qatar), Pearl is the world's largest GTL plant (40). It was built close to the world's largest single

gas reserve, the North Field in the Arabian Gulf, whose estimated capacity is more than 900 TCF of gas,

exploitable for about 100 years. The plant, started up in 2011, reached full production at the end of 2012 and today delivers 140 kbpd of product, despite its capacity of 260 kbpd.

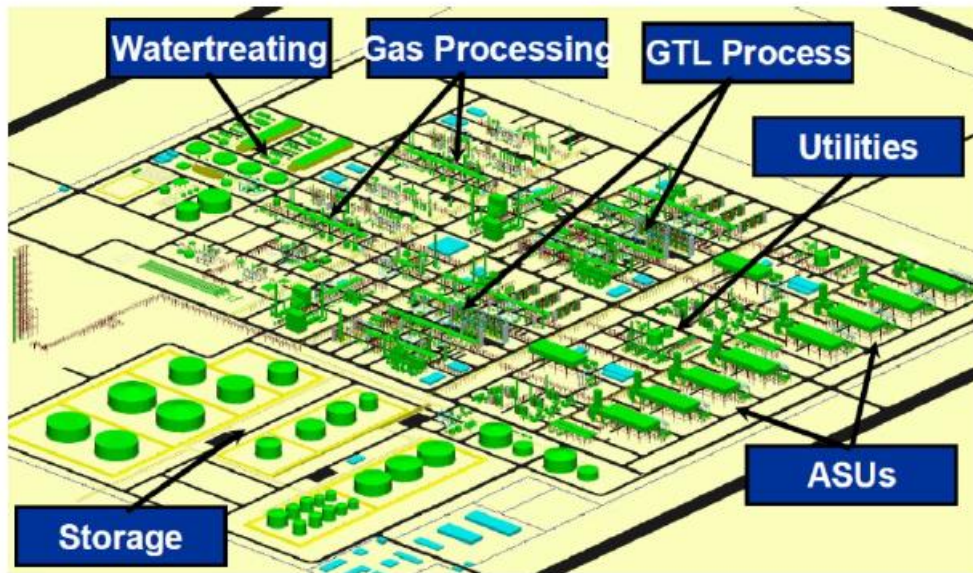


Figure 31. Pearl GTL project. (41)

Syngas is produced via methane partial oxidation and is sent to the synthesis zone, which consists of 24 water-cooled multitubular fixed bed reactors, weighing 1200 tons each, filled with 30 ÷ 100 tons of Co-based catalysts supported on SiO₂. The FT products are then hydrocracked and isomerized to diesel, aviation fuels and lubricants.

Being the world's largest plant, its figures are impressive (42): more than 40 distillation columns, about 2000 pumps and 50 compressors, 1000 online analysers and 14000 lab samples analysed per month.



Figure 32. Aerial view of Pearl GTL plant. (41)

1.2.8.2 Processes based on unconventional reactors

Conventional GTL and CTL (coal-to-liquid) processes require very high capital investments, in the order of billions of US dollars (37): in order to ensure a profitable operation over the plant lifetime, the production volumes must be at least about 30000 bpd. For this reason, these plants must be located close to sites which are very rich in fossil fuels reserves. The current distribution of natural gas reserves is however very scattered: very few are the large gas fields, whereas the number of small gas fields is increasing. In particular, only 6% of the gas reserves proven today would satisfy the lifetime capacity required by conventional GTL plants.

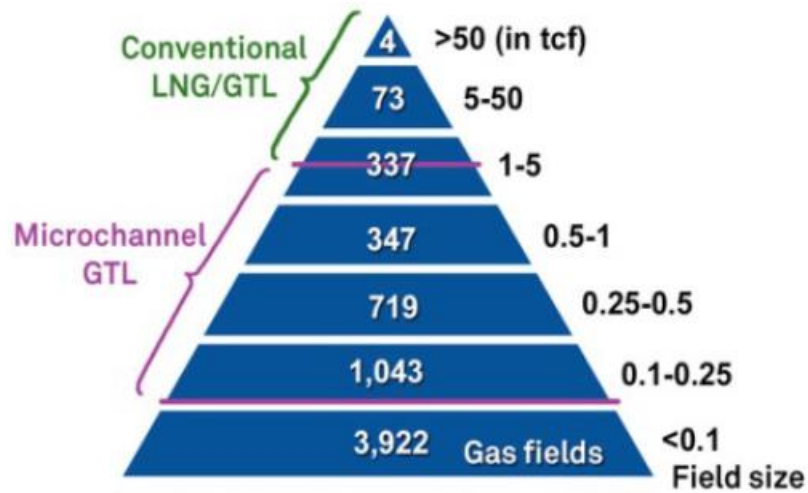


Figure 33. Worldwide distribution of natural gas reserves ([TCF] = Trillion Cubic Feet)

Today's process intensification aims to reduce plant size, thus reducing the capital cost while

maintaining the economic feasibility. Such smaller plants have the potential to exploit the small gas field, enabling a cheaper transportation of more valuable liquid products from remote sites in the world. In addition, small scale GTL technology would provide an alternative to *flaring* in the oil refining industry, which is strictly regulated and severely taxed.

Using compact reactors, the plant size can be easily adjusted to the available volumes of feedstock. These reactors have a standard design and, once manufactured in the workshop, they are mounted over sledges: the transportation in this way is less challenging, especially when they are to be sent to remote areas or installed in already existing gas extraction/processing rigs.

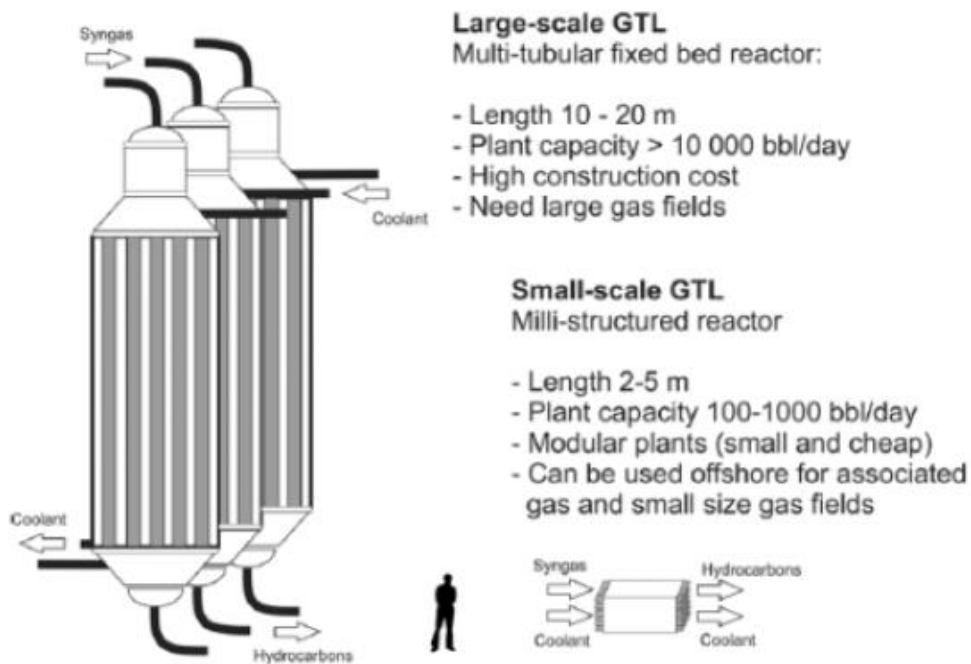


Figure 34. Comparison of large-scale and small-scale GTL reactors. (37)

- *Velocys technology*

Velocys Inc., headquartered in Ohio (USA), was the first company to launch on the market a novel technology which enables the exploitation of remote natural gas sources. This technology allows profitable operations of small scale FT plants, for volumes of production ranging from 1500 to 15000 bpd. Combining compact microchannel reactors and super-active catalysts, both fixed and variable costs are significantly reduced, compared to conventional GTL plants.

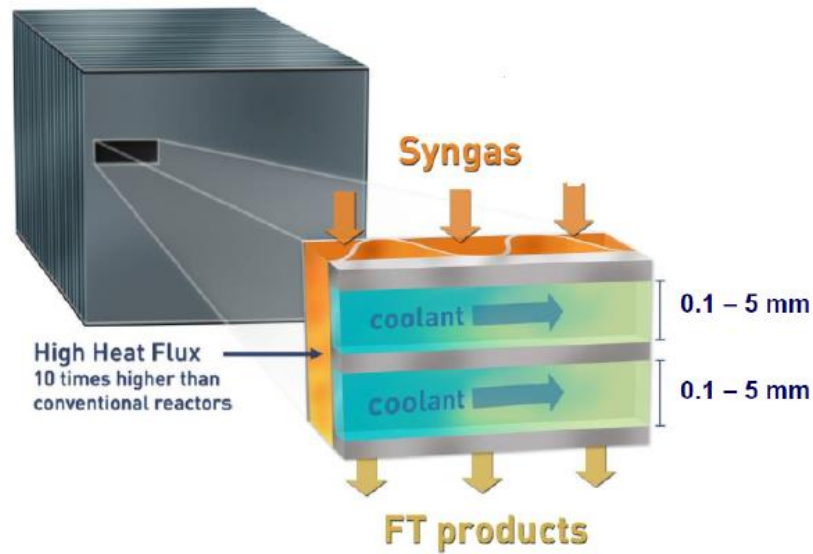


Figure 35. Microchannel reactor technology developed by Velocys Inc.. (43)

In contrast with the multitubular fixed bed, the microchannel reactor has thousands of channels loaded with catalyst and interspersed with water cooling channels (Figure 35): the small channels provide a high surface which allows fast and efficient heat removal, enabling the use of highly active catalysts. In particular, the company reports for such catalysts (Co-based) outstanding performances: conversions well above 90% and selectivity to liquid products over 87% in recycle configuration. Such performances, along with the efficient heat removal, make the small scale GTL technology profitable: currently *Velocys Inc.* is developing a plant (44) close to Ashtabula's harbour (Ohio, USA) aiming to produce 5000 bpd from the abundant reserves of Marcellus Shale, the largest natural gas field in the US.

- *Compact GTL technology*

The target of the technology developed by *CompactGTL*, a British company headquartered in Abingdon (Oxfordshire, UK), is to exploit stranded reserves of natural gas producing *syncrude* (to be mixed with crude oil), which is a high value product of easy transportability. To pursue this goal, two modular microchannel reactors are employed: the first converts natural gas into syngas, which is then converted to *syncrude* in the second reactor.

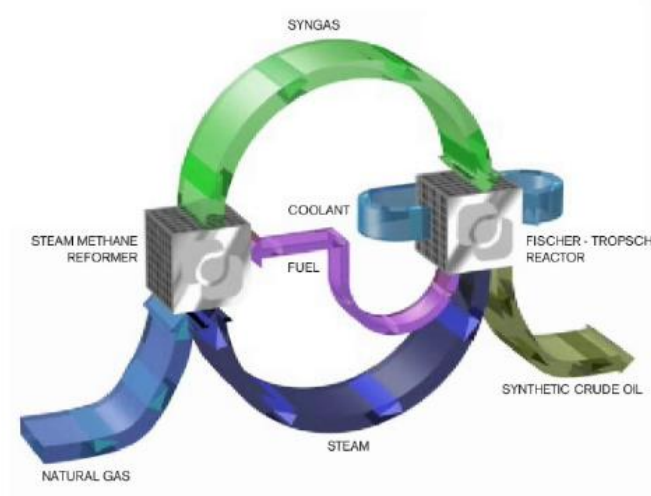


Figure 36. Production loop developed by Compact GTL.

As shown in Figure 36, the water produced in the second reactor is purified and then sent to the first, where it reacts with natural gas forming syngas (SMR= *Steam Methane Reforming*). The unconverted syngas and gaseous fractions produced in the second reactor are burned “shell-side” in the first, providing the heat needed for the endothermic SMR to proceed.

The main advantage is to have a self-sustaining plant, which does not require an air separation unit for oxygen production. In 2011, the first demonstration plant, commissioned by Petrobras, was built by *Compact tGTL* in Aracaju (Brasil) and today produces 20 bpd of liquid products.

- *ENI-IFP technology*

For some years until 2014, the catalysis group at *Politecnico di Milano*, in collaboration with *ENI (Ente Nazionale Idrocarburi)* and *IFP (Institut Français du Pétrole)* worked on structured multitubular reactors for Fischer-Tropsch synthesis. Enhanced heat removal and mass transfer, when compared to that of conventional packed bed reactors, are the key factors of this technology: metallic monoliths are employed due to their high thermal conductivity. In 2012, tests carried out on the monolith reactors showed very promising results: the group, in fact, performed a feasibility study for a demonstration plant with 20

bpd capacity. Unfortunately, the recent collapse in oil prices led these oil-and-gas companies to stall the investments in the project.

Bibliography

1. Organisation for Economic Co-operation and Development. Wikipedia, the free encyclopedia. [Online]
2. BP Statistical Review of World Energy June 2016. British Petroleum. [Online]
3. The 2016 outlook for energy: a view to 2040. Exxon Mobil. [Online]
4. Toyo Engineering Corporation: GTL (Gas to Liquids). Toyo Engineering Corporation. [Online]
5. C. G. Visconti, P. Forzatti. Studi e sperimentazione del processo di produzione di combustibili liquidi da carbone. 2011.
6. History of cobalt catalysts design for FTS. Bartholomew, C. H. s.l. : AIChE Natl. Spring Meet., 2003.
7. Analysis of Natural Gas-to-Liquid Transportation Fuels via Fischer-Tropsch. J. F. Goellner, V. Shah, M. J. Turner, N. J. Kuehn, J. Littlefield, G. Cooney, J. Marriott. s.l. : National Energy Technology Laboratory, 2013.
8. B. Y. F. Morales, B. M. Weckhuysen. 1, 2006, Vol. 19.
9. M. De Beer, A. Kunene, D. Nabaho, M. Claeys, E. Van Steen. 2, 2013, J. S. Afr. Inst. Min. Metall. , Vol. 114, pp. 157-165.
10. J. A. Moulijn, M. Makkee, A. E. Van Diepen. Chemical Process Technology. Sec. Ed. Wiley. Hoboken, New Jersey : John Wiley & Sons Ltd, 2013.
11. Tronconi, E. Lecture 8: Fischer-Tropsch Synthesis. Course of Industrial Organic Chemistry. 2016.
12. Schulz, H. 2003, Top. Catal., Vol. 26, pp. 73–85.
13. P. Winslow, A. T. Bell. 1, 1984, J. Catal., Vol. 86, pp. 158-172.
14. E. Iglesia, S. C. Reyes, R. J. Madon. 1, 1991, J. Catal., Vol. 129, pp. 238-256.
15. Dry, M.E. 1996, Appl. Catal. A Gen., Vol. 138, pp. 319-344.
16. H. Pichler, H. Buffleb. Synthesis of Paraffin Wax on Ruthenium Catalysts at Pressures up to 100 atmospheres. Brennstoff-Chem. 1940, Vol. 21.

17. I. Wender, H. W. Sternberg, M. Orchin. 1952, *J. Am. Chem. Soc.*, Vol. 74, pp. 1216–1219.
18. E. Van Steen, H. Schulz. 1999, *Appl. Catal. A Gen.*, Vol. 186, pp. 309-320.
19. S. Shetty, A. P. J. Jansen, R. A. Van Santen. 36, 2009, *J. Am. Chem. Soc.*, Vol. 131, pp. 12874–12875.
20. Adesina, A. A. 2, 1996, *Appl. Catal. A Gen.*, Vol. 138, pp. 345-367.
21. M. Ojeda, R. Nabar, A. U. Nilekar, A. Ishikawa, M. Mavrikakis, E. Iglesia. 2, 2010, *J. Catal.*, Vol. 272, pp. 287-297.
22. Flory, J. 10, 1936, *J. Am. Chem. Soc.*, Vol. 58, pp. 1877–1885.
23. R. B. Anderson, R. A. Friedel. 1949, *J. Am. Chem. Soc.*, Vol. 72, pp. 1212–1215.
24. G. P. van der Laan, A. A. C. M. Beenackers. 3-4, 1999, *Cat. Rev.*, Vol. 41, pp. 255-318.
25. O. O. James, B. Chowdhury, M. Adediran, S. Maity. 2012, *RSC Adv.*, Vol. 2, pp. 7347-7366 .
26. Fratolocchi, L. Preparazione e analisi di reattività di un catalizzatore eggshell Co/Al₂O₃ per la sintesi di Fischer-Tropsch. s.l. : Politecnico di Milano, 2013.
27. Dry, M. E. 2002, *Catal. Tod.*, Vol. 71, pp. 227-241.
28. Wojciechowski, B. W. 4, 1988, *Cat. Rev.*, Vol. 30, pp. 629-702 .
29. T. J. Donnelly, I. C. Yates, C. N. Satterfield. 6, 1988, *Energy Fuels*, Vol. 2, pp. 734–739.
30. E. Kuipers, I. H. Vinkenburg, H. Oosterbeek. 1, 1995, *J. Catal.*, Vol. 152, pp. 137-146.
31. Iglesia, E. 1997, *Appl. Catal. A Gen.*, Vol. 161, pp. 59-78.
32. Erkey, Rodden, Akgerman. 3, 1990, *Energy Fuels*, Vol. 4, pp. 275–276.
33. H. Song, D. Ramkrishna, S. Trinh, H. Wright. 2, 2004, *Korean J Chem Eng.*, Vol. 21, pp. 308–317.
34. E. W. W. Kuipers, C. Scheper, J. H. H. Wilson, I. H. H. Vinkenburg, H. Oosterbeek. 1996, *J. Catal.*, Vol. 158, pp. 288-300.
35. Upgrading of Fischer-Tropsch Products to Produce Diesel. D. Leckel, H. Tropsch. 2010.
36. D. Leckel, H. Tropsch. Upgrading of Fischer-Tropsch Products to Produce Diesel. Haldor Topsoe Catal. Forum. 2010, August.

37. B. Todić, V. V. Ordonsky, N. M. Nikačević, A. Y. Khodakov, D. B. Bukur. 2015, Catal. Sci. Technol., Vol. 5, pp. 1400-1411 .
38. B. Jager, R. Espinoza. 1, 1995, Catal. Today, Vol. 23, pp. 17-28.
39. Gas-to-liquids projects gaining momentum as process list grows - Oil & Gas Journal. Ogj. [Online]
40. The world's largest GTL plant - Shell Global. Shell . [Online]
41. Hoek, A. 8, 2005, Vol. 77.
42. Holmen, A. Lecture 4: Fischer-Tropsch Synthesis. NTNU : s.n., 2015.
43. S. LeViness, S. R., Deshmukh, L. A. Richard, H. J. Robota. 2014, Top. Cat., Vol. 57, pp. 518–525.
44. Velocys Project.
45. Toyo Engineering Corporation: GTL (Gas to Liquids). Toyo Engineering Corporation. [Online]
46. R. Guettel, U. Kunz, T. Turek. Reactors for Fischer-Tropsch synthesis. 2008. Vol. 31.

Chapter 2

State of art

Passivation of highly air sensitive transition metal catalysts is often used to preserve reduced or spent catalysts to allow transfer of samples from the reactor vessel to conventional characterization instruments. This process allows the characterization of the catalyst in a state which resembles the activated state. Furthermore, passivated samples can be stored under ambient conditions. Passivation is reported to avoid or at least suppress rapid and violent oxidation by air, which results in phase changes and local temperature hot spots. The latter can become a safety hazard in the case of pyrophoric materials and industrial catalysts are typically removed from the reactor under inert gas or after passivation. The passivation treatment fundamental for the cobalt-based catalysts used for the Fischer-Tropsch synthesis. Generally, the passivation treatment allows deposit of a protective thin film of Co oxides on the metallic catalyst surface. The film has a thickness of few nanometres and allows delaying the oxygen penetration. The characterization of the spent FT catalyst is necessary to understand the properties of the catalytic material during and after the Fischer-Tropsch synthesis. For example, to identify the different causes of the catalyst deactivation during FTS (Figure 1).

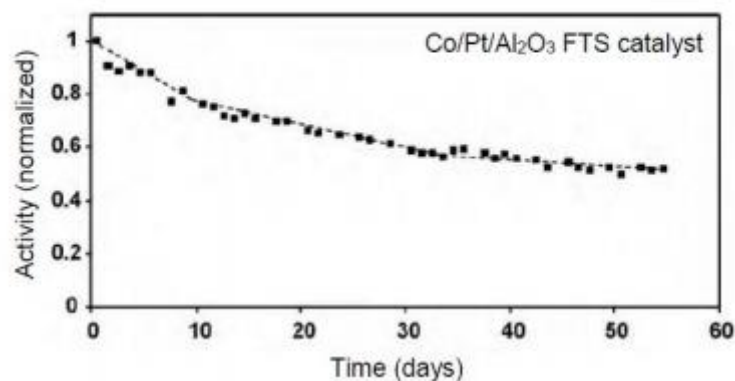


Figure 1. Activity for a Co/Pt/Al₂O₃ catalyst during FTS in a 100-barrel/day slurry bubble column reactor (230°C, 20 bar, H₂+CO conversion of 50 ÷ 70%, feed gas composition of 50 ÷ 60 vol.% H₂ and 30 ÷ 40 vol.% CO) (1).

The passivation treatment can be also used to carry out the reduction process and the reactivity test in different reactors. In this regard, it may happen that the reduction conditions used for conventional Co-based catalysts cannot be reached in the same reactor dedicated to the assessment of the catalytic performances. In particular, the reduction process is carried out at significantly higher temperatures $350 \div 450$ °C than those used during FTS ($200 \div 250$ °C). Accordingly, it's necessary to conduct the reduction and so the passivation steps in one separate reactor and then load the catalyst in the passivated form into the operating Fischer-Tropsch reactor.

In this chapter, an overview on the based catalysts used for the FTS and on the Co oxidation, reduction and passivation processes will be given.

2.1 FT catalysts

The metals considered for FTS applications are: nickel, cobalt, iron and ruthenium. This is due to their level of activity. Depending on the application, the criteria to select the most suitable catalyst are the price of the active metal, the desired final products and the carbon source for synthesis gas production. Ruthenium is not present in commercial usage because, despite the fact it is the most active metal in the FTS, it has low availability and high cost. Due to its excessive hydrogenation activity, nickel produces too much methane for viable operations (2). In addition, when exposed to typical FTS pressures, nickel forms volatile nickel carbonyls. This results in loss of catalyst from the reactor and deactivation. This leaves cobalt and iron as the most promising candidates for industrial operations.

Cobalt is the catalyst preferred for operations at $200 \div 240$ °C, (Low Temperature Fischer-Tropsch synthesis, LTFT), which favours the formation of heavier hydrocarbons (e.g., waxes) that can be upgraded to the diesel and jet fuel range. For the production of gasoline and high-value α -alkenes, iron catalysts operating at temperatures between 300 and 350°C (High Temperature Fischer-Tropsch, HTFT) are deemed the best options. Iron-based catalysts have high water-gas-shift (WGS) activity. This makes them suitable for synthesis gas with low H_2/CO ratios, i.e., from coal or biomasses feedstock, where the ratio is considerably lower than the consumption ratio of the FT reaction ($H_2/CO= 2.15$). The WGS activity of Co-based catalysts, instead, is low. Therefore, these catalysts are used when the synthesis gas is produced from natural gas, which gives H_2/CO ratios close to the stoichiometric value of 2.15 (3). Notably, LTFT has several advantages with respect to

HTFT. In this regard, LTFT produces hydrocarbon products that are less energy intensive to upgrade and premium quality fuels with high cetane number (up to 75) related to ignition delay time in diesel engines. Furthermore, the greenhouse gas emissions are quite low (lower $C_1 \div C_4$). In contrast, HTFT to target gasoline range fuels results in hydrocarbons with poor octane rating and, due to the lower chain growth probability factor, significantly more methane and other light gases are produced.

The LTFT synthesis carried out over cobalt based catalysts is the focus of this thesis and thus only this kind of catalyst will be considered in the remainder of this thesis.

2.1.1 Cobalt-based catalysts

The currently used Co based catalysts are made of promoted cobalt dispersed on an oxide support, and thus similar to the ones prepared by Fischer and Tropsch. The FTS occurs on the surface cobalt metal centres (Co^0). This metal is an expensive material and thus it is important to obtain a suitable dispersion on the catalytic support. From the particle size, catalyst morphology, extent of reduction, and particle stability depends on the number of Co^0 surface sites (4). After the catalyst activation step, the extent of reduction should be greater than 60%, even though the cobalt may undergo further reduction during the FTS reaction. An optimum cobalt particle size of around $8 \div 10$ nm is preferred as particles below this range have a lower turnover frequency (TOF) (4). Furthermore, very small particles ($4 \div 6$ nm) are prone to deactivation and are also difficult to reduce due to the increased metal-support interaction (4). The two most common phases of metallic cobalt in supported cobalt FTS catalysts are face-centered cubic (fcc) and hexagonally close-packed (hcp), which often coexist. It is reported that for cobalt particles less than 40 nm, the predominant phase should be fcc (4). The relative amounts of these phases may be influenced by the activation procedure, the addition of promoters, and the type of support used (5). Catalysts are often promoted with a second metal (i.e., noble metals) which leads to the improvement of the reducibility of the cobalt oxide particles formed after the calcination step involved in the catalyst synthesis procedure (4). This results in an increase in the number of active sites available for the FTS, thus resulting in higher CO conversion per gram of catalyst compared to unpromoted catalysts. The more facile cobalt reduction is attributed to faster hydrogen activation in the presence of promoter metals and subsequent spillover of hydrogen to cobalt oxides and reduction of cobalt species (5). Often, the

promotion with noble metals plays a key role to achieve small average size of either cobalt oxide or cobalt metal particles. Structural promoters, such as Zr and La, are usually also added to improve the stability of Co. Two are the main functions of the catalyst support: the cobalt dispersion and the production of stable cobalt metal particles in the catalysts after reduction. Mechanical strength and thermal stability to the catalyst are also provided by the support. Robustness is also an important characteristic of the support. Accordingly, resistance to attrition is required under FTS conditions, especially in a slurry bubble-column environment. The most used supports for FTS catalysts are silica (SiO_2), alumina (Al_2O_3) and titania (TiO_2). These oxide supports are characterized by a high surface area. When Al_2O_3 is used, the interaction between the support and cobalt may take place. Therefore, mixed compounds inactive in the FTS, such as cobalt-aluminate, can be formed. In contrast with titania and silica these interactions are weaker. In particular, Co- TiO_2 interactions can occur depending on the catalyst formulation (6).

Cobalt-based FT-catalysts are usually prepared via impregnation or co-precipitation. The impregnation technique is the preferred one (5). It consists in depositing a solution containing dissolved cobalt precursor on a dry support. One impregnation procedure is the “Incipient Wetness Impregnation” (IWI) method. In the IWI method the impregnating solution containing the cobalt salt, typically cobalt nitrate, is contacted with a dry porous support. After being contacted, the solution penetrates in the pores of the support by capillary action. The condition for the incipient wetness to occur is that the pores of the support are all filled with the liquid and there is no excess of moisture. Another impregnation technique used to deposit cobalt onto the support is the slurry (wet) impregnation, which uses an excess of liquid in the pores of the supports (5). The support is usually added to the impregnating solution heated at $60 \div 120^\circ\text{C}$, to yield a slurry, which is constantly stirred. The slurry impregnation method is often preferred in industry over incipient wetness impregnation because the distribution of cobalt particles results more uniform at high cobalt loadings (e.g., $20 \div 25\%$ by weight cobalt) (7).

The co-precipitation method is predominant in the preparation of iron FT catalysts, while it is not common for cobalt-supported catalysts (5). The catalyst preparation based on co-precipitation is performed by following four steps: precipitation, washing, drying, and shaping. Chemical precipitation of the cobalt, promoter, and support by a precipitation agent (i.e., Na_2CO_3 or KOH) can be done batchwise or continuously at constant pH.

Temperature, precipitation agent, precursor salts, structure directing, or organic hydrolysis reagents, aging time, and reaction atmosphere control the crystallite size and composition of the precipitate. Filtration and washing of the precipitate are made to ensure that excess chemicals are removed (4). The last step of the co-precipitation, the shaping of the catalyst precursor, differs with the reactor application.

Drying and calcination are usually carried out after the impregnation or co-precipitation step. During these thermal treatments it is important that the cobalt distribution achieved by impregnation or precipitation is preserved. In order to do that, the cobalt mobility must be hindered. For catalysts obtained by impregnation from cobalt nitrate solutions, more attention has to be paid during the calcination process. An exact calibration of the heating rate, temperature and air flow should be made to remove the water and NO_x immediately.

2.1.2 Composition of industrial Co-based catalysts

At the industrial scale, Co-based catalysts are employed by Sasol and Shell for the Slurry Phase Distillate (SPD) process and Shell Middle Distillate Synthesis (SMDS) process. The composition of these catalysts is shown in Table 1. The new generation Shell catalyst is supported on TiO₂ pellets, while the previous catalyst was supported on SiO₂ modified with some Zr and possibly other rare earth oxides ((8) (9) (10) (11) (12)). Two methods are used for the preparation of the patented Shell catalysts: the kneading or incipient wetness impregnation (IWI) methods. However, the kneading is the preferred method. It consists in mixing the support with the aqueous solution containing Co-nitrate salt and in applying an intensive mechanical treatment such as pressing, squeezing or wringing, to form a paste. This paste is then dried and calcined in air at 500°C.

When the impregnation procedure is adopted, it is repeated several times until the desired Co loading is obtained. After each impregnation step, the material is dried and calcined in air at 500°C. The impregnating solution containing the cobalt precursor salt is usually aqueous. However, it is modified with the addition of “delaminating” agents, i.e., citric acid, in one example shown in the Shell patent of 2010 (11). The inventors reported that the function of the citric acid was the improvement of the cobalt dispersion on the support. The Sasol catalyst is said to be Pt-Co/Al₂O₃ (13; 14; 15; 16). Cobalt catalysts patented by Sasol are supported on alumina modified with silica. In addition to cobalt, the catalyst components include platinum as promoters. The preferred catalysts preparation method is

the slurry impregnation, which involves the impregnation of the support with an excess volume of impregnating solution containing both Co and Pt-precursors. The impregnation step is repeated twice. Each impregnation step is followed by drying and calcination under a controlled air stream at maximum 250 °C.

Table 1. Composition of commercial Co-based FT catalysts [20-25].

	Shell SMDS	Sasol SPD
Active metal	Co	Co
Support	SiO ₂ (old), TiO ₂ (new)	γ-Al ₂ O ₃
Reduction promoter	-	Pt
Rare earth oxides	Zr, Ti, Cr (old) Mn (new)	SiO ₂
Co loading	10 ÷ 30 g of support	10 ÷ 30 g per 100 g of support
Reduction promoter loading	-	Pt: Co molar ratio < 1:100

Numerous patents, probably more than 100 U.S and foreign patents, are also assigned to Exxon for FT Co-based catalysts formulations (17). Most of the catalysts developed by Exxon are composed of cobalt dispersed on TiO₂ support and additives that function as structural (metal oxides) or activity (noble metals) promoters. The support contains primarily TiO₂, which, in many cases, is doped with a low content of silica or alumina.

Recently, Velocys patented a new cobalt-based FT catalyst to use in structured microchannel reactor systems [34]. The catalyst is supported on silica modified with 16wt.% of TiO₂ and is comprised of 42 wt.% of Co, 0.2 wt.% of Re and 0.03 wt.% of Pt. The preparation method refers to the patent of Oxford Catalysts Group (18) and it is based on the addition of the support in a warm solution containing:

- the Co-nitrates precursor salt
- the precursors of the promoter
- a low content of water
- an organic compound, such as urea, citric acid or acetic acid (18).

Then, the obtained material is heated in an oxygen-containing atmosphere to 100 °C and 250 °C for 5 and 3 h, respectively (heating rate of 2°C/min). In the example cited in the Velocys patent (19), the catalyst is prepared by following four impregnation steps of a solution containing Co and Re precursors. Each impregnation is followed by drying and calcination. Citric acid is chosen among the proposed organic compounds and it is added in the impregnating solution in the last three-impregnation steps. A further impregnation step is carried out on the obtained material to deposit Pt on the catalyst (19).

2.2 Cobalt oxidation

Cobalt-based catalysts are known to possess a variety of coordination and oxidation states and hence spectroscopic techniques are well suited for their characterisation (20).

Cobalt has the electron configuration $[\text{Ar}] 3d^7 4s^2$ and the most commonly found oxidation states are 0, +2, +3 and +4. Co^{2+} (d^7) is cobalt most common valence state, which can adopt high-spin octahedral (CoO nanocages) and tetrahedral (CoAl_2O_4) coordination environments. Co^{3+} (d^6) is also present in octahedral coordination (LaCoO_3) but on rare occasions is also found in the tetrahedral coordination. Co^{4+} (d^5) is less stable and only observed as intermediate during catalysis, particularly in electrocatalytic water splitting.

The normal spinel structure of Co_3O_4 has two distinct Co sites in a two-formula-unit face-centered-cubic (fcc) primitive cell. One site is occupied by a Co^{2+} ion, which is surrounded by a tetrahedral O^{2-} coordination sphere, while another site is occupied by Co^{3+} ions and is in an octahedral environment surrounded by six O^{2-} ions (Figure 2a). In contrast, the single valence compounds, Co_2O_3 (six-formula-unit cell) and CoO (two-formula-unit cell), exist in a weakly symmetric crystal structure, namely, orthorhombic and monoclinic, respectively. In Co_2O_3 , an octahedral environment of O^{2-} ions surrounds each Co^{3+} ion. In CoO , Co^{2+} is also surrounded by an octahedral environment of O^{2-} ions, unlike the tetrahedral O^{2-} environment in Co_3O_4 (Figure 2b,c) (21).

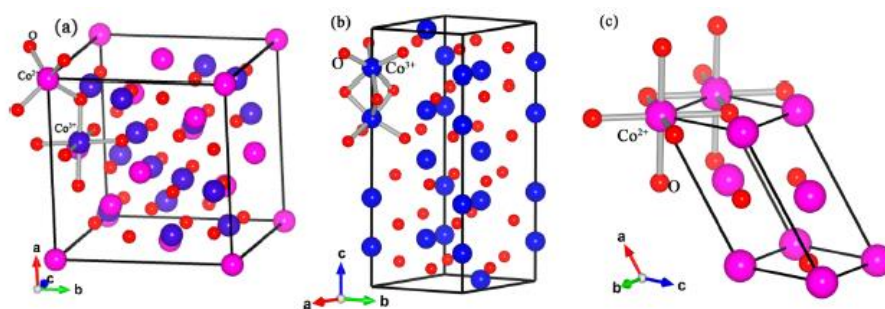


Figure 2. (a) Fcc of Co_3O_4 with Co^{+2} and Co^{+3} ; (b) Orthorhombic Co_2O_3 with Co^{+3} ; (c) Monoclinic CoO with Co^{+2} .

In recent years, several authors have shown that oxidation of metallic nanoparticles, made of Co leads to the formation of hollow oxide spheres (22). The understanding about void formation in a reaction between two solids or a solid and a liquid/gaseous reactant is known. At the base of this lies the *Kirkendall effect*, which is a consequence of the different diffusion rates of cobalt and oxygen through the oxide. The Kirkendall effect is described as the movement of the interface between a diffusion couple i.e., copper and zinc in brass, as the result of the different diffusion rates of these two species at elevated temperature (23). In the case of metals mentioned above, the formation of hollow structures is attributed to the faster outward diffusion rate of the metal cations compared to the inward diffusion of the anions and this difference in diffusion rates creates vacancies which coalesce into voids.

In an oxidizing environment, the initial oxidation process leading to the formation of hollow spheres is explained by Cabrera–Mott theory of metal oxidation (24). According to this theory, oxygen first adheres to the surface of the metal resulting in the formation of a thin oxide layer. Electrons tunnel through the oxide layer and ionize the oxygen leading to an electric field between the metal and the surface of the oxide layer. This electric field is the driving force for the outward diffusion of the metal cation. Even though the diffusion of the metal is faster, there is inward diffusion of oxygen as well which can be enhanced at grain boundaries of the oxide layer. This is proven by the fact that the diameter of the void formed is generally smaller than the size of the initial metal particle size, found to be 40 to 70% less. The effect of size of metal on the oxidation process has been studied for well-defined nickel nanoparticles and it was observed that smaller particles oxidize faster than larger ones. The oxidation is carried out at high temperature between 200 and 500 °C. Another study of Wang et alia has shown that iron nanoparticles of size 8 nm oxidised

completely at room temperature to form hollow shells, while the larger particles formed core–shell structures (25).

Figure 3 shows a schematic picture of this oxidation mechanism for a cobalt nanoparticle. After formation of a thin oxide shell, further oxidation proceeds by outward diffusion of cobalt cations through the oxide shell, which is much faster than the inward diffusion of oxygen anions. The vacancies created in the cobalt core coalesce and form voids inside the oxide shell. After completion of the oxidation process, a hollow, polycrystalline oxide shell is formed (22). In this way, the oxidation mechanism leads to transport of cobalt away from its original location, spreading it over the support.

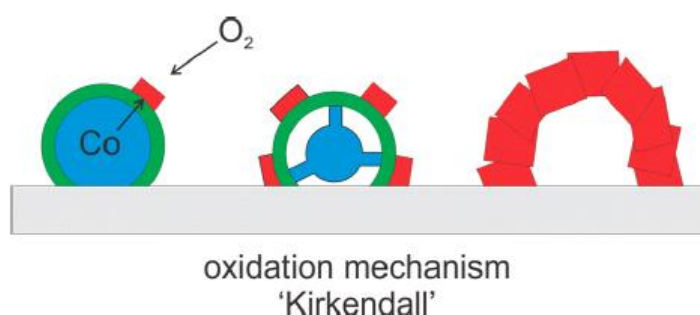


Figure 3. Oxidation of a supported Co nanoparticle. After completion of the first thin oxide layer, oxidation proceeds via fast outward diffusion of cobalt, ultimately creating a polycrystalline oxide shell.

The formation of hollow cobalt oxide spheres has been observed for cobalt both in the unsupported (colloidal nanoparticles in solution) or supported form (cobalt nanoparticles supported on montmorillonite).

Cobalt oxidation is strictly dependent on the temperature (Figure 4). At relatively low temperatures, the Co metal starts being oxidized to CoO, while the oxidation of CoO to Co₃O₄ only starts at about 300 °C after CoO reaches a maximum. At the end, all Co metal has been oxidized, and mainly Co₃O₄ is present (26).

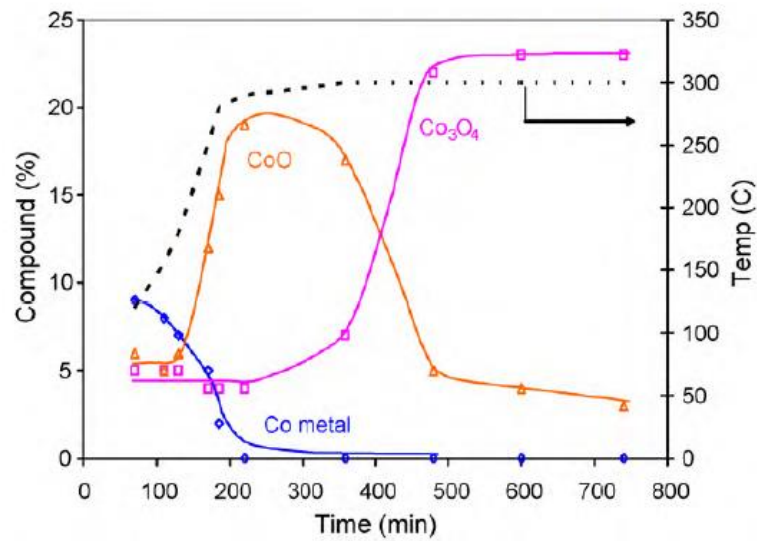


Figure 4. XRD phase analyses shows the different stages of oxidation.

Ha et al. report the structural changes and diffusion processes during the chemical transformation of ϵ -Co (ferromagnetic hcp structure) nanoparticles through the oxidation in air into CoO and Co₃O₄ (27) (28) at 200 °C for 1 h. The initial Co sample shows a core-shell structure, which is formed by cobalt and cobalt oxide. This is due to immediate surface oxidation after exposure to air, shown in Figure 5.

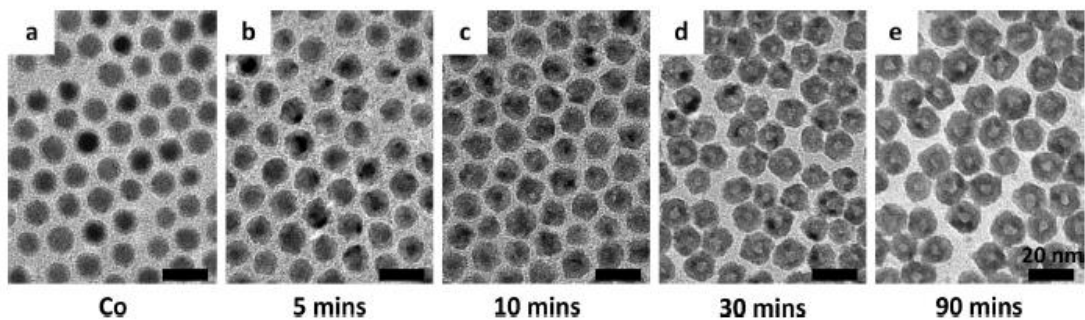


Figure 5. TEM images of the samples during the oxidation at 200 °C in air. (a) The initial ϵ -Co are spherical with an oxide shell. The samples are oxidized for 5 (b), 10 (c), 30 (d), and 90 min (e) and transform to a hollow structure with an irregular faceted morphology.

The CoO is not detected by XRD but is only visible with TEM technique. After the sample is oxidized for 5 minutes, the XRD detects a peak that corresponds to CoO phase in the following figure.

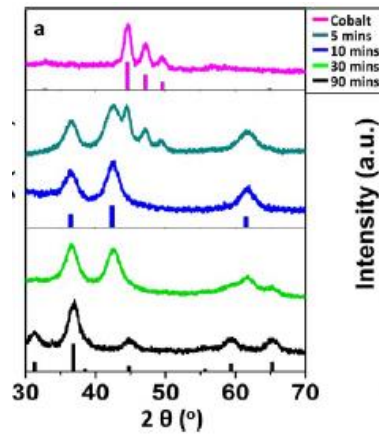


Figure 6. XRD shows the pink, turquoise, blue, light green, and black lines that represent the starting cobalt, oxidized for 5, 10, 30, and 90 min samples, respectively. The XRD patterns of the samples during the oxidation show a gradual transition from the ϵ -Co phase (pink bars) to CoO (blue bars) and Co₃O₄ (black bars).

According to the Figure 7, the calculated Co-O phase diagram for 10-nm particles confirms a much-diminished stability field for the divalent oxide (29). The stable phase is Co₃O₄ at 200 °C in air for both bulk and nanomaterials (30), but Co should transform to CoO before Co₃O₄, since the transformation to Co₃O₄ is much slower than that to CoO (31). The reverse process is observed in the system under reduction conditions (32; 33).

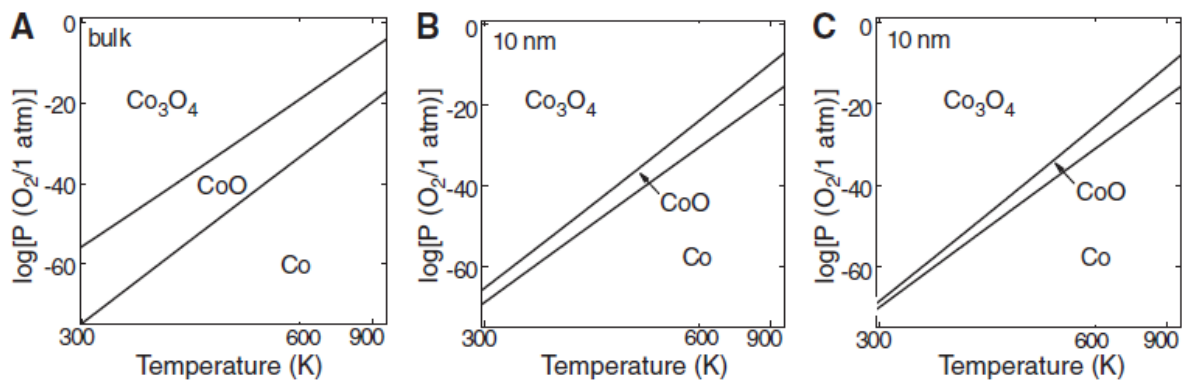


Figure 7. Calculated phase diagrams for bulk and 10-nm-diameter spherical particles. (A) Co-O (bulk). (B) Co-O (anhydrous 10-nm particles). (C) Co-O (hydrated 10-nm particles). The temperature scale is in $1/T$, in order to make a linear plot, although the labelled temperatures are in T (kelvin).

From a kinetic point of view, the oxidation from Co to CoO is extremely fast and the it slows down.

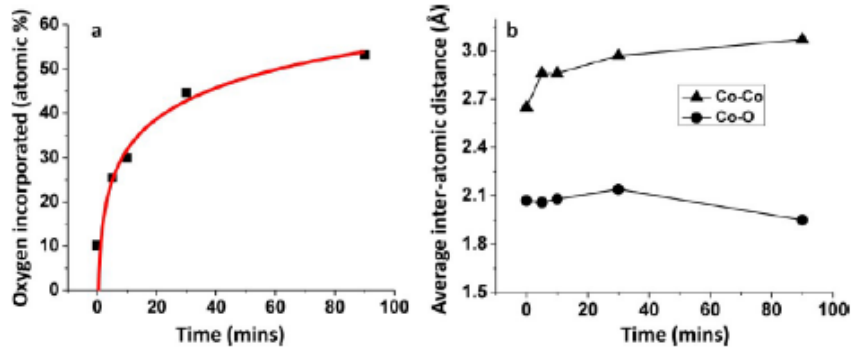


Figure 8. Oxygen concentration and the average interatomic distances of the samples during the oxidation process. A) The oxygen concentration based on the EXAFS fitting model increase logarithmically and are well-fit with the logarithmic function ($(\text{oxygen } \%) = 8.5 + 10 \cdot \ln(\text{oxidation time})$, $R^2 = 0.97$). B) The filled triangles and filled circles represent the Co–Co interatomic distances and Co–O interatomic distances, respectively.

In Figure 8(a) is shown the kinetics of oxygen diffusion: the rate of diffusion increases with increasing the oxidation time. The Co-O interatomic distance is relatively constant from the beginning of the bond formation and the Co-Co interatomic distance increases roughly parabolically as a function of the oxidation time (Figure 7(b)).

Table 2. Formation Energy, Migration Barrier, and Diffusion Activation Barrier for Co and O Diffusing Through ϵ -Co^a

diffusion type	formation energy (eV)	barrier to migration (eV)	diffusion activation barrier (eV)
$\text{Co}_{(i)}-\text{V}_{(i)}$	1.39	0.08	1.47
$\text{O}_{(i)}-\text{V}_{(i)}$	1.02	0.21	1.23
$\text{O}_{(int)}-\text{O}_{(int)}$	-0.81	2.53	1.72
indirect exchange	-0.18	1.06	0.88

^aFor the indirect exchange, the formation energy is based on the structure with O in a Co vacant site (Figure 6a) and the barrier energy to migration refers to the highest barrier energy in the diffusion steps shown in Figure 6b–d.

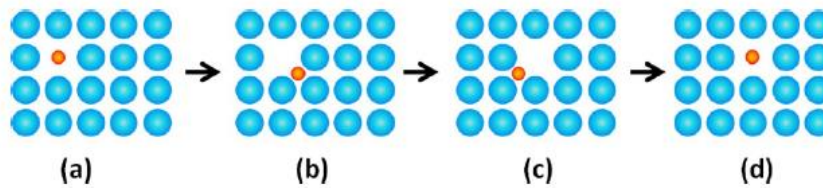


Figure 9. Proposed indirect exchange mechanism of O diffusion in the ϵ -Co phase takes place over three steps (a)–(d): (a)–(b) O atom in a vacant type I site diffuses to an adjacent interstitial site; (b)–(c) neighbouring type I Co atom diffuses to site vacated by O; (c)–(d) O hops back into the empty type I site.

The diffusion mechanism is complex (Figure 9). The first step assumes that a substitutional O atom on a vacancy site move to an adjacent interstitial site, then there is the migration of a neighbouring Co atom into the now vacant site. At the end, the O atom migrates to the previous abandoned site by moved Co atom. The O diffusion in the ϵ -Co occurs via an indirect mechanism of Co and O atoms and the O diffusion is faster than Co ones. Once the amount of O is enough, CoO is formed. The fast diffusing species then switches from O to

Co: the Co diffuses faster in the CoO phase than O. Some characterization analysis as TEM, EXAFS and XRD confirms the two-step mechanism: for the first 5 minutes no hollow structures are present, hence the O is still diffusing inward faster than the Co diffusing outward. After 10 minutes, the dominant phase is CoO so Co diffuse faster than O, resulting in the hollow structures.

The mechanism of the transition from CoO to Co₃O₄ is quite different from that of Co to CoO. Co atoms are the mobile species while the O atom remains stable due to the low diffusivity of O atoms in the CoO phase. Ha et al. note an increase in size of the samples through TEM analysis: this is due to the lower density of the Co₃O₄ phase respect with the CoO phase. There is also the formation of more cobalt oxide on the surface that changes the stoichiometry: the excess of Co from CoO migrates to the outer surface forming O-rich Co₃O₄ phase due the exposure to O atoms in air.

Jung et al. conduct different studies through a precise single-phase Raman identification analysis on the deposition temperature (125 ÷ 300 °C), precursor and reactant, pulsing times and post-annealing that control growth of the high quality single-phase Co₃O₄ (34). The Co₃O₄ phase is formed in a spinel structure, identified with XRD, with a high deposition temperature above 265 °C, while the rock-salt CoO phase disappeared at the same conditions. These studies confirm that CoO_x films deposited within the temperature range of 150 ÷ 250 °C have a mixed phase comprising both CoO and Co₃O₄. The phase transition from CoO and Co₃O₄ mixed phase to single phase Co₃O₄ occurs at the deposition temperature of 265 °C. In reactant (O₂) pulsing condition, an excess of supply of Co metalorganic precursor with respect to the reactant O₂ helped form the CoO phase due to high Co/O ratio, but it also helps the conversion from the mixed phase CoO and Co₃O₄ to the single phase Co₃O₄. In the post-annealing in oxidising ambient, only the single phase Co₃O₄ results for temperature above 350 °C.

For the mixed phase CoO and Co₃O₄, Zyla et alia investigate on the kinetics and mechanism of Co₃O₄ formation in the interior oxidized CoO substrate (35).

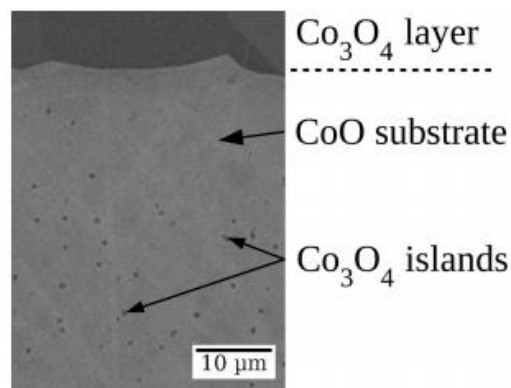


Figure 10. The cross-section of the CoO sample oxidized at 900 °C under oxygen pressure equal to 100 KPa for 12 h.

This study considers high temperature reactions of pure metals with an oxidant frequently result in the formation of one or more compounds in the product layer (scale). The scale is formed by flat compact layers of reaction products, growing parallel to the surface of the metallic core. The presence of the products depends on the reaction temperature and the partial pressure of the reactant in the gas atmosphere. They show that the Co_3O_4 oxide is growing not only as a continuous layer on the surface of CoO but it can be detected within the substrate of CoO in the form of isolated islands. The formation kinetics of Co_3O_4 island are independent of the oxidation time. The Co_3O_4 islands formation is the result of the decomposition of the CoO substrate. These experiments are conducted at high temperature and at variable O_2 pressure (700 ÷ 900 °C; 1 ÷ 100 KPa). In this case, the Co is completely oxidized in atmosphere to form CoO at 1000 °C with a lower O_2 partial pressure, then the Co_3O_4 is oxidized in the air with 50% O_2 concentration (higher partial pressure) for 12 h at 900 °C (36).

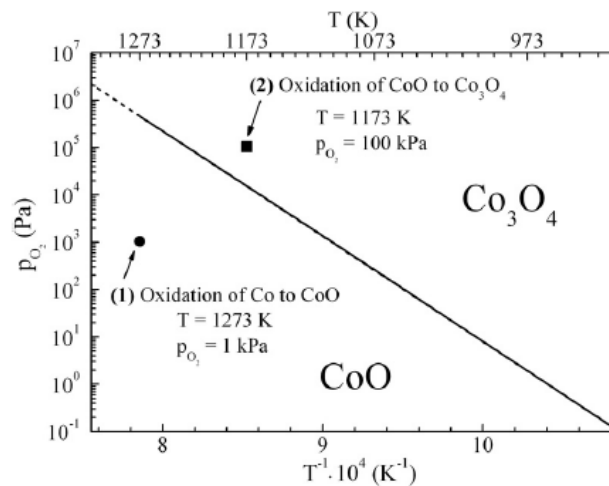


Figure 11. The part of the Co-O diagram with thermodynamic parameters for which metallic cobalt was oxidized to CoO (1) and Co_3O_4 (2).

Since there are only two stable cobalt oxides (CoO and Co_3O_4) at high temperatures, these results denote that the observed non-continuous phase within CoO constitutes Co_3O_4 cobalt oxide. This conclusion was confirmed by the results obtained using Raman spectroscopy, presented in figure 10. The continuous top layer as well as small islands (light) within the CoO phase is a pure, crystalline Co_3O_4 .

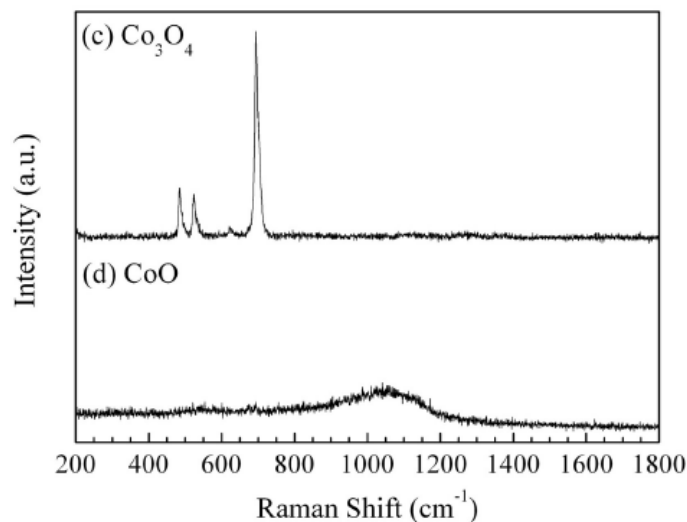
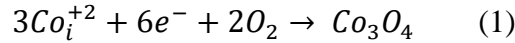


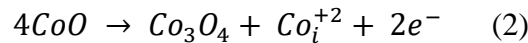
Figure 12. The results of Raman analysis of a part of the CoO sample oxidized at $900\text{ }^\circ\text{C}$ under the O_2 pressure equal to 100 KPa for 72 h.

The mechanism of the Co_3O_4 continuous layer formation is concerned. The islands are in the interior of the Co_3O_4 layer, dividing this layer into two parts, the outer one being three

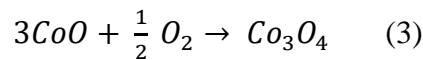
times thinner than the inner layer. Such a location of used markers in the interior of the reaction product of CoO oxidation explicitly indicates that the outer layer of Co₃O₄ grows on the outer Co₃O₄-O₂ interface due to the outward diffusion, according to the following reaction (the Kröger-Vink notation of defects):



while, the inner layer is developed at the CoO-Co₃O₄ interface because of the following displacement reaction:



where Co_i⁺² and e⁻ denote the double ionized interstitial cobalt cation in the Co₃O₄ crystal lattice and quasi-free electron, respectively. The Co₃O₄ oxide is predominantly disordered. On the other hand, the mechanism of the formation of Co₃O₄ isolated islands within the CoO phase is not clear. Theoretically, Co₃O₄ islands can be formed by oxidation of preferred sites of the CoO phase due to inward diffusion of oxygen, in accordance with the following chemical reaction:



or by decomposition of CoO at preferred sites, according to the displacement reaction presented in equation (2). Hence, the formation of Co₃O₄ islands due to oxidation of preferred sites of the CoO phase because of inward oxygen diffusion is improbable and so the decomposition of CoO takes place according to equation (2) and this mechanism is responsible for the formation of Co₃O₄ inside CoO grains. Since the amount of Co₃O₄ per unit surface area is independent of the reaction rate time and the average size is constant for the long reaction time, the formation of Co₃O₄ grains inside the CoO oxide has almost no influence on the CoO oxidation kinetics.

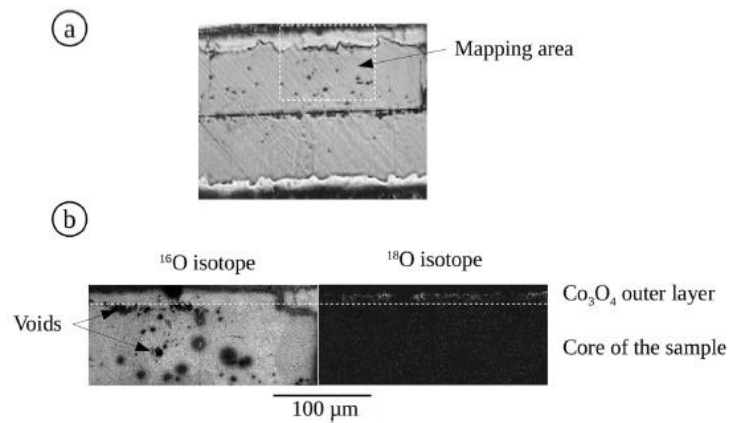


Figure 13. Distribution of the oxygen isotopes in the CoO sample after 12 h of oxidation at 900 °C. SIMS maps of the oxygen isotopes. (37)

Rojas et al. investigate the oxides state of cobalt in passivated samples by pure oxygen and air exposure to achieve an exhaustive chemical and structural characterization of the nanocomposite material in its original state (passivated Co powder) and after thermal treatments in vacuum.

After passivation, the fcc-Co nanocrystals of sizes $2 \div 20$ nm are detected. They are covered by an amorphous oxide passivation layer with a short range structural order similar to the cubic (fcc) CoO phase (38). Upon heating, crystallisation of the oxide layer is observed together with the formation of the Co_3O_4 spinel phase. The Co powder is heated up to 1500 °C in a He atmosphere of 1 Torr and the samples are passivated by oxygen (3 Torr for 10 min) before exposure to air. In these spherical grains of $9 \div 30$ nm there are interactions between the oxide layer and the ferromagnetic core. The XRD analysis indicates the presence of metallic cobalt in the fcc phase, as shown in Figure 14. It is interesting to mention that the starting Co powder material was hexagonal cobalt and high-pressure polymorphic phases can be stabilized in grains of a few nanometres in diameter. The cobalt oxide passivation layer should be quite amorphous or very thin and consequently no clear peaks from CoO or Co_3O_4 phases could be identified.

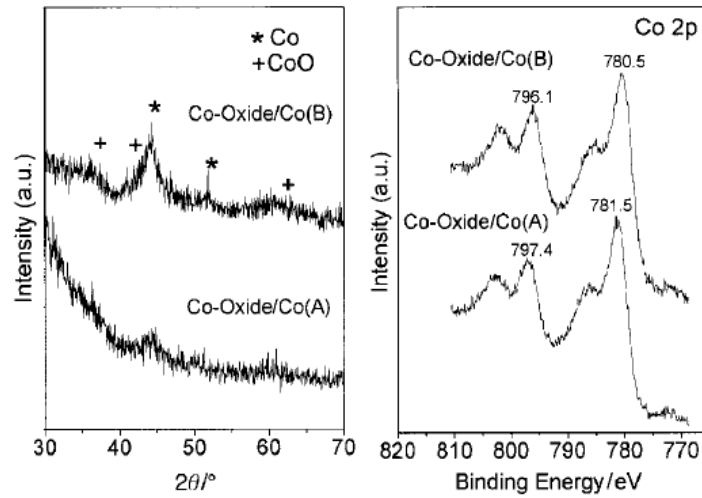


Figure 14. XRD diffraction patterns (left) and Co 2p photoelectron spectra (right) for the Co-oxide/Co(A) and (B) samples.

The XPS analysis evidence the absence of metallic cobalt: the passivation oxide layer is thicker than ca. 3 nm. This technique gives important information related to the major presence of Co^{2+} species, indicating the formation of a CoO like oxide layer after room temperature passivation of the nanocrystalline Co particles. In the following figure is shown the change from the pure metallic cobalt to the pure oxide phase.

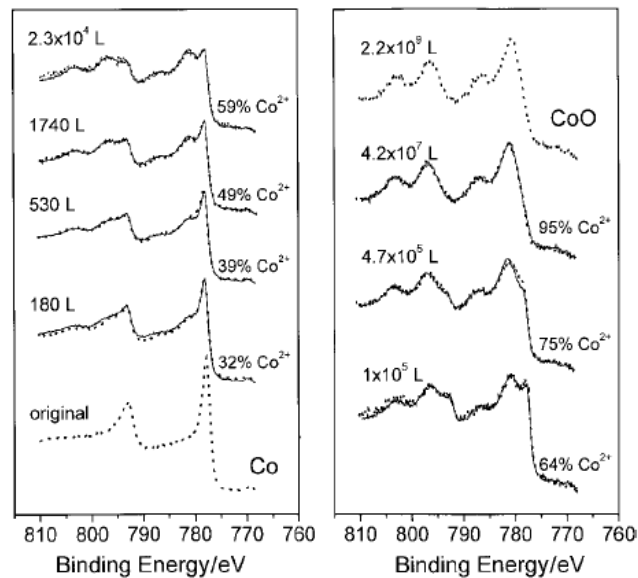


Figure 15. Co 2p photoelectron spectra of the in situ prepared nanocrystalline cobalt (original) and after exposure to different doses of oxygen. The experimental spectra are depicted as dotted line. Full lines correspond to the best fitted linear combination of the spectra for pure Co and CoO phases.

However, an appreciable oxidation of the nanoparticles occurs just by oxygen exposure of the sample to 30 Langmuirs of oxygen (10^{-6} Torr during 1 s).

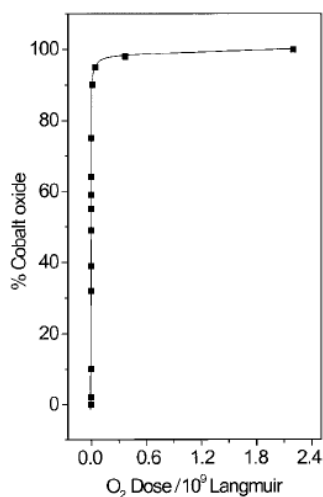


Figure 16. Percentage of oxidised cobalt in the total Co 2p photoelectron peak as a function of the oxygen dose during the in situ oxidation of the nanocrystalline cobalt.

To quantify oxide to metal ratio, linear combinations of the reference spectra for Co^0 and CoO have been carried out to achieve the best reproduction of the experimental spectrum for both samples. These linear combinations for samples Co-oxide/Co(A) and Co-oxide/Co(B) are shown in Figure 17 giving a quantification of the bulk composition of the oxide–metal nanocomposite materials.

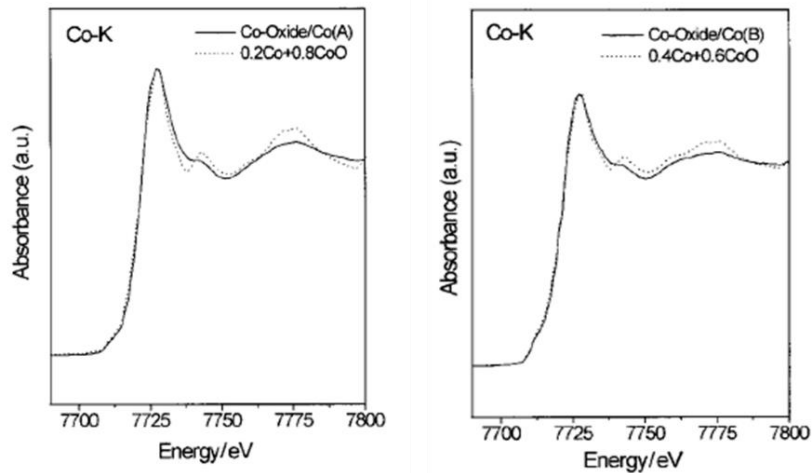


Figure 17. Right: the spectrum for the nanocrystalline composite sample (full line) is compared with the linear combination (dashed line) of the spectra for Co and CoO. Left: the spectrum for the nanocrystalline composite sample (full line) is compared with the linear combination (dashed line) of the spectra for Co and CoO.

It's also detected the evolution of the O K-edge of the Co-oxide/Co(A) sample from its original state under heating. The thermal evolution of the samples can also be followed by electron diffraction: it is possible to identify peaks corresponding to metallic fcc Co, cubic CoO and Co₃O₄ spinel phases. The original samples contain metallic Co and a CoO like overlayer. Figure 18 and 19 present a good agreement about the oxide passivation layer that evolves to a Co₃O₄ crystalline phase.

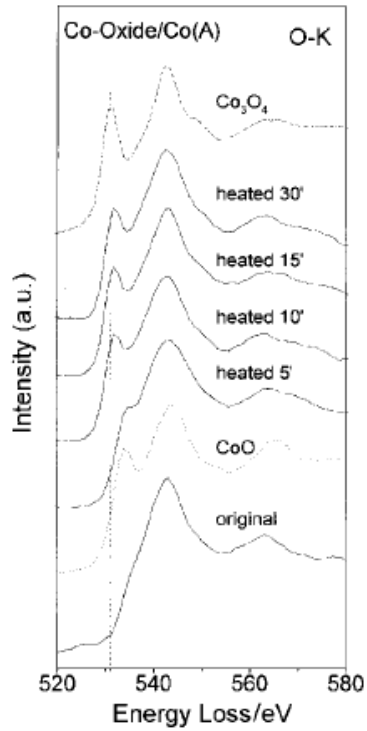


Figure 18. Evolution of the O K edge, as recorded by EELS, for the Co-oxide/Co(A) sample from its original state under electron beam illumination. For comparison spectra for CoO and Co_3O_4 reference samples are included.

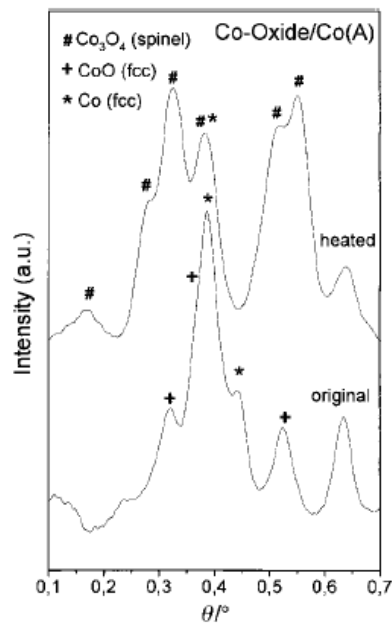


Figure 19. Integrated electron diffraction pattern for the original Co-oxide/Co(A) sample and after heating in vacuum under electron beam illumination. Expected theta angles for the rings corresponding to Co (fcc), CoO (fcc) and Co_3O_4 spinel phases are included.

By an industrial application of the FTS process, Van Steen et al. study the oxidation and re-reduction of cobalt in water/hydrogen mixtures. Since the stability of nanosized materials differs significantly from the stability of bulk materials, a thermodynamic analysis on the simultaneous oxidation and re-reduction of small metallic cobalt crystallites in the presence of water and hydrogen as a function of the crystallite diameter is performed as a catalyst deactivation in the Fischer-Tropsch synthesis (39).

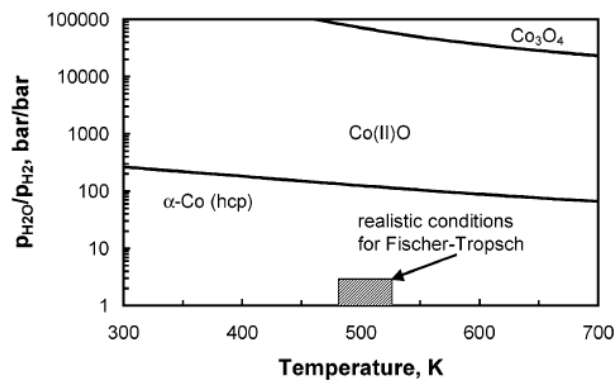


Figure 20. Stability diagram of bulk cobalt metal and various cobalt oxide phases as a function of temperature and ratio of partial pressure of water and of hydrogen. (40)

The oxidation of small cobalt crystallites or the formation of an oxide shell might be thermodynamically feasible under conditions that do not allow the oxidation of bulk metallic cobalt. Small metal cobalt crystallites exposed to a water/hydrogen atmosphere as experienced during the Fischer-Tropsch synthesis can be oxidized to CoO depending on the crystallite size, morphology, the starting crystal phase, and the ratio of the partial pressure of water relative to the partial pressure of hydrogen. The spherical cobalt crystallites with a diameter less than 4.4 nm will not be stable under industrially relevant Fischer-Tropsch conditions ($p_{\text{H}_2\text{O}}/p_{\text{H}_2} < 1.5$), as seen in the previous figure. It must, however, be kept in mind that cobalt crystallites in intimate contact with support material will yield the thermodynamically more stable cobalt-support species. Thus, the stability region for metallic cobalt crystallites given here might be a lower estimate for the actual stability region.

By considering the thermodynamics in the FTS synthesis, Van De Loosdrecht et al. summarize that oxidation is not a deactivation mechanism during realistic Fischer-Tropsch synthesis and the oxidation isn't connected to the sintering. The partial pressure of water

and of hydrogen haven't any effect on the support. The experiments are conducted on an industrial Co/Al₂O₃ catalyst (cobalt crystallites of 6 nm) at the temperature between 200 and 250 °C, as shown in the table and in the figure. Hence, the oxidation of cobalt can be prevented by the correct combination of the reactor partial pressures of hydrogen and water ($P_{H_2O}=P_{H_2}$) and the cobalt crystallite size and appears to be independent of the support.

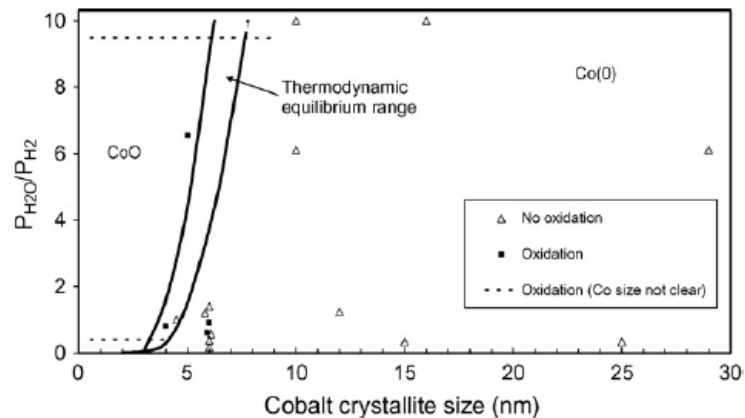


Figure 21. The open literature data on the effect of the water/hydrogen reactor ratio as a function of cobalt crystallite size on the oxidation behaviour of cobalt. All the data are superimposed on the thermodynamic equilibrium data range (solid lines) generated by Van Steen et al. (41) for nano-sized cobalt crystallites.

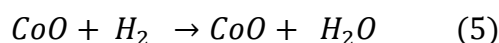
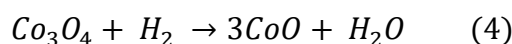
Table 2. The open literature current data on the effect of the water/hydrogen reactor ratio combined with the cobalt crystallite size on the occurrence of oxidation during FTS. ($P_{H_2O}=P_{H_2}$ data in 'italics' were re-calculated; cobalt sizes in 'italics' were estimated)

Author	Support	Cobalt size (nm)	Cobalt size measurement technique	P_{H_2O}/P_{H_2} in reactor	Oxidation (yes/no)	Oxidation analysis technique
Schanke et al. [18]	Alumina	25	H_2 TPD	0.33	No	XPS
		15		0.33	No	XPS
		<15		0.33	Yes	XPS
Hilmen et al. [21]	Alumina	16	H_2 chemisorption	10	No	XPS
		10		10	No	XPS
		<10		10	Yes	XPS
Iglesia [40]	Silica	4	–	0.74	Yes	–
Jacobs et al. [14]	Alumina	6	H_2 TPD	0.16	No	XANES
		<6		0.16	Yes	XANES
Jacobs et al. [8]	Alumina	6	H_2 TPD	0.56	No	XANES/EXAFS
		6		0.60	Yes	XANES/EXAFS
Jacobs et al. [15]	Alumina	6	H_2 TPD	0.38	No	XANES
		<6		0.38	Yes	XANES
Jacobs et al. [9]	Alumina	6	H_2 TPD	0.91	Yes	XANES/EXAFS
		12		1.24	No	XANES/EXAFS
Kiss et al. [10]	Silica	5 ^a	TEM	6.55	Yes	TEM
Bian et al. [34]	Silica	10	H_2 chemisorption	6.11	No	EXAFS/XRD
		29		6.11	No	EXAFS/XRD
Saib et al. [47]	Silica	4.5	AFM	1.0	No	NEXAFS
Saib et al. [51]	Alumina	6	TEM	1.0–1.5	No	XANES
This paper	Alumina	6	TEM	1.0–1.5	No	XANES/XRD/magnetic

^a Although reported as oxidation of 5–6 nm Co crystallites from TEM it is not clear whether only the small cobalt crystallites were oxidised to cobalt silicate.

2.3 Reduction

Cobalt oxide reduction from Co_3O_4 to Co^0 is commonly thought to follow a path consisting of two reactions accounting, from a stoichiometric point of view, for 25% and 75% of the oxygen depletion respectively. The reduction occurs in two steps:



Catalyst reducibility can be evaluated by characteristic temperatures of the two main TPR reduction steps. Even a small addition of Pt shifts the reduction temperatures towards lower values. Hence, platinum promotion leads to beneficial effects for both the reduction steps. However, as the transition $Co_3O_4 \rightarrow CoO$ occurs at low temperatures, usually lower than the typical catalyst activation temperatures (350 ÷ 400 °C), also unpromoted sample can easily get over this step. Thus, the major improvement with Pt promotion lays in the second step, i.e. the transition $CoO \rightarrow Co^0$, which is thought to be cluster-size dependent (42) and severely hindered by interaction with the alumina support. The addition of Pt appears to decrease the energy barrier related to the second step, thus showing significantly

lower reduction temperatures: this catalysing effect was mainly attributed to H₂ dissociation and its subsequent spillover that occurs more readily on the noble metal surface than on the cobalt oxides surface.

Typically, cobalt oxide in the form of the spinel is found in calcined catalyst immediately before activation in a reducing gas stream in preparation for FTS. In this step Co₃O₄ is reduced to CoO and then into metallic Co. It proceeds by this two-step reaction where the Co⁺² and Co⁺³ are transformed into Co⁺² and then in metallic cobalt, Co⁰. In the following figure, the Co oxidation state is monitored as a function of the reduction time: increasing the reduction time, the reduction from Co₃O₄ to CoO and then to Co⁰ occurs under a flow of pure H₂ and heating from the room temperature up to 400 °C with a heating ramp of 5 °C/min (43).

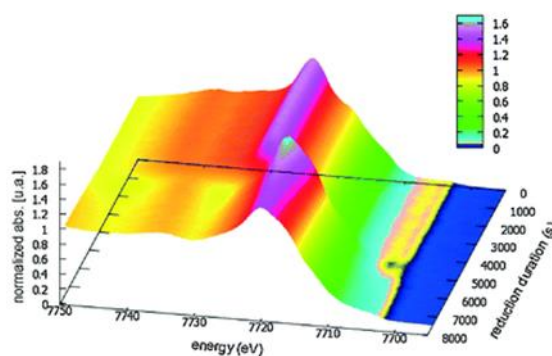


Figure 22. Time resolved XANES spectra corresponding to the reduction of Co/Al₂O₃ catalyst (7 wt%).

A direct relationship between the Fischer–Tropsch synthesis (FTS) rate and the number of surface cobalt atoms available for reaction is usually obtained (44). For Co/Al₂O₃ catalysts in particular, the site density depends on two primary factors:

- the average size of the cobalt clusters on the support
- the fraction of cobalt reduced to the metallic state.

Jacobs et al. investigates on the addition of small amounts of noble metal promoters, such as Pt and Ru to cobalt-based catalyst supported on alumina. They found that noble metals favour the reduction of cobalt oxide shifting the temperature at which the two steps (Co₃O₄ → CoO and CoO → Co⁰) occur to lower temperatures (44). However, Re affects only the second step. Re is reduced at a higher temperature than Pt or Ru, and at approximately the

same temperature as the first step of cobalt reduction ($\text{Co}_3\text{O}_4 \rightarrow \text{CoO}$). Thus, Re metal is able to catalyse only the second step.

The temperature-programmed reduction (TPR) suggests that hydrogen spillover from the promoter to cobalt oxide clusters is important for the catalysis of cobalt oxide reduction.

In situ EXAFS shows that the average cobalt cluster size decreases with increasing the promoter loading. In this case, Re promotes reduction of smaller species which interact with the support, and therefore, for a given reduction temperature, the average cobalt metal cluster size decreases as a function of increasing Re content.

After reduction at a temperature slightly above the first peak in the TPR ($\text{Co}_3\text{O}_4 \rightarrow \text{CoO}$), the species remaining on the surface displayed XANES spectra identical to that of CoO. After reduction at a temperature above the second broad TPR peak, XPS showed that a residual oxide species was present, with a binding energy equivalent to cobalt aluminate.

Paterson et al. investigates the cobalt reduction and carbide formation (45). In the Figure 23, the result reduction of Co_3O_4 with a slow temperature ramp with a flow of pure H_2 (100%) at atmospheric pressure is shown. The Co_3O_4 starts to reduce at 170 °C and the CoO at 180 ÷ 210 °C. Then, the CoO intensity starts to reduce and the Co^0 becomes visible. Only the metallic Co is visible at 300°C for only 4h.

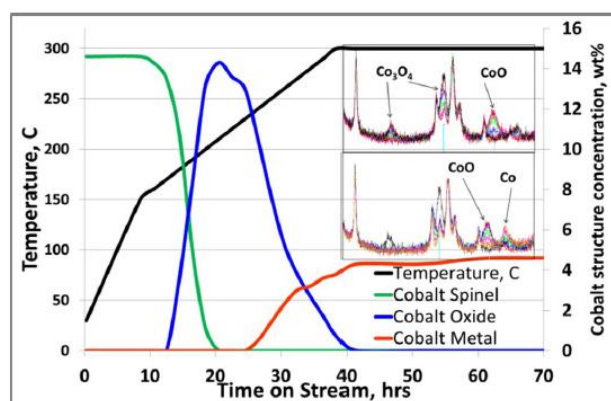


Figure 23. Reduction of cobalt oxide spinel with H_2 .

2.4 Passivation

The reduced Co metal form is the active site for the FT reaction. Accordingly, the reduction of the catalyst prior to the reaction is required. It's often useful to reduce the

catalyst *ex situ*. However, cobalt metal centers reoxidized after air exposure. The catalyst passivation treatment after the catalyst reduction is required to protect the catalyst surface from rapid oxidation. Usually, the passivation is achieved by the formation of a thin layer of Co oxide on the catalytic surface. The most common approach to passivate air sensitive metals is controlled exposure to low concentration of O₂ (0.1 ÷ 1%) in an inert as He or N₂, as applied in several studies (47) (48). The result of this treatment is a surface passivation, where the thin oxide layer protects the metallic core from further oxidation in air. Besides O₂, CO₂ and N₂O are also used but these methods don't lead to satisfying results (46) (49).

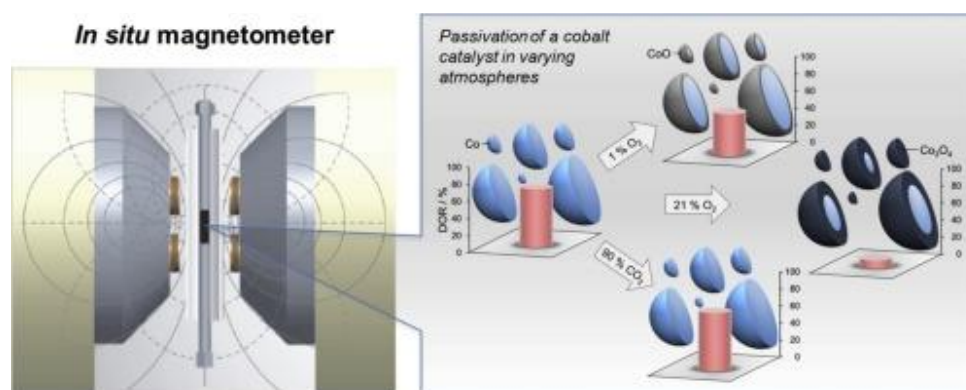


Figure 24. On the left the *in situ* magnetometer and on the right the summary of the effectiveness of catalyst passivation techniques at different conditions.

Wolf et al. studied the passivation treatment on a reduced Pt promoted Co/SiO₂ FT catalyst with the *in situ* magnetometer (46). This instrument monitors directly the formation or loss of magnetic species: metallic cobalt to CoO or Co₃O₄ are used to illustrate the passivation of the catalyst by low concentrations of O₂ in N₂, CO₂ or He. The authors studied the magnetic measurements on 500 mg of the oxidic parent catalyst in reactor, reduced for 10 h at 400 °C in H₂ at a heating rate of 2 °C/min. Three different passivation treatments are applied to the reduced catalyst:

- 1% O₂/N₂ at 30 °C
- 90% CO₂/Ar at 30 °C
- 90% CO₂/Ar at 150 °C.

The measured magnetisation is directly proportional to the amount of metallic Co, only one metallic compound at these operating conditions. It's possible to calculate the DOR (degree of reduction) by calibrating the instrument with well-defined amounts of metallic

Co. The mass fraction of ferromagnetic material describes the relative mass of ferromagnetic Co domains larger than a critical diameter of $15 \div 20$ nm at room temperature. Below this critical value the metallic Co behaves superparamagnetic and above this it is ferromagnetic. An increase of the ferromagnetic material means an increased average Co crystallite size and/or a decrease overall fraction of smaller Co crystallites in the metallic phase. After the passivation, which guarantees a stable magnetisation, the samples are exposed to a controlled air stream at 30 °C and the same procedure is done for fresh reduced samples without passivation. At the end, a re-reduction is conducted at 400 °C in H_2 for 30 min with a heating rate of 2 °C/min. All experiments are conducted with a GHSV of 200 ml/g/min based on the initial mass of parent catalyst and the outlet gases of the reactor are analysed via gas chromatography with TCD.

The crystallites are arranged in clusters of 40 - 100 nm and the volume based average Co oxide crystallite size of the prepared catalyst are about 16.5 nm (via TEM) and 14.6 nm (via XRD) while the dominating metallic phase is fcc allotrope with crystallite size of 11.8 nm. It's also present a small fraction of hcp Co.

The phase change from non-magnetic Co oxide to magnetic metallic one during the reduction of the parent catalyst, at 210 °C, is detected by increasing the amount of metallic Co formed with final DOR value at 400 °C of 89% . The magnetisation decreases with the increase of temperature and a constant value is reached after 30 h, a time longer than passivation one. During the passivation process the temperature is constant, which complies with the definition of proper passivation ($\Delta T < 2 \div 3$ K) and excludes any hotspots even in the exposure in air as in the following figure.

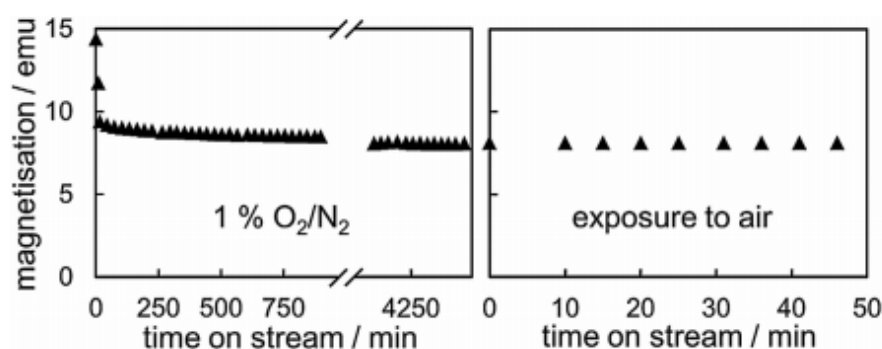


Figure 25. Saturation magnetisation as function of time on stream during passivation of the reduced catalyst in 1% O_2/N_2 at 30 °C (left) and subsequent exposure to air (right)

Wolf et al. assumed that the amount of metallic cobalt present is adequately passivated by the formation of cobalt oxide on the surface of the cobalt crystallites. For low concentration of O_2 the analysis with XRD on the passivated catalyst reveals the presence of CoO , while Co_3O_4 is not present (Figure 26). It's observed that the CoO amount increases with the exposure in air after long time for 6 months at $20\text{ }^\circ\text{C}$, while the metallic peaks are less pronounced. Hence, the only suitable passivation for a prompt characterisation as the catalyst shows no long-term stability in air is in $1\% O_2/N_2$.

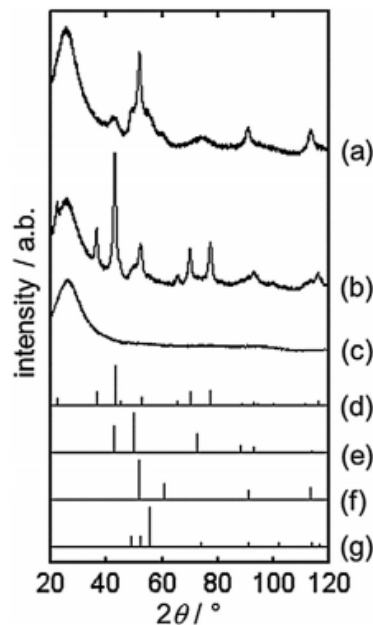


Figure 26. XRD pattern of passivated catalyst in $1\% O_2$ (a), the air treated catalyst of the reference experiment (b), pure silica (c), and the reference pattern of Co_3O_4 (d), CoO (e), fcc-Co (f), and hcp-Co (g).

In Figure 28, an increase of the mass fraction of ferromagnetic Co (fcc) from 41 to 50% is shown and this corresponds to almost full oxidation of smaller crystallites. As for studies of Dalman and Barbier, there is a mass loss in Co crystallites below the critical diameter of $15 \div 20\text{ nm}$: almost a full oxidation of the smaller cluster occurs.

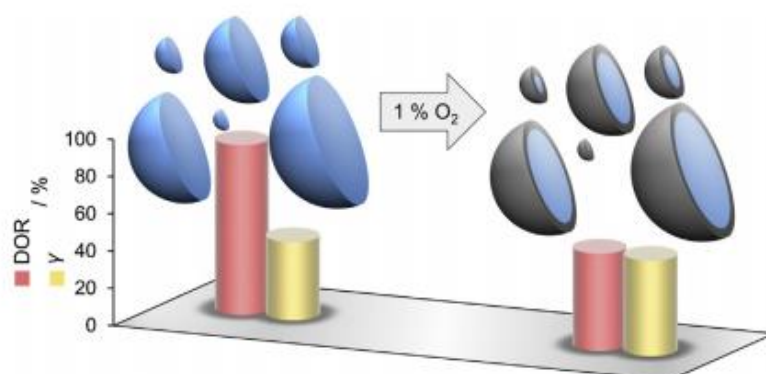


Figure 27. Schematic of Co particles (light blue) of different size as half spheres illustrating the formation of a uniform CoO layer (grey) by passivation in 1% O₂ at 30°C and a histogram of the consequential change in the fraction of ferromagnetic cobalt (γ) and DOR.

For a diffusion limited oxidation process, the layer thickness of oxide is constant: smaller crystallites oxidise to a higher extent as the mass fraction of oxide per particle increases with decreasing diameter. Initially ferromagnetic cobalt crystallites turning superparamagnetic during passivation due to a reduction of the metallic (core) diameter to just below the critical diameter has a reverse effect on but is less pronounced. The catalyst in the passivated state still has a high DOR of 51%. Theoretical estimations assuming uniformly sized cobalt spheres result in a diameter of 9.8 nm for the metallic core and a CoO layer thickness of 1.3 nm, which is below reported values of 3 nm for similar passivation treatments, Due to lower O₂ concentrations (maximum 0.1% or unknown) and possibly shorter duration of the passivation processes (overnight or unknown), further oxidation of the metallic cobalt core to CoO in air before characterisation cannot be excluded in these studies. Regarding the passivation of spent Co-based Fischer-Tropsch catalysts, it has been reported that small Co crystallites can undergo oxidation during the Fischer-Tropsch synthesis due to the oxidative pressure of the gaseous product water. The DOR in the reference experiment, i.e. the direct exposure of a reduced catalyst to air, drops to 12%. Although the oxidation was not controlled ($\Delta T=22$ °C), a metallic core was successfully passivated as well. The formation of Co₃O₄ was identified by XRD (figure 24) and no changes were observed after 6 months exposure to air during storage. These results and a theoretical layer thickness of 3.4 nm in the reference experiment confirm the reported dependency of the formed oxide type in the layer on the O₂ concentration during the passivation process (50), which is also reported for iron nanoparticles [54].

Furthermore, it highlights the importance of a controlled oxidation as the reference experiment can be seen as a treatment with 21% O₂ /N₂ (Figure 28).



Figure 28. A schematic representation of a cobalt particle (light blue), as half sphere of average diameter illustrating the dependence of the formed oxide type (CoO: grey, Co₃O₄: dark blue) and the oxide layer thickness on the concentration of O₂ during the passivation.

The formation of Co₃O₄ is also reported by Nakhaei Pour et al. for passivation of a carbon nanotube supported Co catalyst in 5.2% O₂ /He for 2 h. The nanoparticles in the catalyst passivated in 1% O₂ are completely re-reducible in H₂ and reach the initial DOR of 89% at low temperatures, while the DOR after re-reduction in the reference experiment only 83%. However, a higher re-reducibility in the reference experiment can be achieved as the magnetisation increases during the isothermal step of the re-reduction at 400 °C. The extrapolated onset of the re-reduction for the passivated sample is around 65 °C and significantly lower than for the reference experiment at 140 °C and the parent catalyst at 210 °C. The presence of the metallic cobalt core and/or of an activated platinum phase can be assumed to have a beneficial effect on the reduction. Platinum is present in its oxidic phase in the parent catalyst, but it should remain metallic during the different passivation treatments. Hydrogen activation on said metallic surfaces and subsequent hydrogen spillover to the cobalt oxide phase could therefore take place at significantly lower reduction temperatures enhancing said process. Differences between the onset temperatures of the reference experiment and the re-reduction of the passivated sample could originate from different intrinsic reduction temperatures of the oxides formed under the respective conditions (Co₃O₄ vs. CoO). Furthermore, the thinner, possibly amorphous or more porous CoO layer after controlled passivation in 1% O₂ /N₂ facilitates diffusion of hydrogen to the metallic core further aiding reduction. Because of these effects the particles passivated in 1% O₂ are easier to reduce, as shown in Figure 29.

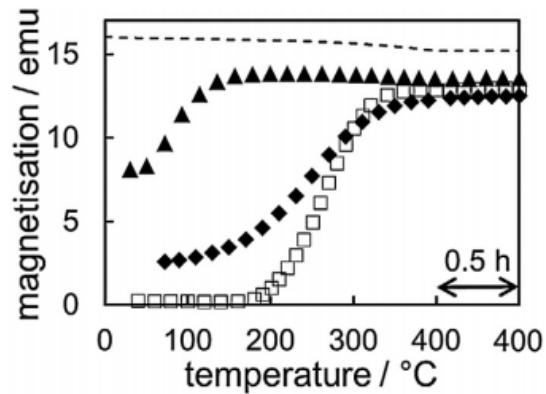


Figure 29. Saturation magnetisation as function of temperature during re-reduction of the passivated catalyst at 1% O_2/N_2 at 30 °C in triangular shape line, the reference experiment without pre-treatment in rhombic shape line, the reduction of the parent catalyst as reference square shape line and the temperature dependent magnetisation corresponding to DOR=100% in dashed line.

This agrees with a previously reported complete re-reducibility of carefully passivated crystallites. During the treatment of the reduced catalyst with 90% CO_2/Ar at 30 °C, no cobalt oxide is formed as seen by the constant saturation magnetisation, as shown in Figure 30.

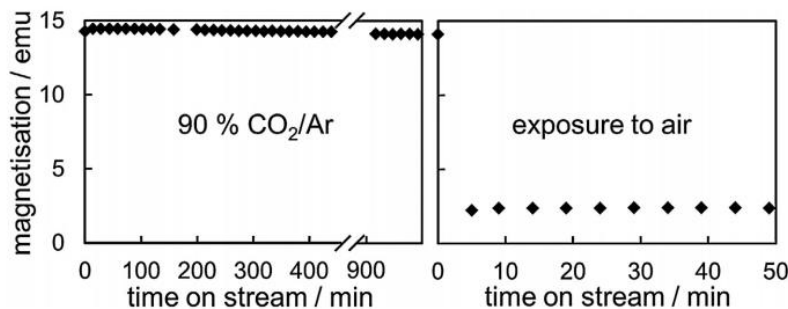


Figure 30. Saturation magnetisation as function of time on stream during treatment of the reduced catalyst with 90% CO_2/Ar at 30 °C on the left, and the exposure to air on the right.

A slight initial increase and subsequent decrease of the saturation magnetisation may be explainable by the adsorption of CO_2 on the surface of the cobalt crystallites, which can affect the magnetic moments of surface atoms in ferromagnetic and superparamagnetic materials. Dissociation of CO_2 is unlikely as only CO_2 and Ar were detected in the reactor outlet gases during the treatment with CO_2 . Furthermore, adsorbed CO would most likely decrease the saturation magnetisation of cobalt significantly as calculated by Claeys et alia. The cobalt particles oxidise to a high extent upon exposure to air before the first magnetic reading was taken after 5 min on stream, as shown in the figure 20 on the right. The

temperature increased from 35 °C to 88 °C indicating a violent oxidation. Increasing the temperature for the 90% CO₂/Ar treatment from 30 °C to 150 °C did not result in an air stable cobalt phase either. In fact, no mentionable differences between the CO₂ treatments and the reference experiment were observed. It can be concluded that CO₂ treatment at 30 °C or 150 °C does not protect the metallic particles from air and therefore is not an appropriate passivation method for this catalytic system. Therefore, reported passivation with CO₂ of cobalt based catalysts in the literature should be critically reviewed. However, it has to be noted that different types of supports and promoters dictate the behaviour of catalysts and could influence the here described findings. Furthermore, most reported studies using gaseous CO₂ as passivation medium are focusing on spent catalysts, i.e. after exposure to, for example, Fischer-Tropsch conditions. The reactants can change the surface structure of metal catalysts, as well known. The presence of adsorbed products, such as hydrocarbons, could further hinder oxidation upon exposure to air, explaining the discrepancy of previous reports on the applicability of CO₂ as passivation agent and the present study.

For the passivation of a cobalt Fischer-Tropsch catalyst with diluted O₂ and pure CO₂, the freshly reduced catalyst did not oxidise during CO₂ treatment at 30 °C, nor at 150 °C and undergoes rapid oxidation upon exposure to air. No mentionable differences to a non-CO₂ treated catalyst were observed. During treatment in 1% O₂/N₂, smaller cobalt crystallites oxidised almost completely and the DOR dropped by 48%, which corresponds to a theoretical 1.3 nm layer of CoO protecting the metallic core from further oxidation in air. Though passivation is achieved, this treatment is not suitable for long-term protection as the catalyst experiences an ongoing slow oxidation. The re-reduction of the carefully and properly passivated catalyst was much more facile than that of the parent sample, which is believed to be due to a combination of beneficial effects: the oxide in the passivated sample consists of a gently formed, highly reducible CoO layer and a metallic core, and metallic platinum is present allowing for hydrogen spillover to take place at lower temperatures.

As real application of the catalyst passivation, several patents exist and show the use of the passivation method in industrial processes. In the FT industrial processes, the catalyst is reduced and passivated *ex situ*, thereafter it is loaded into the reactor, in which its activity and selectivity are exploited.

A patent from IFP about the preparation of a Co-based catalyst affirms that after a reduction step with 1 ÷ 3 litres/minutes of H₂ at temperature between 350 ÷ 450 °C with a heating rate between 3 ÷ 20 °C/min for 10-20 hours, a passivation step is conducted on the sample (51; 52), carried out in presence of 1 ÷ 2% O₂ diluted with an inert gas, as nitrogen, at temperature between 10 ÷ 80 °C for 1 ÷ 5 h.

The patent of Eurecat S.A. reported the passivation process by heat treatment under a gas flow containing O₂, in the presence or in absence of water vapour, thus imparting to Co-based catalyst a behaviour that is not self-heating (53). Two O₂ partial pressure (2 KPa and 7 KPa) are used at different temperatures of 20, 50, 100, 120 °C. The temperature/oxygen partial pressure can be adjusted to control the oxidation: the temperature less than 120 °C is advantageous. It's found that the presence or absence of water doesn't affect the process. For a process of ex-situ oxidizing passivation process of pre-sulfurized catalyst for hydro-conversion of hydrocarbons at temperature between 75 ÷ 120 °C and subjected to treatment of passivation with a molecular O₂ gas flow at partial pressure of at least 7 KPa, the passivation is sufficient to yield a catalyst having a critical self-heating temperature of at least 100 °C.

The Chevron U.S.A. Inc. (Kibby et al.) works on the preparation of Co-based catalyst on the acidic support, as zeolite (54). In this patent the reduction, the passivation and the re-oxidation and/or a second reduction of the catalytic material are investigated. In particular, the passivation after the second reduction is useful if the catalyst is activated in a reactor different and separated by the FTS ones. Since the cobalt is well-dispersed on the surface and extremely pyrophoric material, the passivation occurs in a nitrogen-diluted air over the catalyst with 1% of O₂, after the previous steps and the cooling at the room temperature. For the reduction and passivation procedures, the calcinated catalyst are heated at 1 °C/min to 400 °C in the H₂ with GHSV per catalyst 1500 h⁻¹ and it remains at this temperature for 15 h. The cooling is controlled with a 0.4 °C/min to 50 °C, now the H₂ can be replaced by N₂ with GHSV per catalyst about 500 h⁻¹. After 3 hours in nitrogen the catalyst achieves the temperature of 40 °C. Then for the passivation step, N₂ is replaced with air for 10 hours or in the case of diluted air (2% O₂) at higher temperature of ca. 100 °C. It is possible to introduce the re-oxidation step in air (GHSV per catalyst about 1000 h⁻¹) with a heating ramp of 1 °C/min up to 300 °C, once the catalyst achieves the temperature it remains in this condition for 7 hours.

The temperature of 300 °C is the maximum temperature that can achieve to avoid some reactions in the solid state between the Co oxides and the support.

There is the possibility to have a second reduction and passivation. The reduction proceeds with the same conditions of the first reduction step, but the maximum temperature is shifted at 350 °C, since in this case where the cobalt is mixed with ruthenium and reacts less with the alumina support: the catalyst is much easier to reduced. The heating ramp of the final reduction is 1 °C/min for the achievement of 350 °C for 10 h. It's sufficient a temperature of 250 °C and a 5 ÷ 10 % H₂ concentration diluted in N₂ could be used.

Bibliografy

1. A. M. Saib, D. J. Moodley, I. M. Ciobîcă, M. M. Hauman, B. H. Sigwebela, C. J. Weststrate, J. W. Niemantsverdriet, J. van de Loosdrecht. 2010, *Catal. Tod.*, Vol. 154, pp. 271–282.
2. J. W. A. De Swart, R. Krishna, S. T. Sie. 1997, *Stud. Surf. Sci. Catal.*, Vol. 107, pp. 213-218.
3. M. Dry, in: G. Ertl, H. Knozinger, F. Schuth, J. Weitkamp (Eds.), *Handbook of Heterogeneous catalysis*, Wiley-VCH, Weinheim. *Handbook of Heterogeneous catalysis*. Weinheim : Wiley-VCH, 2008, pp. 2965-2994.
4. J. van de Loosdrecht, F.G. Botes, I.M. Ciobica, A. Ferreira, P. Gibson, D.J. Moodley, A.M. Saib, J.L. Visagie. 2013, *From Elements to Applications*, Vol. 7, pp. 525–557.
5. A.Y. Khodakov, W. Chu, P. Fongarland. 1692, 2007, Vol. 107.
6. R. Oukaci, A. H. Singleton, J. G. Goodwin Jr. 1999, *Appl. Catal. A Gen.*, Vol. 186, pp. 129-144.
7. R. L. Espinoza, J. L. Visagie, P. J. Van Berge, F. H. Bolder. US5733839A
8. E. J. Creighton, C. M. A. M. Mesters, M. J. Reynhout, G. L. M. M. Verbist. US 2008/0171655A1
9. A. Hoek, A. H. Joustra, J. K. Minderhoud, M. F. M. Post. EP 0104672 B1

10. S. A. Posthuma, H. M. H. Wechem, H. Heetveld. U.S 5486542
11. R. J. Dogterom, R. M. van Hardeveld, M. J. Reynhout, B. A. van de Werff. US 7790648 B2
12. J. L. Visagie, H. M. Veltman. WO 2006075216 A1
13. P. J. van Berge, S. Barradas. US 7365040 B2
14. P. J. van Berge, J. van De Loosdrecht, S. Barradas. WO 2003012008 A2
15. P. J. van Berge, J. van De Loosdrecht, L. Jacobus. US 5053574
16. S. Barradas, E. A. Caricato, B. H. Sigwebela, J. P. van Berge, J. van De Loosdrecht. US 4568663
17. R. Oukaci, A. H. Singleton, J. G. Goodwin Jr. 1999, *Applied Catalysis A: General* 186, pp. 129-144.
18. T. Xiao, Y. Qian. WO 2008104793 A2
19. S. C. Leviness, F. Daly, L. A. Richard, S. Rugmini. US9359271 B2
20. J.J. Hebert, P. Senecal, D. J. Martin, W. Bras, S. K. Beaumont and A. M. Beale. 2016, *Catal. Sci. Techn.*, Vol. 6, pp. 5773-5791.
21. Major, V. Singh and D. T. 2016, *Inorg. Chem.*, Vol. 55, p. 3307–3315.
22. A. M. Saib, J. L. Gauché, C. J. Weststrate, P. Gibson and J. H. Boshoff. 2014, *Ind. Eng. Chem.*, Vol. 53, p. 1816–1824.
23. S. Sadasivan, R. M. Bellabarba and R. P. Tooze. 2013, *Nanoscale*, Vol. 5, pp. 11139–11146.
24. Mott, N. Cabrera and N. F. 1948, *Rep. Prog. Phys.*, Vol. 163, p. 12.
25. C. M. Wang, D. R. Baer, L. E. Thomas, J. E. Amonette. 2005, *J. Appl. Phys.*, Vol. 98.
26. A. M. Saib, J. D. Moodley, I. M. Ciobîca, M. M. Hauman, H. B. Sigwebela, C. J. Weststrate, J. W. Niemantsverdriet and J. van deLoosdrecht. 2010, *Catal. Tod.*, Vol. 154, pp. 271-282.
27. C.S. Yoo, P. Soderlind and H. Cynn. 1999, *J. Phys. Cond. Mat.*, Vol. 10, pp. 311–318.
28. D. H. Ha, L. M. Moreau, S. Honrao, R. G. Hennig, and R. D. Robinson. 2013, *J. Phys. Chem. C*, Vol. 117, p. 14303–14312.
29. A. Navrotsky, C. Ma, K. Lilova and N. Birkner. s.l. : *SCIENCE*, 2010, *Science*, Vol. 330, pp. 199-201.
30. A. Navrotsky, C. Ma, K. Lilova and N. Birkner. 2010, *Science*, Vol. 330, pp. 199-201.
31. Martin M., Koops U. and Lakshmi N. 2004, *Solid State Ion.*, Vol. 172, p. 357–363.

32. Jacobs, G., Ji Y., Davis B. H., Cronauer D., Kropf A. J. and Marshall C. L. 2007, *Appl. Catal. A*, Vol. 333, pp. 177-191.
33. S., Connor P. A. and Irvine J. T. 2002, *Electrochim. Acta*, Vol. 47, p. 2885–2892.
34. S. Junga, D. K. Nandia, S. Yeob, H. Kimb, Y. Jangc, J. Baec, T. E. Hongc and S. Kima. 2018, *Surf. Coat. Tech.*, Vol. 337, pp. 404–410.
35. M. Zyla, G. Smola, A. Knapik, J. Rysz and M. Sitarz. 2016, *Corros. Sci.*, Vol. 112, pp. 536-541.
36. O. Knacke, O.Kubaschewski and K. Hesselmann. *Thermochemical Properties of Inorganic Substances*, in: O. . Berlin, Dusseldorf : Stanhleisen, 1991.
37. C. J. Weststrate, M. M. Hauman, D. J. Moodley, A. M. Saib, E. van Steen and J. W. Niemantsverdriet. 2011, *Top. Catal.*, Vol. 54, pp. 811–816.
38. T. C. Rojas, J. C. Sanchez-Lopez, M. J. Sayagues, E. P. Reddy, A. Caballero and A. Fernandez. 1999, *J. Mat. Chem.*, Vol. 9, pp. 1011–1017.
39. E. van Steen, M. Claeys, M. E. Dry and J.van de Loosdrecht. 8, 2005, *Journal of Physical Chemistry B*, Vol. 109, pp. 3575–3577.
40. H., Lide D. R. and Kehiaian. *CRC Handbook of Thermophysical and Thermochemical Data*. Boca Raton : CRC Press, 1994.
41. E. van Steen, M. Claeys, M.E. Dry, J. van de Loosdrecht, E.L. Viljoen, J.L.Visagie. 109, 2005, *J. Phys. Chem. B*.
42. G. Jacobs, J. a. Chaney, P. M. Patterson, T. K. Das, J. C. Maillot, and B. H. Davis. 5, 2004, *J. Synchrotron Radiat.*, Vol. 11, pp. 414–422.
43. A. Rochet, V. Moizan, C. Pichon, F.Diehl, A. Berliet and V. Brios. 2011, *Catal. Tod.*, Vol. 171, pp. 186-191.
44. Jacobs G., Chaney J.A., Patterson P.M., Das T.K. and Davis B.H. 2, 2004, *Appl. Catal. A Gen.*, Vol. 264, pp. 203-212.
45. J. Paterson, M. Peacock, E. Ferguson, R. Purves and M. Ojeda. 2017, *Chem.Cat.Chem.*, Vol. 9, pp. 3463-3469.
46. M. Wolf, N. fischer and M. Claeys. 2016, *Catal. Tod.*, Vol. 275, pp. 135-140.
47. J. Haber, J. H. Block and B. Delmon. 1995, *Pure Appl. Chem.*, Vol. 67, pp. 1257–1306.
48. Pinna, F. 1998, *Catal. Tod.*, Vol. 41, pp. 129-137.

49. M. Claeys, E. van Steen, J.L. Visagie and J. van Loosdrecht. USpatent 8773118B2 2014.
50. D. Srikala, V.N. Singh, A. Banerjee, B.R. Mehta and S. Patnaik. 2008, *J. Phys. Chem. C*, Vol. 112, pp. 13882-13885.
51. R. Zannaro, A. Gusso and M.G. Clerici. 5856365 1999.
52. P. Chaumette, A. Gusso and R. Zannaro. EP0934115B1
53. P. Dufresne, F. Labruyere. US 7501376 B2 2009.
54. C.L. Kibby, A. Haas. US 2010/01068258 A1 2010.
55. O. Ducreux, B. Rebours, J. Lynch, M. Roy-Auberger and D. Bazin. 64, 2008, *Oil Gas Sci. Technol.*, pp. 49-62.
56. C.J. Werstate, M.M. Hauman, D.J. Moodley, A.M. saib, E. Van Steen and J.W. Niemantsverdriet. 54, 2011, *Top Catal.*, pp. 811-816.
57. G.R. Wilson, N.L. Carr. 5639798 1997.
58. H. A. Wright, A. P. Raje and R. L. Espinoza. US 6962947 B2 2005.
59. A. S. Lisitsyn, A. V. Golovin, V. L. Kuznetsov, and Y. I. Yermakov. 2, 1985, *J. Catal.*, Vol. 95, pp. 527–538.
60. Bartholomew, R. Reuel and C. H. 1984, *J. Catal.*, Vol. 85, pp. 78-88.
61. C.W. Tanga, C.B. Wang and S.H. Chienc. 473, 2008, *Thermochim. Acta*, pp. 68–73.
62. Chenavas J., Joubert J. C. and Marezio M. 1971, *Solid State Commun.*, Vol. 9, p. 1057–1060.
63. D. Kistamurthy, A.M. Saib, D.J. Moodley, J.W. Niemantsverdriet and C.J. Weststrate. 2015, *J. Catal.*, Vol. 328, pp. 123–129.
64. D. Nabaho, J. W. Niemantsverdriet, M. Claeys, and E. Van Steen. 2016, *Catal. Tod.*, Vol. 261, pp. 17-27.
65. G. Jacobs, T. K. Das, P. M. Patterson, J. Li, L. Sanchez, and B. H. Davis. 2, 2003, *Appl. Catal. A Gen.*, Vol. 247, pp. 335–343.
66. G. L. Bezemer, J. H. Bitter, H. P. C. E. Kuipers, H. Oosterbeek, J. E. Holewijn, X. Xu, F. Kapteijn, a J. Van Dillen, and K. P. De Jong. 12, 2006, *J. Am. Chem. Soc.*, Vol. 128, pp. 3956-3964.
67. Iglesia, E. 1997, *Appl. Catal. A Gen.*, Vol. 161, pp. 59-78.
68. J. C. Mohandas, M. K. Gnanamani, G. Jacobs, W. Ma, Y. Ji, S. Khalid and B. H. Davis. 2011, *ACS Catal.*, Vol. 1, pp. 1581–1588.

69. Khodakov, F. Diehl and A. Y. 1, 2009, Oil Gas Sci. TechN., Vol. 64, pp. 11–24.
70. S. Vada, A. Hoff, E. Adnanes, D. Schanke, and A. Holmen. 1-4, 1995, Top. Catal., Vol. 2, pp. 155-162.
71. T. P. Kobylinski, C. L. Kibby, R. B. Pannell, E. L. Eddy. 4729981 1988.

Chapter 3

Lab-Scale Rig and Experimental Procedures

3.1 Fixed bed lab-scale rig

The reduction and passivation experiment of the state of art Fischer-Tropsch catalysts have been performed in the LCCP (*Laboratory of Catalysis and Catalytic Processes*) laboratories on a rig operating at ambient pressure, shown in Figure 1 and Figure 2.

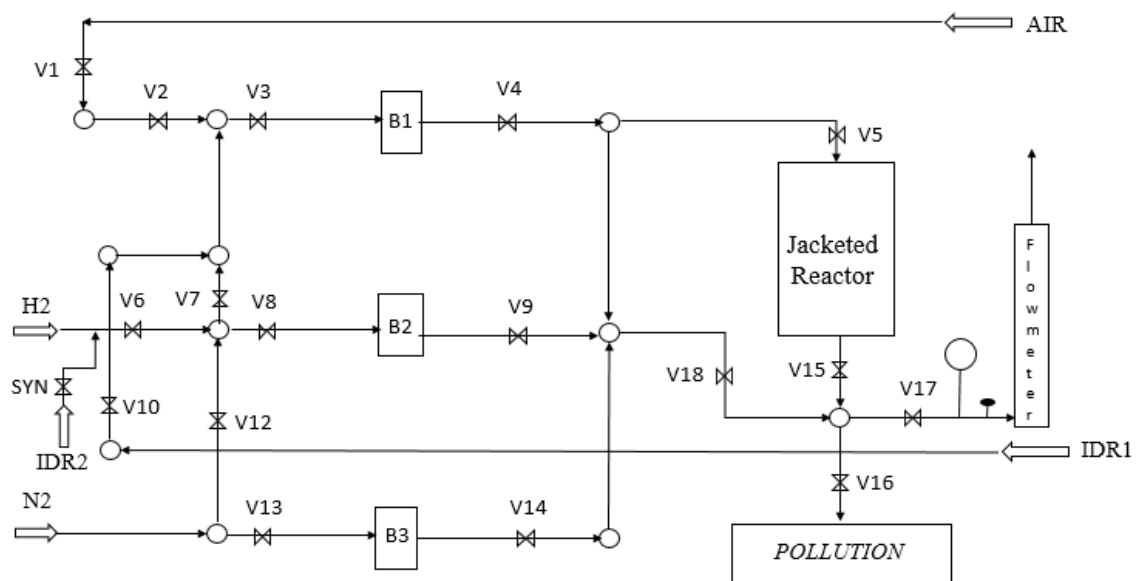


Figure 1. Simplified scheme of the lab-rig.



Figure 2. Real lab-rig.

It consists of three main zones:

1. *Feed zone*
2. *Reaction zone*
3. *Product analysis zone*

The temperature of the reactor is monitored by K type thermocouple is positioned at the centre of the catalytic bed.

The employed piping consists of ¼ inch diameter tubes, made of *INOX ASME 316* stainless steel.

3.1.1 Feed zone

The feed zone is the part of the rig related to regulation and distribution of the inlet gases.

The rig exploits globally five gas lines:

- AIR
- H₂
- IDR1
- IDR2

- Mix AC2

Only three of them can be used contemporarily during the tests, depending on the type of experiment carried out, hence different gas mixtures can flow in these lines. As shown in the Figure 1, the first line conveys the reactants as compressed air (AIR) or O₂/He (IDR1). The latter are used for the passivation tests. The second line in the middle conveys pure molecular hydrogen and is operated during catalyst reduction and is also used for the syngas feed (IDR2) during the catalytic test by switching the SYN valve as in Figure 2. The third line is connected to the line of pure nitrogen (*Mix AC2* line), which is the inert gas used during catalytic testing. Each one is characterized by a sequence of five elements, as shown in Figure 3:

1. on/off valve to intercept the gas
2. two Bourdon tube pressure gauges (P_{full-scale}= 6 barg): before and after the mass flow controller
3. mass flow controller.



Figure 3. Example of the main line and all its components.

Downstream of each line the gas can be sent to the connecting joint between the lines and they can flow in the reaction zone through the V5 or they can be sent to the vent by the bypass line through the V18. The third line N₂ can be vented in the atmosphere before the valve V13. The other gases and/or the bypass line are vented passing through the outlet line of the reactor in the fume hood, passing in a connected flowmeter. The outlet gases of

the reactor can be also sent to the product analysis zone (Pollution) via the quadruple connection with the opening of the valve V16 (Figure 2).

The flow control in the facility is performed by three mass flow controllers (*BROOKS® Smart II Mass Flow model 5850E*). *IDR1* and *AIR* line (line 2) controllers can regulate a flow rate from 0 up to 40 ml/min. *H₂* and *IDR2* (line 2) controller goes from 0 up to 200 ml/min. While *N₂* (line 3) controller regulates the flowrate from 0 up to 400 ml/min.

Each controller needs to undergo calibration before performing the experiments. The calibration is carried out by measuring the flow rates corresponding to different degrees of opening of the controller with a glass flowmeter. Performing a linear regression of the measured data, a characteristic line is obtained for each mass flow controller (Figure 4,5,6,7):

$$\text{Flow rate} = m \cdot (\text{degree of opening}) + q \quad (40)$$

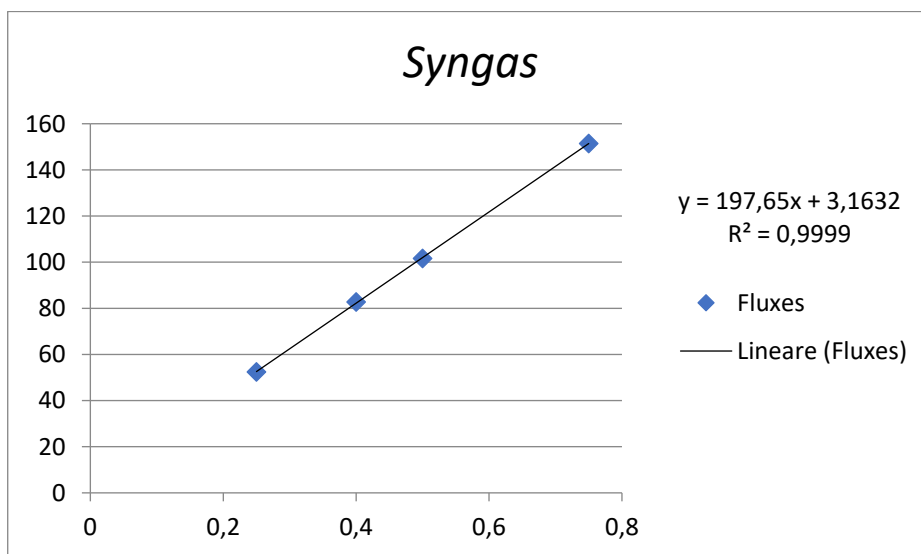


Figure 4. Calibration line of syngas with H₂.

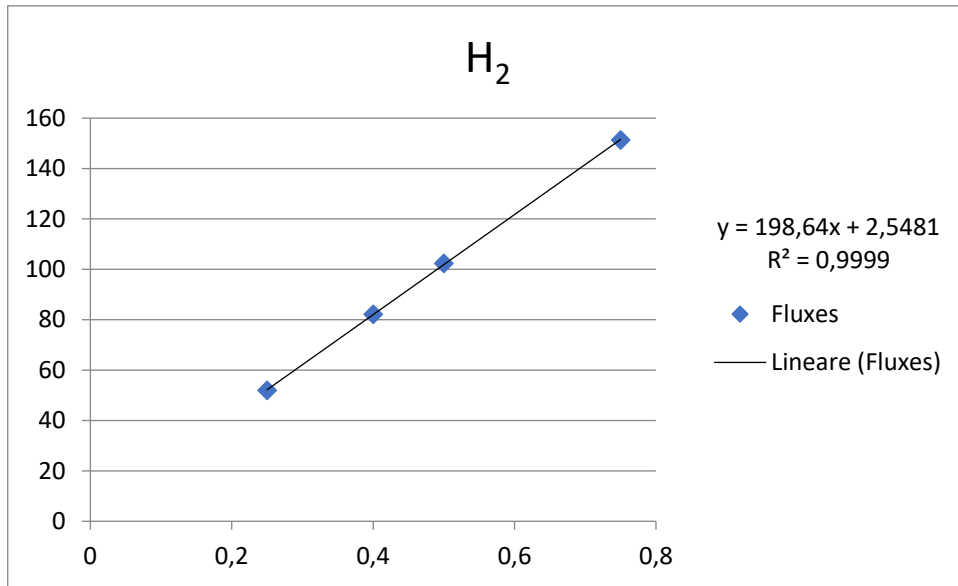


Figure 5. Calibration line of H₂ with H₂.

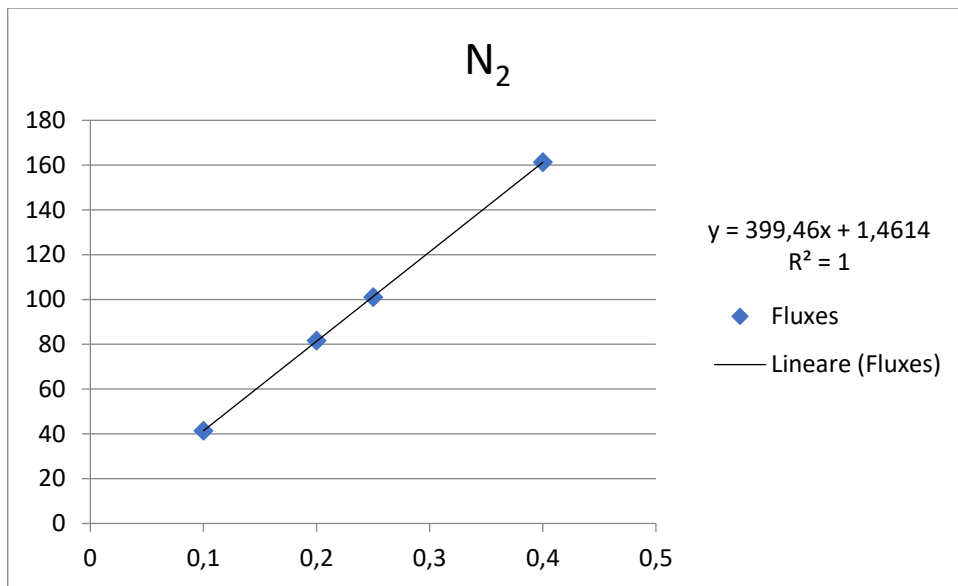


Figure 6. Calibration line of N₂ with N₂.

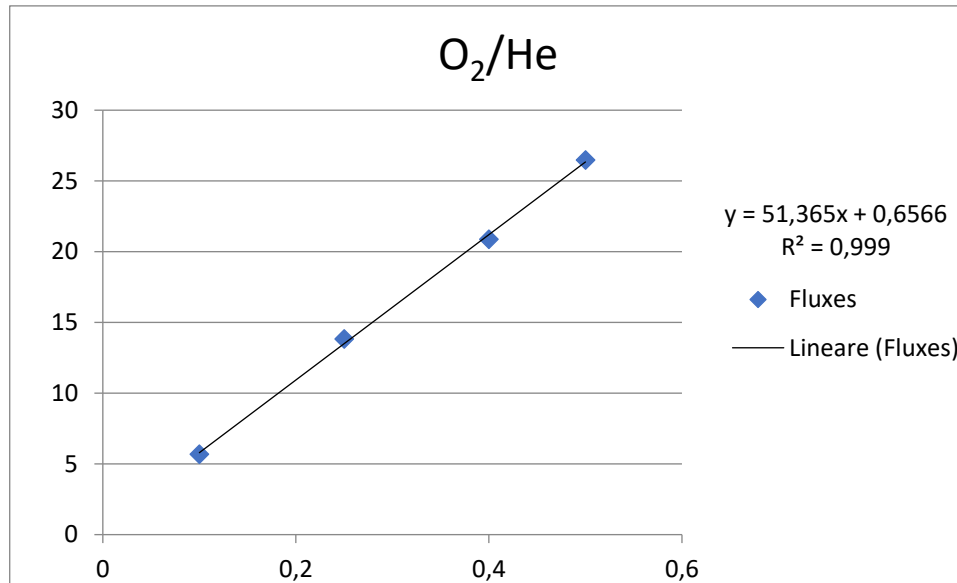


Figure 7. Calibration line of oxygen in helium with N_2 .

3.1.2 Reaction zone

The reaction zone starts from the valve V5. The lines are connected by a quadruple joint before the bypass valve V18 and in a triple joint before the valve V5. Downstream of the reactor, the gas can either flow directly into the analysis zone and/or in the vent line. The fixed bed reactor employed in the experiments is a quartz tube of 1.1 cm diameter and 27 cm length. At its bottom before the restriction, there is a porous separator which sustains the solid parts inside of the reactor itself.

The loading of the reactor strongly depends on the axial temperature profile of the electrical oven in which the reactor is located.

In this regard, the catalyst bed is put in the isothermal section of the oven: it is therefore necessary to determine the temperature profile of the reactor before performing experiments. The thermal profile of the reactor is obtained using two J-type thermocouples: one is fixed on the porous separator at the bottom of the reactor and connected to the oven, so as to maintain constant heat flux, the other is mobile along the reactor and generates the thermal profile.

The first rough measures are obtained loading the entire reactor volume with a solid inert (quartz grains). Once the isothermal zone is identified, the same measure is carried out by filling the isothermal zone with $\alpha\text{-Al}_2\text{O}_3$, so as to get closer to the thermal conductivity of

the real catalyst bed. Two profiles have been obtained, by imposing as set point temperatures the catalyst activation temperature (400 °C) and the reaction temperature (240 °C).

The isothermal zone covers 1.5 ÷ 2.5 cm from the porous separator. Being the catalyst bed 1 cm long, the length of the isothermal zone allows operations in reasonably isothermal conditions.

3.1.3 Product analysis zone

Downstream of the reactor, the gas merges into the by-pass line and flows towards the gas detector. Since the gas stream flowing through the gas detector must be at high temperature, the line connecting the bottom of the reactor to the gas detector is heated up and insulated. The instrument installed in the rig is a gas chromatograph (Pollution): it consists of two columns, operating at different temperatures and pressures, downstream of which four TCD (Thermal Conductivity Detectors) are present. The TCD senses changes in the thermal conductivity of the column effluent by means of a filament immersed into the carrier gas: when the gas sample enters the columns, the composition changes and so does the thermal conductivity, causing a variation of the filament temperature. As a result, the electrical conductivity is altered, triggering a change of the potential difference across the filament for the entire contact time between the gas sample and the filament. The TCD allows detection of compounds which have a considerable thermal conductivity difference from the carrier gas; helium is often employed as a carrier gas, mainly because it is inert, and it has a thermal conductivity about seven times higher than that of common organic gases.

The micro-GC analysis times is about 4 ÷ 5 minutes for analysis and the possibility to detect helium He, since argon Ar was used both as eluent and reference for the detectors. In this way, it was possible to use the He/O₂ mixture in order to provide analysis. The micro-GC scheme is shown below in the figure 8.

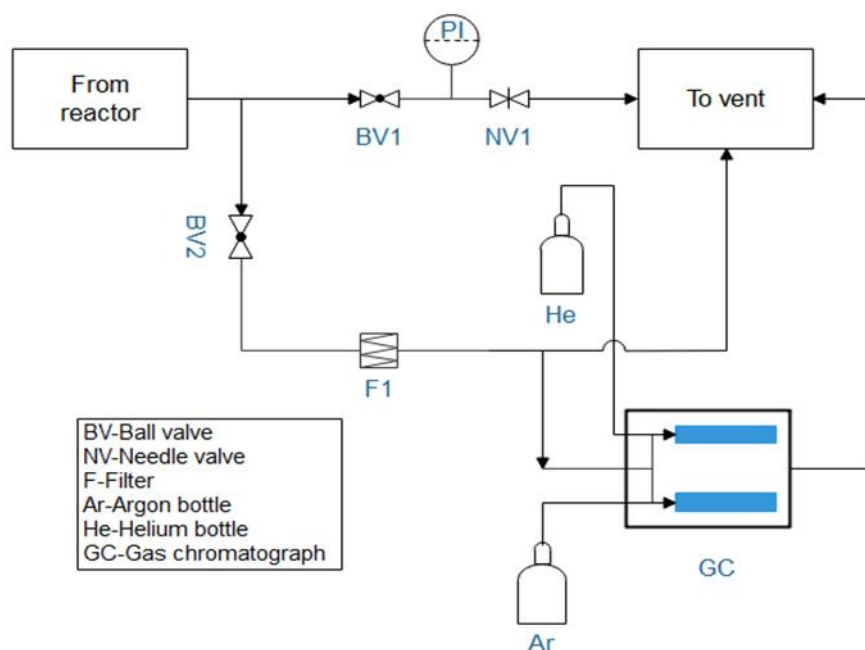


Figure 8. P&I scheme of the analysis section with Pollution Micro-GC.

Pollution micro-GC is equipped with two capillary columns, one coated with Molecular Sieve and the other with PoraPlot Q ®. Argon is used as eluent for Molecular Sieves (column A) while helium is used as eluent for PoraPlot (column B). During the thesis the Molecular Sieves (column A) is used only. Micro-GC is also equipped with a membrane filter that can trap the water that can damages the column. Water is very dangerous for the correct operation of the system, so a flash system is placed before the Molecular Sieve to ensure complete evaporation of the residual water and a pre-column with PoraPlot is placed before the column with Molecular Sieves. In the case of micro-GC, automatic sampling procedure was ensured by a pump. The pump ensures a flow equal to 10 ml/min of gas for each analysing column. In this configuration is possible to analyse the compounds of interest as helium, oxygen and nitrogen since it is detected in the column that use argon as reference.

- *Gas chromatograph configuration*

In a gas chromatographic analysis, gases are entrained by an eluent (He or Ar, in this case Ar) and enter the columns which contain the active phase (solid) that realise the real separation of the mixture components; this is done by exploiting the different affinity of

the gases to the active phase which physically adsorb on the solid in a reversible way. As the gas flow in the columns the components of the gas mixture will be separated and will leave the columns separately and detected. The more the gas is affine to the active phase the later it will be desorbed and the longer will be the retention time where with this term it is meant the time required to a specific gaseous component to leave the column. What is obtained is a chromatogram where on the abscissa is reported the time and on the ordinate axis is reported the intensity of the output signal in terms of electric potential (μV). The area under the peaks is proportional to the gas concentration. In the chromatogram for each substance a peak of intensity is realised in the output signal; in a good analysis each peak must be as much sharp as possible, and they should be well separated and not overlapped (Figure 9).

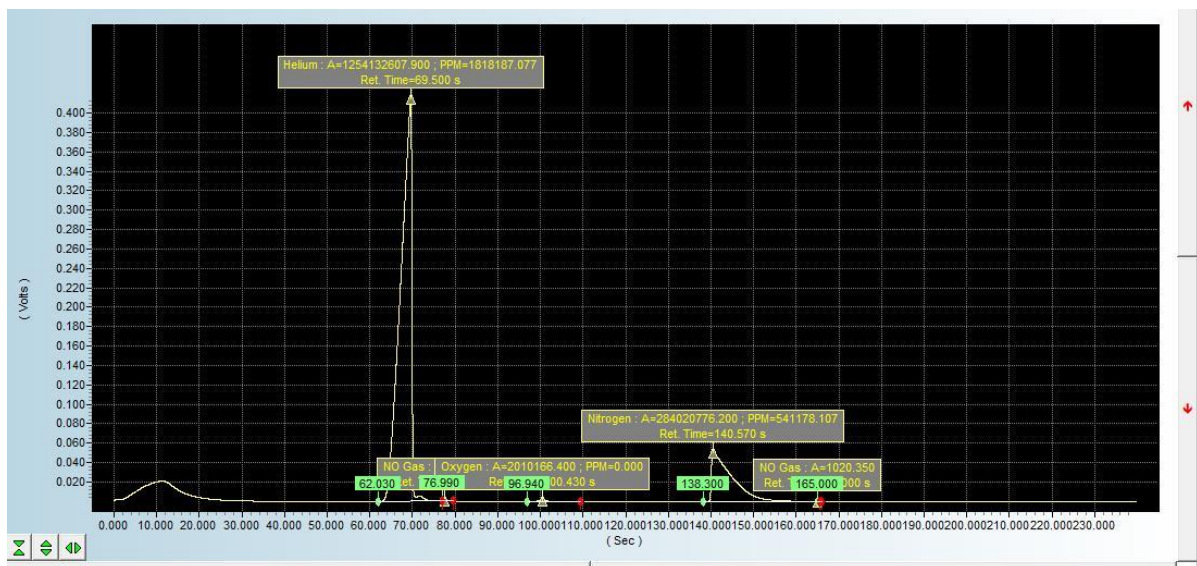


Figure 9. Example of output chromatogram from the Micro-GC analysis.

The output chromatogram can be modified by tuning the operative condition of the column in particular pressure and temperature in order to avoid overlapping and widening of the peaks. As a general rule high temperature will favour desorption of gases and reduce analysis time and makes peaks sharper while high pressure will favour absorption and makes analysis longer. Optimal operative conditions of the Micro-GC however are not defined a priori but must be chosen accordingly to the gaseous mixture and to the kind of columns used in terms of geometry and length. The best operative conditions ensure a good definition of the peaks and short analysis time are resumed in the tables below (Table 3, Table 4).

Table 3. Micro-GC properties.

Pollution® GCX	Column A	Column B
Active phase	Molecular Sieve	PoraPlot
Column geometry: diameter length functional material	320.00 µm 10 m 30 µm	320.00 µm 8 m 10 µm
Carrier	Ar	He
Detectors type	TCD	TCD
Detected species	O ₂ , N ₂ , CO	CO ₂ Pseudo (O ₂ , N ₂)

Table 4. Parameters of column A in the Micro-GC analysis.

Column Temperature	40°C
Injector temperature	55°C
Injector time	100 msec
Initial Pressure	120 kPa
Max filament temperature	350°C
Run time	220 sec
Back-Flush Time	10 sec

With the above operating conditions, the retention time of each compound are the following:

Table 5. Retention time for the detected compounds.

Components	Retention time
He	70 sec
O ₂	100 sec
N ₂	150 sec

- *Gas chromatograph calibration*

The output of the GC (*Gas Chromatograph*) is a variable potential signal which is sent to the CPU (*Central Processing Unit*), where it is processed and transformed into the so-called chromatogram: the latter consists of a profile with a number of peaks corresponding to different compounds which are present in the gas sample. The proportionality of the peak's area to the corresponding species concentration is governed by the following equation:

$$\frac{A_i}{C_i} \cdot f_i = \frac{A_{ref}}{C_{ref}} \quad (1)$$

Where: A_{ref} = area of the reference compound

C_{ref} = concentration of the reference compound

A_i = area of the i compound

C_i = concentration of i compound

Hence, to determine the concentration of the i species, it is necessary a reference compound whose concentration is constant and known throughout the experiments. The term f_i is the so-called *response factor*: it is the end point of the calibration process as it enables to relate the i species concentration (unknown) to the reference concentration (known).

Table 6. Cylinder composition used for the response factors.

Components	Concentration [%]
Ar	2.02
N ₂	15.01
CO	26.01
CH ₄	2.02
H ₂	54.94

The calibration is carried out by analysing samples of a product mixture, at known concentration, sent to the chromatograph from the *IDR2* line. The adopted reference species must be consistent both during calibration and during experiments and must be inert during the reaction. The product mixture of known concentration contains N₂ and Ar: the latter is chosen as reference species because it is also present in the reacting syngas mixture. However, as argon is detected only in column A. Once methane concentration is acquired from column A, where Ar is the reference. This procedure is named *internal standard method*. Sometimes the column does not share any of its compounds with the other columns, it becomes necessary to follow a different path in determining its species compositions. The so-called *external standard method* can be extended as side-check also to the other columns because it does not depend on any reference compound. It defines a linear relationship between peak area and composition:

$$A_i = m_i \cdot x_i + q_i \quad (2)$$

By collecting experimental data at different inlet gas compositions, it is possible to perform a linear regression obtaining the m_i and q_i values needed for the instrument calibration, without any dependence on reference species. Experimentally, the gas mixture of known composition if progressively diluted by co-feeding nitrogen: the gas analyses at different compositions should lie on a straight line crossing the origin. When available, the *internal standard method* is preferred: the other is highly sensible to alterations in flow rate and volume of the gas sample injected into the GC.

3.2 Experimental procedures

3.2.1 Catalyst preparation

The alumina support was purposefully stabilized with inactive cobalt aluminate species, following the procedure described in our recent work. Briefly, γ -Al₂O₃ pellets (Sasol Puralox[®], D_{pellet}= 300 μ m) were impregnated (incipient wetness impregnation, IWI, method) with an aqueous solution of Co(NO₃)₂·6H₂O (Sigma Aldrich, 98 wt.%) so to reach a Co loading of 5.7 wt.% (0.67 g_{salt}/ml_{solution}). Then, the sample was dried in static air at 120 °C for 1 h and calcined in static air at 900 °C for 4 h (heating rate: 1.5 °C/min). This treatment resulted in an evident color change from pink (cobalt nitrate) to blue as a consequence of the formation of cobalt aluminates (Figure 10). The obtained material will be referred in the following as Al₂O₃^(s). Cobalt used for the support stabilization is “sacrificial” because forms species (Co-aluminates) inactive in the CO hydrogenation as verified experimentally.

In order to prepare catalysts with active Co loading of around 18 wt.%, stabilized alumina was impregnated four times with an aqueous mixture of Co(NO₃)₂·6H₂O. Each impregnation step was followed by drying in static air at 120 °C for 2 h (heating rate: 2 °C/min) and calcination in static air at 500 °C for 4 h (heating rate: 2 °C/min). In the following, the catalysts will be named Co/Pt/Al₂O₃^(s). The sample is promoted with 0.1 wt.% of Pt.

The promotion of the catalysts with Pt is performed using the *Reverse Sequential Deposition Order* (RSDO) methods. In the RSDO method, Pt is deposited onto the Al₂O₃^(s) support using an aqueous solution of 3.4 wt.% Pt(NH₃)₂·(NO₂)₂ in NH₄OH (Sigma Aldrich, 99 wt.%). The impregnation step is followed by drying in static air at 120 °C for 2 h (heating rate 2 °C/min) and calcination at 500 °C for 4 h (heating rate 2 °C/min).



Figure 10. Image of the $\gamma\text{-Al}_2\text{O}_3$ support stabilized with CoAl_2O_4 species.

3.2.2 Reactor preparation

The catalyst bed must be placed into the reactor's isothermal section, which starts above the porous separator and 1 cm of glass wool. In the passivation experiments, the catalyst bed is made of a pure catalyst while during the activity tests the pure catalyst few grams is diluted with 2 gr of $\alpha\text{-Al}_2\text{O}_3$ for a total length of 2.6 cm. The $\alpha\text{-Al}_2\text{O}_3$ powder is employed as a thermal diluent to ensure a uniform temperature distribution in the catalyst bed and avoid potential hot spots. Also, from the chemical point of view this allotropic form of alumina has low porosity and thus appropriate inertness in the reaction. The reactor filling is completed with glass balls for the remain length until the inlet of the gases fed to the reactor itself.

3.2.3 Catalyst reduction and passivation

The reduction of the catalyst is effectuated with heating ramp of 2 °C/min ramp in order to achieve at ambient pressure for 17 h under a flow of pure H_2 (83.33 Ncc/min/g_{cat}).

After the reduction step, the temperature is cooled down up to room temperature under a flow of pure nitrogen. Once the temperature of 27 °C is reached, a gas flow of 1% of O_2/He is fed into the reactor at different GHSV of 11, 20, 30.5, 40 and 50 Ncc/min/g_{cat}. The amount of O_2 adsorbed on the catalyst is monitored by the microGC.

3.3 Catalyst characterization

3.3.1 ICP-MS

The ICP-MS (*Inductively Coupled Plasma-Mass Spectrometry*) is an analytic tool capable of identifying the percent elemental composition of the calcinated samples. The analyses on this instrument have been performed, so as to verify that the actual amounts of active phase and promoter on the catalysts were the ones expected during preparation. Experimentally, the sample is dissolved into concentrated nitric acid or, when noble metals are present, concentrated hydrochloric acid; if the dissolution is not complete some phosphoric acid is added. Subsequently, the sample is introduced in a microwave oven (*Multiwave 3000, Anton-Paar*) which operates at 240 °C and 60 atm: the solution is then cooled down and nebulized so that a quadrupole achieves the separation, based on the mass/charge ratio. Finally, a detector downstream measures the concentration of the elements.

3.3.2 BET

The BET analysis – in honour of the scientists *Brunauer, Emmet and Teller* – coupled with the BJH – *Barret, Joyner, Halenda* – provides information on the morphological and structural properties of the catalysts, by studying nitrogen adsorption-desorption dynamics at -196 °C. Surface area, pore volume and pore size distribution (between 200 and 0.5 nm) can be determined with this technique. The instrument used for the measurements is a *Micrometrics Tristar 3000*, which evaluates the volumetric adsorption-desorption varying the relative pressure ($P/P^0 = 0.001-0.98$). The following expression correlates the relative pressure with the adsorbed gas volume:

$$\frac{1}{V_{ads} \cdot \left(\frac{P^0}{P} - 1\right)} = \frac{C - 1}{V_m C P^0} + \frac{1}{V_m C} \quad (3)$$

Where:

P = partial pressure of the adsorbed gas

P^0 = vapour pressure

V_{ads} = adsorbed gas volume at STP

V_m = volume of a monolayer

C = non-dimensional constant, dependent of the adsorption enthalpy

The surface area is linked to the monolayer volume by this equation:

$$S_{tot} = \frac{V_m N_{AVO} A}{V_{ads}} \quad (4)$$

being A the cross-section area of the molecule gas probe (0.162 nm^2).

The so-called Kelvin equation Eq.6 correlates the relative pressure to the curvature radius of the meniscus formed by the adsorbed gas (r_m), which is in turn associated to the average pore radius (r_p) by Eq.7.

$$\ln\left(\frac{P}{P^0}\right) = -\frac{2\gamma V_{liq}}{RT} \frac{1}{r_m} \quad (5)$$

$$r_p = r_m + t \quad (6)$$

3.3.3 XRD

X-ray diffraction is a useful tool to identify the atomic and molecular structure of a crystal: it provides information on the crystalline phases of the catalyst sample. The emitted X-radiation impacts on the catalyst surface, producing a constructive interference with the vibration frequencies of the catalyst only when the so-called Bragg's law is satisfied:

$$n\lambda = 2d \cdot \lambda \sin\theta \quad (7)$$

Where: λ = wave length of the radiation

θ = existing angle between the crystalline plane and the radius

d = inter-planar spacing

The result is a spectrum whose peaks are linked to the crystallite size (D) by the so-called Scherrer equation:

$$D = \frac{k\lambda}{\beta_{hkl} \cos\theta} \quad (8)$$

Where k is a constant and β is a parameter associated with the half-height length of the peak of the reflection hkl . The instrument used for the measurements is a Bruker D8 Advanced which employs a Cu-K α X-ray source. XRD measurements is performed on the same samples in the 2θ range of 20–80° with 0.05 °C step and 12.5 s as step time at room temperature (25 °C): the starting time is fixed at 0 s and on the 2θ axis corresponds to 20 °, so the θ value is 10 °, with null φ .

As the obtained spectrum represent the composition of the whole catalytic material, it becomes necessary to operate a difference between spectra to identify the active phase: in particular, the support spectrum is subtracted from the catalyst spectrum.

3.3.4 H_2 -TPR

H_2 -temperature programmed reduction (H_2 -TPR) analyses are carried out both on the calcined (exp a) and reduced (exp b) catalysts using a Micromeritics Thermoquest TPDRO1100 instrument. The instrument is equipped with a thermal conductivity detector (TCD) located downstream the reactor after a soda lime steam trap. It's possible to have two types of sample: a calcined sample and reduced one. The first sample is calcined and was heated from 40 to 1050 °C (heating rate: 15 °C/min) under a flow of 5.15 vol.% H_2 in Ar (600 cm³(STP)/ min/gcat, Sapio). The second sample could be reduced in situ at 400 °C (heating rate: 2 °C/min) for 17 h using 83 cm³(STP)/min/gcat of pure H_2 (Sapio, 99.995 mol.%) and then cooled to 40 °C in Ar (Sapio,99.999 mol.%). Then, the reactor is purged with a stream of 5.15 vol.% H_2 in Ar, and further heated to 1050 °C (heating rate: 15 °C/min). H_2 consumption in this latter heating step correlates with the amount of cobalt

which remains unreduced after the treatment in H₂ at 400 °C. The degree of reduction (DOR_{TPR}, [%]) from Co₃O₄ to Co⁰ is calculated by applying the following equation:

$$DOR_{TPR} = \left(1 - \frac{n_{H_2}^{red}}{n_{H_2}^{cal}}\right) \cdot 100 \quad (9)$$

where $n_{H_2}^{red}$ is the amount of H₂ consumed during the TPR analysis of the reduced catalyst and $n_{H_2}^{cal}$ is the amount of H₂ consumed during the TPR analysis of the calcined catalyst.

3.3.5 H₂-Chemisorption

The information of Co⁰ dispersion of the catalyst is collected through H₂ chemisorption experiments using the same instrumentation of TPR experiments. In a quartz reactor is placed 300 mg of sample and it is reduced in situ at temperature of 400 °C and pressure of 1 atm with the heating rate of 2 °C/min for 17 h under a pure H₂ flow (5000 cm³ (STP)/h/gcat). Then flowing Ar at 400 °C and 1 atm for 17 h in H₂ (5000 cm³ (STP)/h/gcat) for 2 h and cooling to 100 °C, successive pulses of H₂ (246 μL/pulse) are passed over the catalyst. The total amount of chemisorbed H₂ ($mol_{H_2}^{chemi}$) is calculated from the difference between the peak area obtained during the saturation experiment and the areas of the peaks in the absence of the chemisorption phenomena. Assuming the stoichiometry Co:H equal to 1, the cobalt metal dispersion (D, %) is calculated as following:

$$D = \frac{mol_{H_2}^{chemi} \cdot 2}{mol_{Co}^{tot} \cdot DOR_{magnet}} \cdot 100 \quad (10)$$

Where $mol_{H_2}^{chemi}$ is the total amount of H₂ chemisorbed in the experiment and mol_{Co}^{tot} is the amount of active Co loaded on the catalyst.

Chapter 4

Results and Discussion

4.1 Characterization of the calcined Co/Pt/Al₂O₃^(s) catalyst

The textural properties of the γ -Al₂O₃ pellets, the stabilized Al₂O₃^(s) support and the Al₂O₃^(s) support promoted with Pt (Pt/Al₂O₃^(s)) are shown in Table 1 with those of the calcined catalyst Co/Pt/Al₂O₃^(s). Both BET area and pore volume of the stabilized alumina are about 30% lower than those of the starting γ -Al₂O₃ pellets. Al₂O₃^(s) and Pt/Al₂O₃^(s) show the same values of surface area and pore volume, thus indicating no effect of the Pt-impregnation step and following thermal treatments on the textural properties of the support. In Co/Pt/Al₂O₃^(s) catalyst the values are lower compared to those of the Pt/Al₂O₃^(s) support. The decrease of the surface area is linked to a decrease of the pore volume as well, whereas the pore diameter is rather constant and is in the range 12-14 nm. The BJH pore diameter is similar for the stabilized support and catalysts. The pore size distributions (not shown) show a narrow pore size distribution in the mesopore range (Table 1).

The actual Co loading of the catalyst obtained by ICP-MS analyses, which is inclusive of the cobalt used for support stabilization, is in good agreement with the target value (Table 1).

Table 1. Textural properties of the samples.

	S_{BET}^(a) [m ² /g]	V_p^(a) [cm ³ /g]	d_p^(b) [nm]	Actual Co content^(c) wt. %	Actual Pt content^(c) wt. %
Al₂O₃	145	0.43	12	-	
Al₂O₃^(s)	102	0.37	14	5.57 ± 0.11	-
Pt/Al₂O₃^(s)	102	0.37	14	5.60 ± 0.10	0.141 ± 0.004
Co/Pt/Al₂O₃^(s)	59	0.20	14	22.80 ± 0.59	0.110 ± 0.002

^(a)BET measurements; ^(b)BJH analysis; ^(c)ICP-MS analysis

Figure 1 shows the diffraction patterns of the $\text{Al}_2\text{O}_3^{(s)}$ and $\text{Co/Pt/Al}_2\text{O}_3^{(s)}$ samples. The calcination at 900 °C used for the preparation of the $\text{Al}_2\text{O}_3^{(s)}$ pellets causes the interaction of cobalt-containing species with the alumina support, resulting in the formation of cobalt aluminates (main peaks at 31.5 and 37°) whose diffraction peaks overlap with those of Co_3O_4 . However, cobalt aluminates can be distinguished from Co_3O_4 by H_2 -TPR analysis (Figure 2). In this regard, in contrast with the Co_3O_4 reduction peak that starts at 250 °C and is completed at 350- 400°C, that representing the Co aluminates (likely CoAl_2O_4 species) starts at higher temperatures over 800 °C because hardly reducible species (1). This is in line with the TPR profile obtained with the $\text{Al}_2\text{O}_3^{(s)}$ support (Figure 2) and confirms that the stabilized support is constituted only by CoAl_2O_4 species and does not contain any Co oxides species. In the presence of Pt, the reduction peak of the CoAl_2O_4 species results shifted to a lower temperature of 700 °C (TPR profile of the $\text{Pt/Al}_2\text{O}_3^{(s)}$ support in Figure 2). This temperature is much higher than that used at our activation conditions of the catalyst during the reduction (see Chapter 3). The diffraction pattern of the catalyst shows peaks sharper than those of $\text{Al}_2\text{O}_3^{(s)}$, which can be associated with the presence of a new Co_3O_4 phase in the $\text{Co/Pt/Al}_2\text{O}_3^{(s)}$ catalyst. In this regard, CoO peaks are not detectable on the diffraction pattern of the catalyst, thus indicating that after the calcination step carried out at 500°C in static air only Co_3O_4 species are formed (Figure 1). The average size of Co_3O_4 crystallites, estimated by applying the Scherrer equation to the most intense Co_3O_4 diffraction peak at $2\theta = 37.06^\circ$ (see Chapter 3), is 20 nm from which a Co^0 crystallite size of 15 nm can be determined (see Chapter 3).

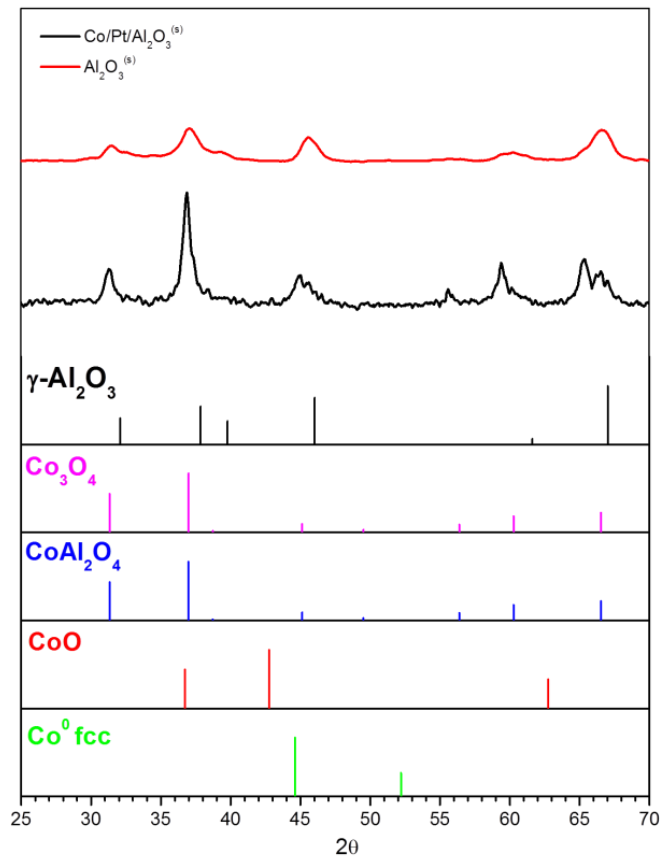


Figure 1. XRD patterns of $\text{Al}_2\text{O}_3^{(s)}$ and $\text{Co/Pt/Al}_2\text{O}_3^{(s)}$ samples. The reference patterns of $\gamma\text{-Al}_2\text{O}_3$, Co_3O_4 , CoAl_2O_4 , CoO and Co^0 are also shown.

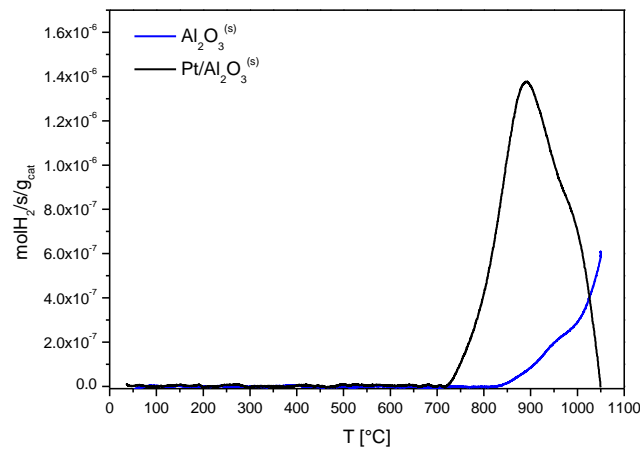


Figure 2. TPR profiles of the stabilized support ($\text{Al}_2\text{O}_3^{(s)}$, blue line) and of the stabilized supported after Pt-impregnation ($\text{Pt/Al}_2\text{O}_3^{(s)}$, black line).

The results obtained from H_2 -TPR measurements performed on the calcined $\text{Co/Pt/Al}_2\text{O}_3^{(s)}$ catalyst (*exp(a)*) are shown in Figure 3. The first peak with a maximum at 301°C is associated with the reduction of Co_3O_4 species to CoO . The following peak with a

maximum at 511 °C is associated with the reduction of CoO to metallic Co. Eventually, the last peak with maxima at 827 and 923 °C involves the reduction of Co^{x+} species highly interacting with the support. These latter may be the CoAl₂O₄ species used for the support stabilization, as suggested by the TPR profile of Al₂O₃^(s) reported in Figure 3, and/or the Co-Al mixed species formed during H₂-TPR via interaction at high temperature (>800 °C) of partially reduced Co-species (likely CoO) and the support.

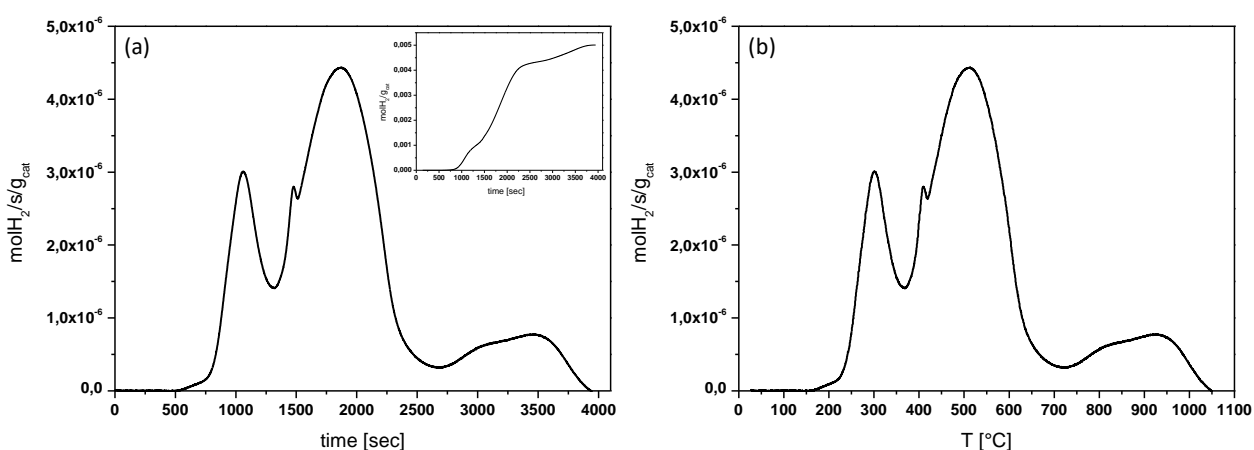


Figure 3. TPR profiles of the calcined Pt/Al₂O₃^(s) catalyst as a function of the time. Inset: integral H₂ consumptions.

The amount of H₂ consumed during the H₂-TPR analysis can be determined from the integral curve of the TPR profile of the calcined Co/Pt/Al₂O₃^(s) catalyst plotted as a function of the time (Figure 3(a)). Knowing the stoichiometry of the reduction reactions from Co₃O₄ to CoO (eq. (1)) and then to Co⁰ (eq. (2)) and the reduction from CoAl₂O₄ to Co⁰ (eq. (4)), it is possible to compare the amounts of cobalt oxide and cobalt aluminates in the sample with the theoretical values (Table 2). The global reaction from Co₃O₄ to Co⁰ is also shown as eq. (3). Theoretical values of all the species are estimated knowing that the calcined catalyst contains 11.6 wt.% of CoAl₂O₄ and 24.6 wt.% of Co₃O₄. The remaining is γ-Al₂O₃.



Table 2. Theoretical amounts of Co oxides and Co aluminates species present on the catalyst and theoretical values of H₂ needed to reduce them.

$\text{molCo}_3\text{O}_4/\text{g}_{\text{cat}}^{\text{th}}$	$10.2 \cdot 10^{-4}$
$\text{molCoAl}_2\text{O}_4/\text{g}_{\text{cat}}^{\text{th}}$	$6.6 \cdot 10^{-4}$
$\text{molH}_2/\text{g}_{\text{cat}}^{\text{th}}$ (eq. (3))	$40.8 \cdot 10^{-4}$
$\text{molH}_2/\text{g}_{\text{cat}}^{\text{th}}$ (eq. (4))	$6.6 \cdot 10^{-4}$
$\text{molH}_2/\text{g}_{\text{cat}}^{\text{th}}$ (tot)	$47.4 \cdot 10^{-4}$
$\text{molCoO}/\text{g}_{\text{cat}}^{\text{th}}$ (eq. (1))	$30.6 \cdot 10^{-4}$
$\text{molCo}^0/\text{g}_{\text{cat}}^{\text{th}}$ (eq. 4.2)	$30.6 \cdot 10^{-4}$

The total amount of H₂ consumed in the TPR profile of the calcined Co/Pt/Al₂O₃^(s) catalyst, determined by the integral curve from 0 to 4000 sec ($\text{molH}_2/\text{g}_{\text{cat}}^{\text{exp}}$ (tot) = $50.0 \cdot 10^{-4}$), well correlates with the total amount of H₂ needed to reduce all cobalt species present on the catalyst ($\text{molH}_2/\text{g}_{\text{cat}}^{\text{th}}$ (tot) = $47.4 \cdot 10^{-4}$) (Table 3).

The theoretical amount of CoAl₂O₄ species used for the support stabilization ($\text{molCoAl}_2\text{O}_4/\text{g}_{\text{cat}}^{\text{th}}$ = $6.5 \cdot 10^{-4}$) also well correlates with the experimental value obtained by integrating the high-temperature peaks of the H₂-TPR profile from 2700 to 4000 sec ($\text{molCoAl}_2\text{O}_4/\text{g}_{\text{cat}}^{\text{exp}}$ = $6.5 \cdot 10^{-4}$) (Table 3). This indicates that the high-temperature peaks are only related to those species used for the support stabilization.

In line with these results, the experimental value of Co₃O₄ species present on the catalyst ($\text{molCo}_3\text{O}_4/\text{g}_{\text{cat}}^{\text{th}}$ = $10.9 \cdot 10^{-4}$), which is calculated by the subtraction of the total amount of H₂ consumed during H₂-TPR ($\text{molH}_2/\text{g}_{\text{cat}}^{\text{exp}}$ (tot) = $50.0 \cdot 10^{-4}$) and that consumed for the reduction of the Co aluminate species ($\text{molH}_2/\text{g}_{\text{cat}}^{\text{exp}}$ (3° and 4° Peaks) = $6.5 \cdot 10^{-4}$), is close to the theoretical value of $10.2 \cdot 10^{-4}$ ($\text{molH}_2/\text{g}_{\text{cat}}^{\text{th}}$ (1° and 2° Peaks) = $43.5 \cdot 10^{-4}$). Notably, the amount of H₂ consumed in the first peak is in line with the assumption that the first peak is related to the reduction from Co₃O₄ to CoO ($\text{molH}_2/\text{g}_{\text{cat}}^{\text{exp}}$ (1° peak) = $10.2 \cdot 10^{-4}$) and the second peak with the reduction from CoO to Co⁰ ($\text{molH}_2/\text{g}_{\text{cat}}^{\text{exp}}$ (2° peak) = $33.3 \cdot 10^{-4}$) (Table 3).

Table 3. Calculated amounts of Co oxides and Co aluminates species present on the catalyst and theoretical values of H₂ needed to reduce them.

molH ₂ /g _{cat} ^{exp} (tot)	50.0·10 ⁻⁴
molH ₂ /g _{cat} ^{exp} (3° and 4° Peaks)	6.5·10 ⁻⁴
molCoAl ₂ O ₄ /g _{cat} ^{exp}	6.5·10 ⁻⁴
molH ₂ /g _{cat} ^{exp} (1° and 2° Peaks)	43.6·10 ⁻⁴
molCo ₃ O ₄ /g _{cat} ^{exp}	10.9·10 ⁻⁴
molH ₂ /g _{cat} ^{exp} (1° peak)	10.2·10 ⁻⁴
molH ₂ /g _{cat} ^{exp} (2° peak)	33.3·10 ⁻⁴
molCoO/g _{cat} ^{exp} (eq. (1))	33.3·10 ⁻⁴
molCo ⁰ /g _{cat} ^{exp} (eq. (1))	33.3·10 ⁻⁴

4.2 Characterization of the catalyst reduced at 400 and 300 °C

The TPR profile of the Co/Pt/Al₂O₃^(s) catalyst reduced in-situ at 400 °C under a flow of pure H₂ (5000 Ncc/h/g_{cat}) for 17 h (*exp(b)*) is also shown in Figure 4. After reduction, the peaks assigned to the reduction from Co₃O₄ to CoO and to Co⁰ completely disappear. Accordingly, a degree of reduction of 100% is calculated (DOR_{TPR}, see Chapter 3).

The peaks observed at high temperature associated with the reduction of Co-aluminates match closely with those observed in the TPR profiles of the calcined catalyst (*exp a*) (Figure 3). This suggests that the cobalt species interacting with the support “survive” the 17 hours reduction in H₂ at 400 °C. However, the interactions between the support and cobalt occur only at the high temperatures reached during H₂-TPR and cannot take place either during the catalyst activation step or during FTS runs (1).

The dispersion (*D*, see Chapter 3) of the reduced Co/Pt/Al₂O₃^(s) catalyst measured after H₂-chemisorption is 11.6% from which a value of 8.3 nm of Co⁰ crystallites size is calculated. This value is lower than that that estimated from XRD analysis by applying Scherrer equation (see Chapter 3, eq. (9)), possibly due to an overestimation of the starting average Co oxides crystallite size, due to the subtraction of the patterns or due to the fact that X-ray is not able to detect very small cobalt oxides particles thus shifting the average value of

crystallites size to high values. The Co^0 crystallites size of 8.3 nm is close to that obtained with in-situ X-ray measurements by Fratolocchi et al. (2) with the same catalyst.

The H_2 -TPR analysis carried out on the $\text{Co/Pt/Al}_2\text{O}_3^{(s)}$ sample reduced in-situ at 300°C is also shown in Figure 4. As in the case of the reduction carried out at 400°C , the peak assigned to the $\text{Co}^{3+} \rightarrow \text{Co}^{2+}$ reduction completely disappears, indicating that residual Co_3O_4 species are not present after a reduction treatment at 300°C in pure H_2 for 17h. This result is in line with the fact that the transition from CoO to Co^0 is known to be the *facile* $\text{Co}^{3+} \rightarrow \text{Co}^{2+}$ reduction step among all the Co reduction steps (2). At variance, the CoO to Co^0 reduction peak is still partially present, indicating an incomplete reduction of the sample. Indeed, a lower extent of reduction (DOR_{TPR} , see Chapter 3) of 83% with respect to the sample reduced at 400°C is calculated. The fraction of unreduced CoO particles is possibly related to the smallest particles present on the catalyst (Figure 5), which are known to be hardly reducible. The peaks observed at high temperature associated with the reduction of Co-aluminates are still present.

The dispersion (D , see Chapter 3) of the $\text{Co/Pt/Al}_2\text{O}_3^{(s)}$ catalyst reduced at 300°C is 5.93%, from which a value of 16.2 nm of Co^0 crystallites size is calculated. The dispersion is lower than that of the sample reduced at 400°C due to (i) a lower degree of reduction of the catalyst and (ii) a bigger average Co^0 particles size (Figure 5).

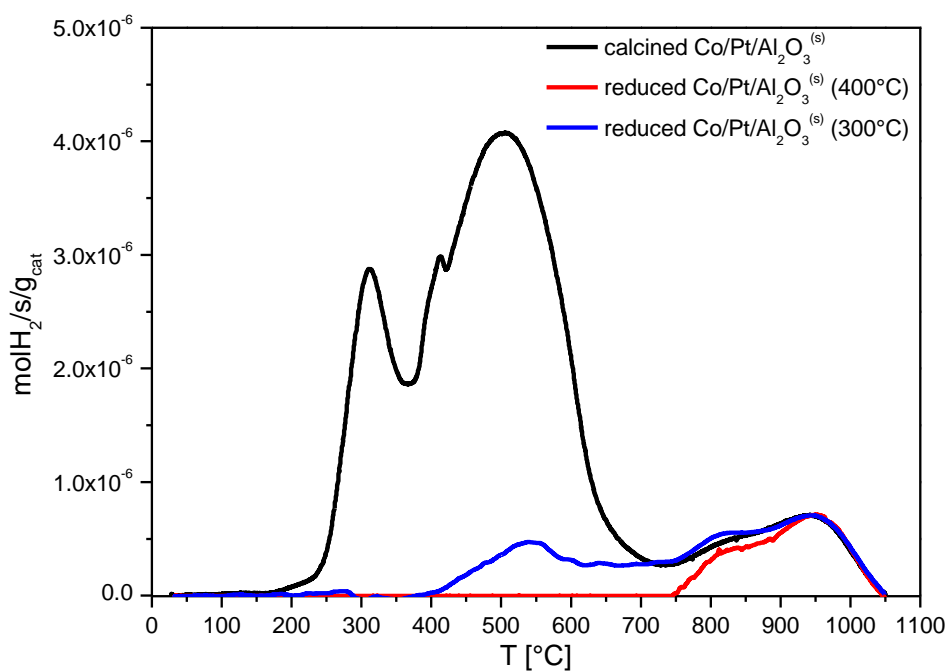


Figure 4. TPR profiles of the calcined $Pt/Al_2O_3^{(s)}$ catalyst (black line) and of the $Pt/Al_2O_3^{(s)}$ catalyst reduced at 400 °C (red line) and 300 °C (blue line) as a function of the temperature.

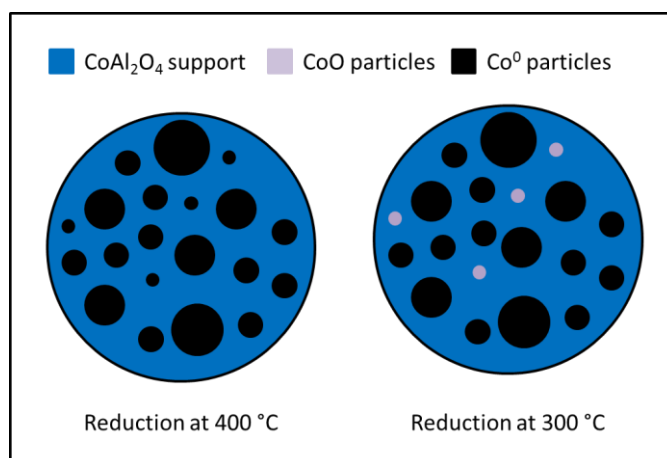


Figure 5. Simplified scheme of the structure of the catalyst reduced at 400 and 300 °C.

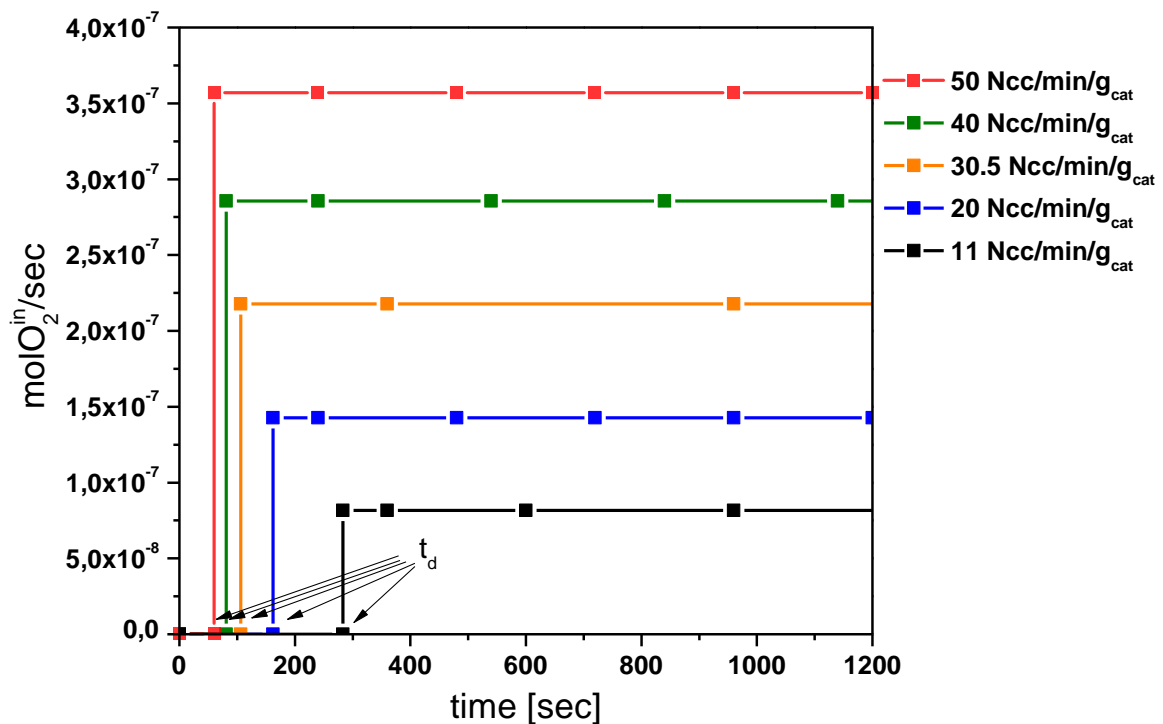
4.3 Catalyst passivation

The effect of the space velocity of O_2 on the catalyst passivation treatment has been investigated by keeping constant the catalyst loading at 0.96 gr and the O_2 concentration at 1% mol/mol). As reported in Chapter 3, the catalyst is initially reduced at 400 °C for 17 h under a flow of pure H_2 (83.33 Ncc/min/gcat), then it is cooled down with a flow of pure N_2 (83.33 cc/min/gcat) up to around 27-28 °C and eventually passivated under different flows of 1% O_2/He (11, 20, 30.5, 40 and 50 Ncc/min/gcat). The temperature of the catalyst, which is measured in the middle of the catalytic bed, is monitored during the entire passivation treatment.

Prior to the experiments, blank tests have been performed by replacing the catalyst bed with $\alpha-Al_2O_3$ powder and by feeding the used 1% O_2/He flows (11, 20, 30.5, 40 and 50 Ncc/min/gcat). As shown in Figure 6, a delay time (t_d) is observed from when we feed the gas into the reactor to when this gas is detected by the MicroGC. This is related to the quite large volumes between the mass flow controller and the analyzer.

Table 4. Delay time (t_d) for the different experiments.

GHSV _{O₂/He} [Ncc/min/g _{cat}]	t_d [sec]
11	295
20	163
30.5	106
40	81
50	65

Figure 6. Blank tests carried out at different GHSV of 1%O₂/He (11, 20, 30.5, 40, 50 Ncc/min/g_{cat}).

The O₂ molar flow (molO₂^{out}/sec) monitored during the passivation treatment of the catalyst at GHSV_{O₂/He} of 11, 20, 30.5, 40 and 50 Ncc/min/g_{cat}, is shown in Figure 7. By increasing the space velocity, the O₂ consumption rate increases. This trend is explained with the fact that increasing space velocity leads to shorter residence time of the reactant into the reactor. The total amount of O₂ consumed (molO₂^{cons}) during the entire passivation treatment is represented by the area plotted in Figure 8, which is determined by the difference between the inlet and outlet O₂ molar flow (molO₂^{cons}/sec = molO₂ⁱⁿ/sec - molO₂^{out}/sec).

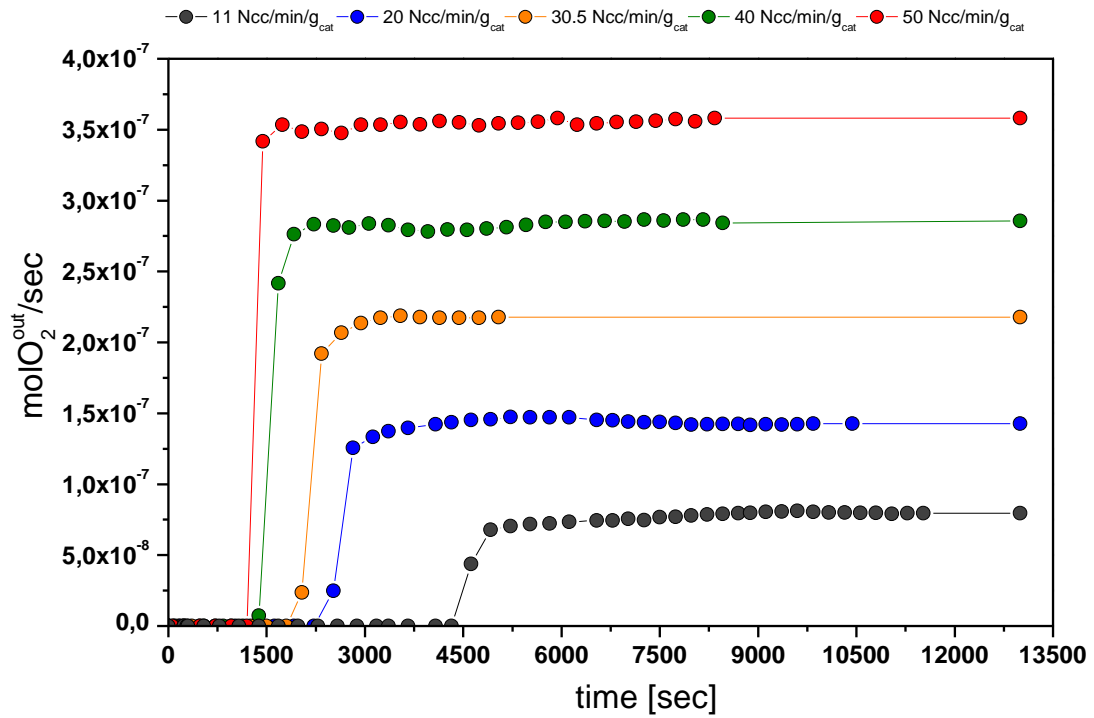


Figure 7. Outlet molar flow of O₂ monitored during the passivation treatment at different GHSV_{O₂/He} of 11 (black circle), 20 (blue circle), 30.5 (orange circle), 40 (green circle) and 50 (red circle) Ncc/min/g_{cat}, as a function of the time.

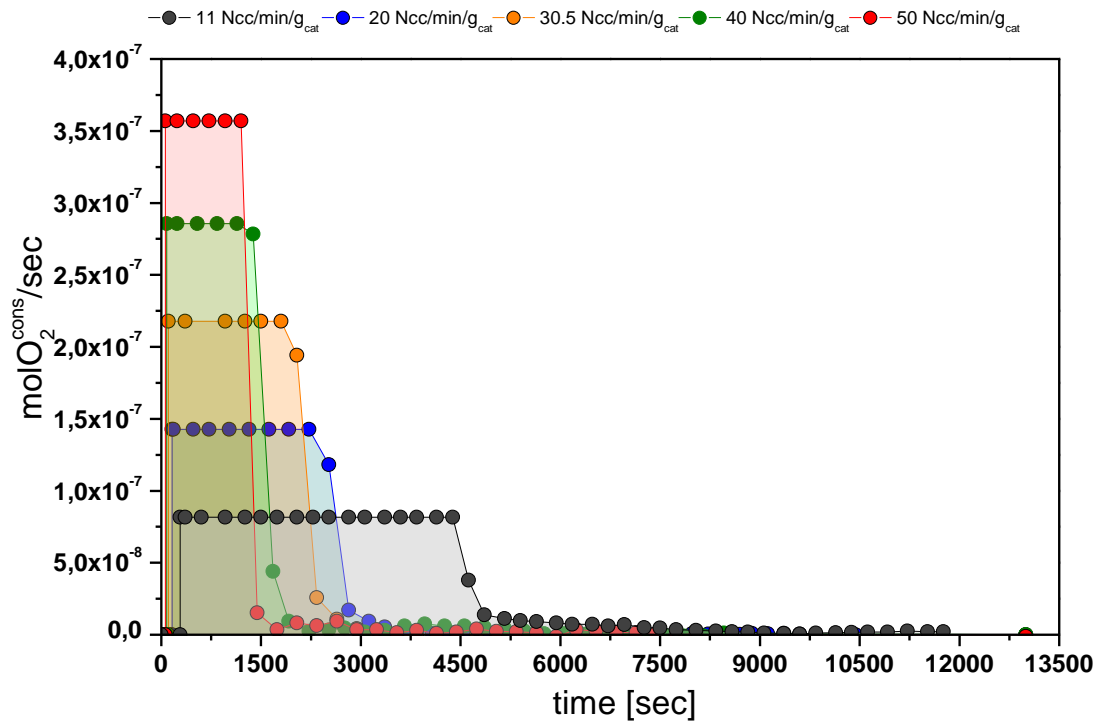


Figure 8. Amount of O₂ consumed during the passivation treatment at different GHSV_{O₂/He} of 11 (black circle), 20 (blue circle), 30.5 (orange circle), 40 (green circle) and 50 (red circle) Ncc/min/g_{cat}, as a function of the time.

The values of total amount of O_2 consumed ($\text{mol}O_2^{\text{cons}}$) as a function of the different $\text{GHSV}_{O_2/He}$ are shown in Figure 9. They are almost constant in the range of $4\text{--}5 \cdot 10^{-4}$ for all the $\text{GHSV}_{O_2/He}$ investigated. Each test has been repeated at least four times. Thus, error bars are also reported for each test. Higher errors are obtained at lower $\text{GHSV}_{O_2/He}$ probably due to the fact that the mass flow controller works in a low and less precise range of flows.

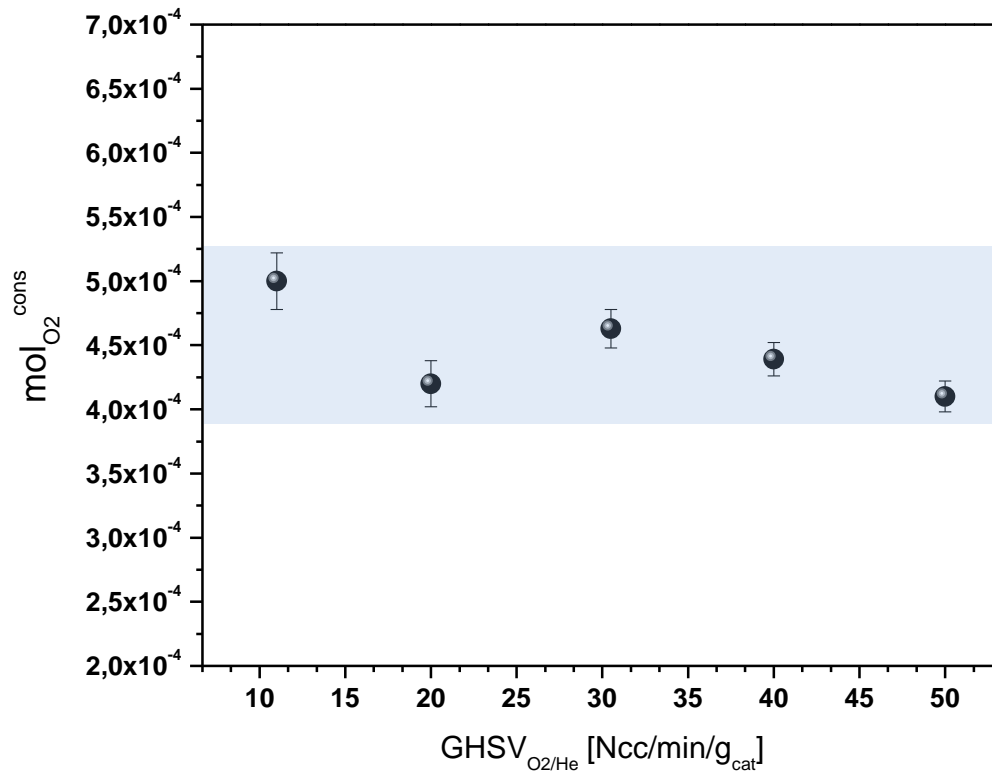


Figure 9. Total moles of O_2 consumed during the passivation treatment at different $\text{GHSV}_{O_2/He}$.

During the passivation process, the temperature of the catalyst is monitored (Figure 10). The temperature remains almost constant during the passivation process carried out at $\text{GHSV}_{O_2/He}$ of 11 Ncc/min/g_{cat}, thus excluding the occurrence of measurable hot spots. Accordingly, the temperature gradient, which is defined as the difference between the maximum and the minimum temperature reached during passivation, is 2 °C, respectively. Stronger temperature gradients are measured at higher $\text{GHSV}_{O_2/He}$: 5.3, 8.5, 11.9 and 14 °C at 20, 30.5, 40 and 50 Ncc/min/g_{cat}, respectively. A linear trend is observed (Figures 11).

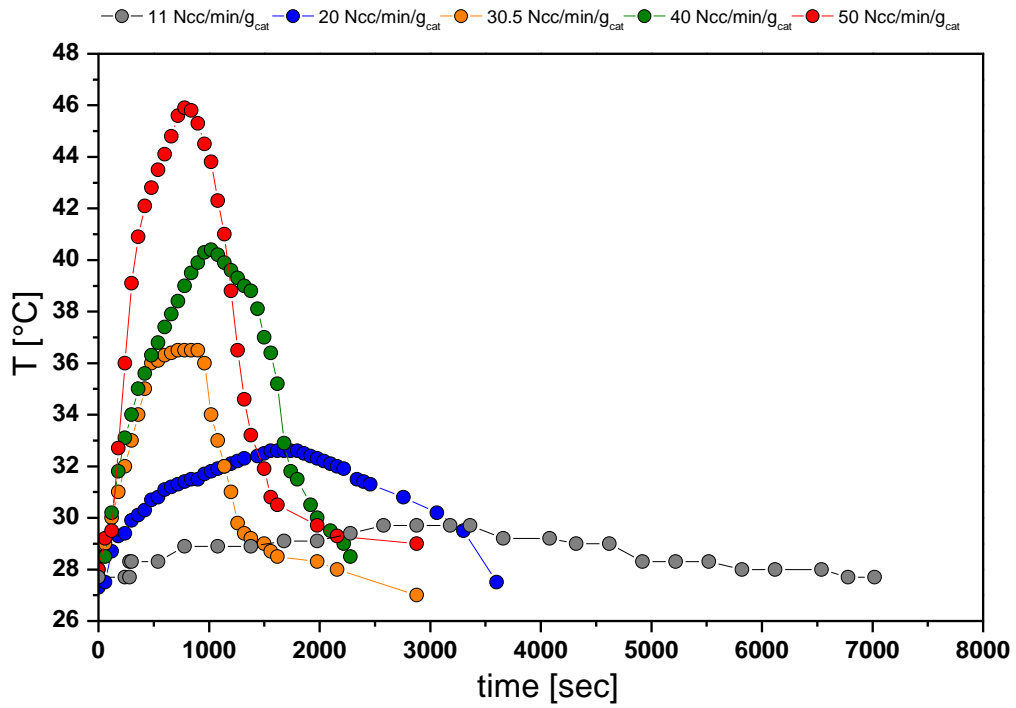


Figure 10. Temperature of the catalyst during the passivation treatment at different $GHSV_{O_2/He}$ of 11 (black circle), 20 (blue circle), 30.5 (orange circle), 40 (green circle) and 50 (red circle) $Ncc/min/g_{cat}$, as a function of the time.

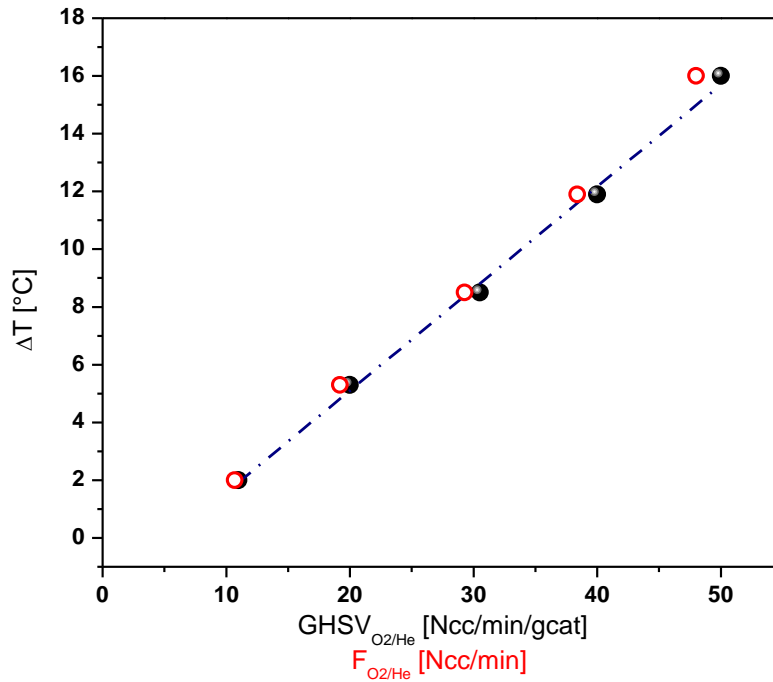


Figure 11. Temperature gradient measured at the centerline of the catalyst bed during the passivation treatment at different $GHSV_{O_2/He}$ and F_{O_2} .

In order to better understand the nature of the temperature gradients measured during passivation, different experiments have been carried in a wide range of O₂ flows (Figure 12). As clearly shown in Figure 12, the temperature gradient linearly depends on the flow of O₂ fed into the reactor. Even if almost negligible (~3%), higher errors are obtained at higher O₂ flow, due to the fact that increasing O₂ flow the increase of the temperature is instantaneous (Figure 10), thus leading to a greater measurement error.

Interestingly, there is no correlation between the different temperature gradients and the total amount of O₂ consumed during passivation, which, as shown in Figure 9 are almost constant.

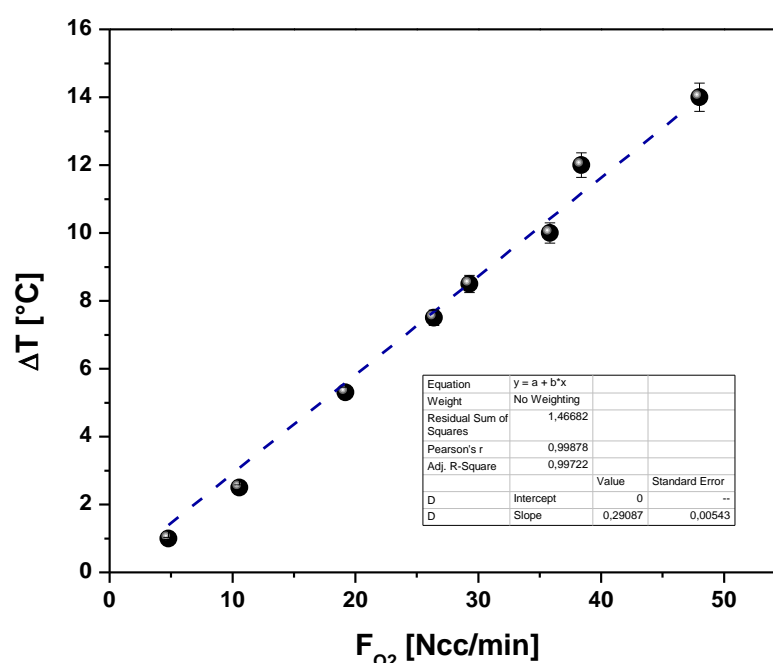


Figure 12. Temperature gradient measured at the centerline of the catalyst bed during the passivation treatment at different F_{O₂}.

In order to determine the oxidation state of cobalt on the passivated catalyst, H₂-TPR analysis is performed immediately after the sample is unloaded from the reactor. As shown in Figure 13, only one peak with a maximum at 260 °C is detected. This peak has also a very small shoulder at 100 °C and occurs at lower temperatures with respect to the first peak of the calcined catalyst representing the reduction of Co₃O₄ species to CoO (maximum at 300 °C). In our opinion, this peak can be associated to the reduction of the

CoO species during passivation to Co^0 . In this regard, it could not be the reduction of Co_3O_4 species to CoO because the consecutive reduction peak from CoO to Co^0 reduction is not present. This result is also in line with (3).

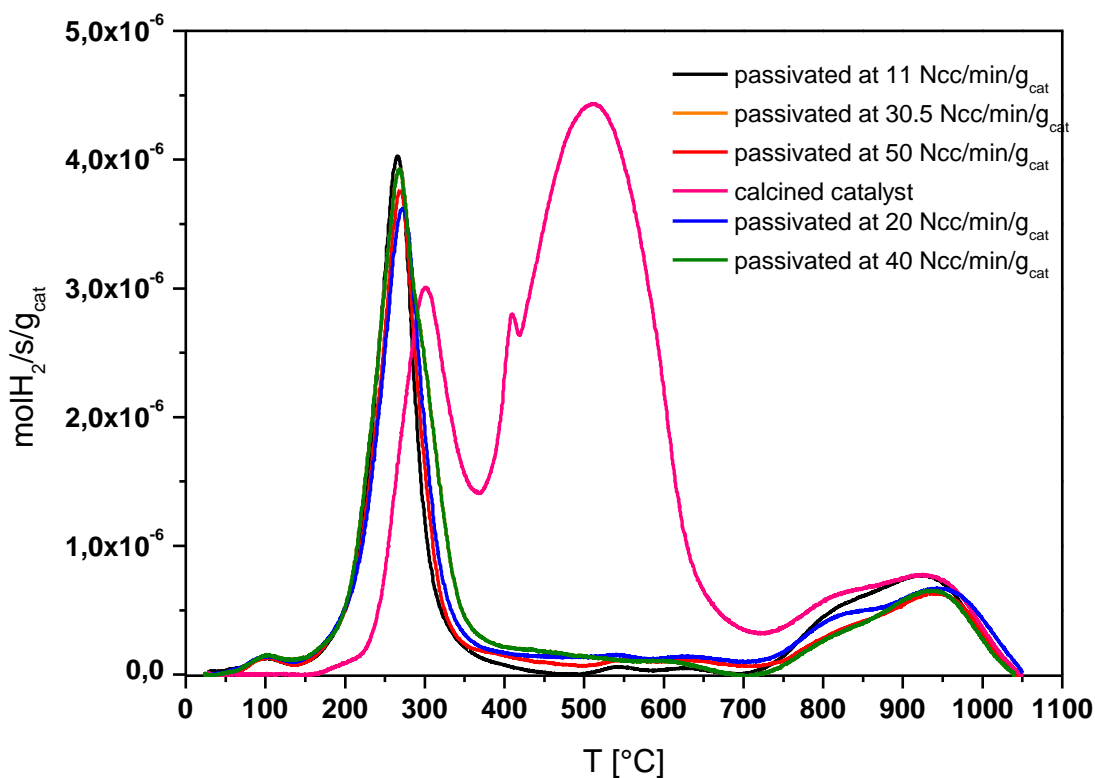


Figure 13. H_2 -TPR on the passivated samples at different $\text{GHSV}_{\text{O}_2/\text{He}}$ as a function of the temperature.

The CoO to Co^0 reduction peak is shifted to lower temperatures with respect to the calcined sample, probably due to the fact that this reduction step is now promoted by the presence of unpassivated Co^0 species which act as active centers for the H_2 spillover occurring during cobalt reduction. It is known that on the calcined catalyst the CoO reduction starts only when all the Co_3O_4 species are reduced to CoO (4). This is due to the fact that the Co_3O_4 species capture all the molecules of H_2 available. The scenario is quite different with the passivated catalyst in which no Co_3O_4 species are present and the CoO reduction can start at low T (Figure 14).

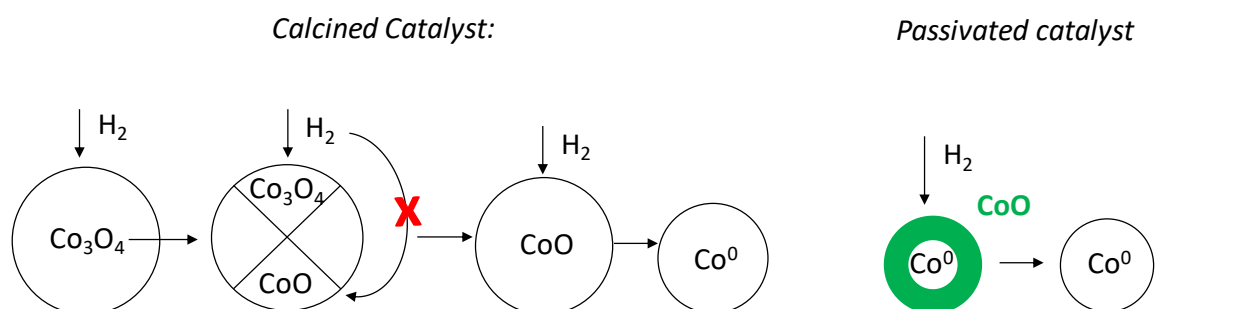


Figure 14. Sketch of the mechanism of the reduction process of the calcined catalyst (on the left) and of the passivated catalyst (on the right).

From the total amount of H₂ consumed under the first peak of the passivated samples and knowing the stoichiometry of the CoO reduction reaction (eq. (2)), we can calculate the moles of CoO present on the passivated sample by H₂-TPR. This value can be compared with the amount of O₂ consumed ($\text{molO}_2/\text{g}_{\text{cat}} = \text{molCoO}/\text{g}_{\text{cat}}$) during passivation. Interestingly, similar values are obtained for all the passivated catalysts: $(\text{molCoO}^{\text{formed during pass}}/\text{g}_{\text{cat}}) / (\text{molCoO}^{\text{reduced during H}_2\text{-TPR}}/\text{g}_{\text{cat}}) = 1$. This confirms our hypothesis on the formation of CoO species during passivation.

The last peaks with maxima at 827 and 923 °C involving the reduction of the CoAl₂O₄ species used for the support stabilization are still present. This points out that these species are not affected by the passivation treatment. Accordingly, the amount of CoAl₂O₄ species present on the passivated catalyst ($\text{molCoAl}_2\text{O}_4/\text{g}_{\text{cat}}^{\text{th}} = 6.0 \cdot 10^{-4}$) obtained by integrating the high-temperature peaks of the H₂-TPR profile as a function of the time well correlates with the value obtained with the calcined catalyst ($\text{molCoAl}_2\text{O}_4/\text{g}_{\text{cat}}^{\text{exp}} = 6.5 \cdot 10^{-4}$).

Among the procedures adopted for the catalyst passivation, we focused on the passivation performed with the lowest GHSV_{O₂/He} investigated (11 Ncc/min/g_{cat}), so to ensure limited temperature gradients into the reactor in case we had to passivate larger quantities of catalyst.

XRD analysis of the catalyst passivated with a GHSV_{O₂/He} of 11 Ncc/min/g_{cat} revealed the existence of CoO and Co⁰ species (Figure 15). The Co₃O₄/CoAl₂O₄ peaks are those belonging to the stabilized support. While the Co⁰ peaks are well distinguishable (main diffraction peak at $2\theta = 44.5^\circ$), the CoO peaks (main diffraction peak at $2\theta \sim 42.9^\circ$) are vague indicating a layer thickness close to the lower detection limit for crystallites sizes being around 2 nm. The hardly detectable CoO peaks in XRD analysis might also be due to a partially amorphous CoO shell as reported in literature (5).

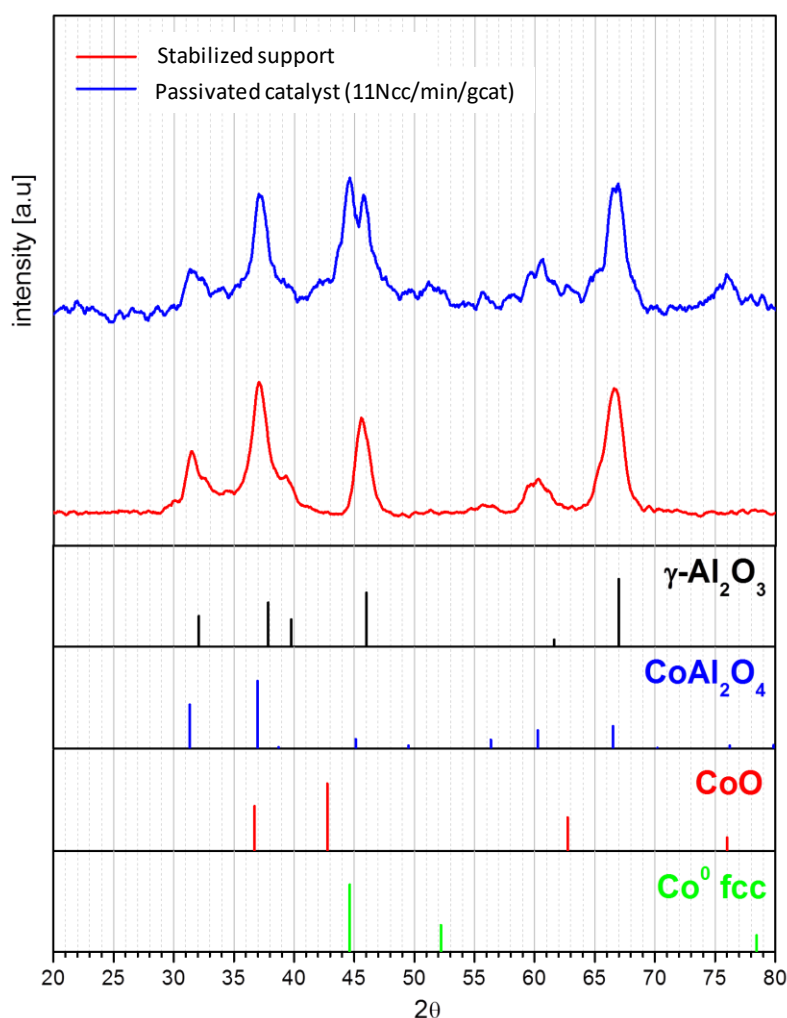


Figure 15. XRD patterns of $\text{Al}_2\text{O}_3^{(s)}$ and the $\text{Co/Pt/Al}_2\text{O}_3^{(s)}$ sample passivated with a $\text{GHSV}_{\text{O}_2/\text{He}}$ of $11\text{Ncc/min/g}_{\text{cat}}$. The reference patterns of $\gamma\text{-Al}_2\text{O}_3$, Co_3O_4 , CoAl_2O_4 , CoO and Co^0 are also shown.

Notably, H_2 -TPR analysis are performed on the passivated catalyst after one week of static air exposure and no differences are obtained, thus indicating that the passivation layer does not increase and protects the Co metal phase during this period of time.

The degree of reduction and the dispersion of the passivated $\text{Co/Pt/Al}_2\text{O}_3^{(s)}$ catalyst after the reduction process carried out at 400 and 300 °C under a flow of pure H_2 (83.33 $\text{Ncc/min/g}_{\text{cat}}$) are calculated. Interestingly, the passivated catalyst is completely reduced at both these temperatures. Furthermore, also the Co^0 dispersion measured after H_2 -chemisorption is the same obtained with the reduction of the calcined catalyst. This result is extremely relevant since it indicates that the passivation process does not change the morphology of the catalyst.

4.4 Catalytic testing at high pressure lab-scale FT plant

Co/Pt/Al₂O₃^(s) catalyst and Co/Pt/Al₂O₃^(s) catalyst passivated at 11 Ncc/min/g_{cat} have been tested in the FTS using a fixed bed tubular reactor (1.1 cm ID) after dilution with α-Al₂O₃ pellets of the same granulometry so as to prevent local hot-spots (catalyst: alumina = 1:4, v/v). More details on the reactor and on the used lab-scale apparatus can be found in (6) and references therein. In order to activate the Co/Pt/Al₂O₃^(s) catalyst, the sample has been reduced in situ in H₂ (Sapio, 99.995 mol.%) at 400 °C (heating rate= 2 °C/min) and atmospheric pressure for 17 h at a space velocity of 5000 cm³(STP)/h/g_{cat}. On the contrary, the passivated Co/Pt/Al₂O₃^(s) catalyst has been reduced in situ in H₂ (Sapio, 99.995 mol.%) at 300 °C (heating rate= 2 °C/min) and atmospheric pressure for 18 h at a space velocity of 5000 cm³(STP)/h/g_{cat}. The latter has been reduced 18 h instead of 17 h in order to ensure the same total time under H₂ flow.

Catalytic runs have been carried out at relevant process conditions: T = 200 °C, P = 25 bar, H₂/CO inlet molar ratio = 2.0, GHSV = 6410 cm³(STP)/h/g_{cat}, inerts (N₂ + Ar) in the feed = 24 vol.%.

The unconverted reactants and the full spectrum of products were measured by on-line and off-line gas-chromatography. Details on the product collection and analysis procedures can be found elsewhere (7). In order to collect representative activity data, both the catalysts studied in this work were tested for more than 90 h. In order to check the achievement of steady state conditions, multiple data at the same experimental condition have been collected for more than 48 consecutive hours. The CO conversion (X_{CO} [%], eq. (5)) and the selectivity to the main FTS products (S_i [%], eq. (7)) have been calculated as in eqs (5) and (6).

$$X_{CO} [\%] = 1 - \frac{F_{CO}^{out}}{F_{CO}^{in}} \cdot 100 \quad (5)$$

$$S_i [\%] = \frac{F_i^{out} \cdot n_i}{\sum_i^{NP} (F_i^{out} \cdot n_i) + F_{CO_2}^{out}} \cdot 100 \quad (6)$$

F_i^{out} is the molar productivity of i^{th} hydrocarbon species, n_i is the carbon atom number of the i^{th} species and NP is the number of the hydrocarbon products (paraffins C₁–C₄₉ and

olefins C₂–C₁₇) identified at the reactor outlet. The selectivity to carbon dioxide has been calculated as in eq. (7):

$$S_{CO_2} [\%] = \frac{F_{CO_2}^{out}}{F_{CO}^{in} - F_{CO}^{out}} \cdot 100 \quad (7)$$

Carbon balances, calculated as moles of C contained in the reaction products divided by the moles of CO converted, always closed within $\pm 5\%$.

The catalysts are found to be very stable with Time on Stream (T.o.S.) in terms of catalyst activity and selectivity (Figure 16).

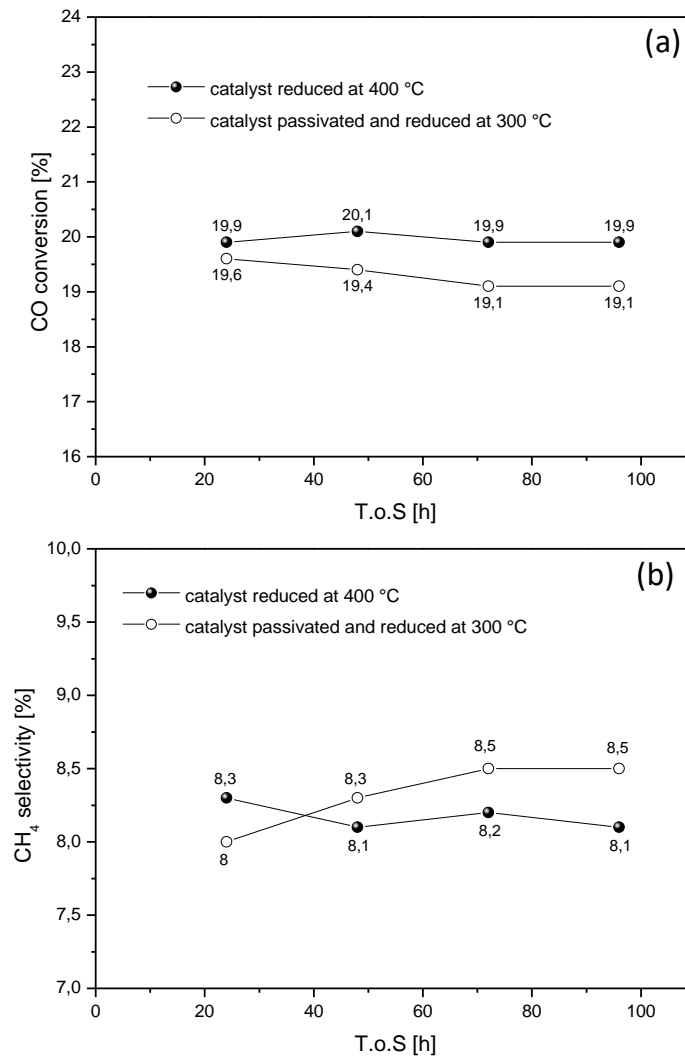


Figure 16. Catalysts stability with Time on Stream (T.o.S.) in terms of (a) catalyst activity and (b) selectivity $T = 200\text{ °C}$, $P = 25\text{ bar}$, $H_2/CO = 2.0\text{ mol/mol}$, $GHSV = 6410\text{ cm}^3(\text{STP})h^{-1}g_{cat}^{-1}$, inerts in the feed ($N_2 + Ar$) = 24 vol.%.

Figure 17 shows the steady-state CO conversion values measured with the catalysts at 200 °C, 25 bar, H₂/CO inlet molar ratio= 2.0, GHSV= 6410 cm³(STP)/h/g_{cat}, inerts (N₂ + Ar) in the feed= 24 vol.% after around 70 h on stream. The selectivities to methane, carbon dioxide, C₅₊ and C₂₅₊ hydrocarbons are also shown. Notably, the catalysts show the same performances in the FTS. In particular, the CH₄ selectivity is around 8%, the CO₂ selectivity is close to 0.3%, and the selectivity to C₂₅₊ and C₅₊ is 14.3 and 76.9%, respectively.

This is well evident also in the Anderson-Schulz-Flory (ASF) plots shown in Figure 18. Both distributions show the typical positive and negative deviations from the ideal linear distribution for methane and C₂ hydrocarbons, respectively, and a change of slope at a carbon number around 8. The chain growth probability for the C₁₅₊ species ($\alpha_{C_{15+}}$) is 0.877 for both the catalysts.

In line with the previous results, also the olefin to paraffin ratio trend is similar for both the catalysts.

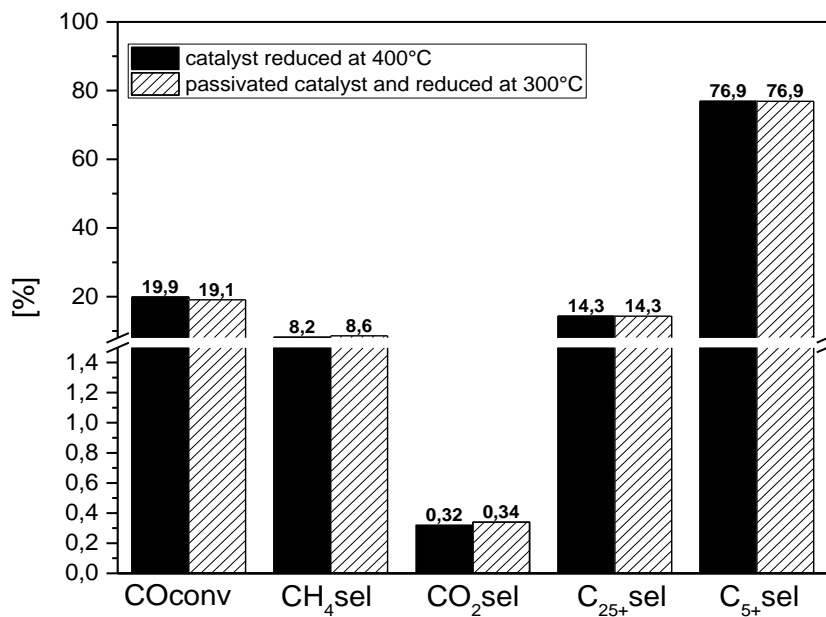


Figure 17. CO conversion and selectivity to main FT products measured with CoDEG/Al₂O₃^(s) and Co/Al₂O₃^(s) catalysts. O.C.: T= 200 °C, P = 25 bar, H₂/CO = 2.0 mol/mol, GHSV = 6410 cm³(STP)/h/g_{cat}, inerts in the feed (N₂ + Ar) = 24 vol.%, T.o.S.≈ 90 h.

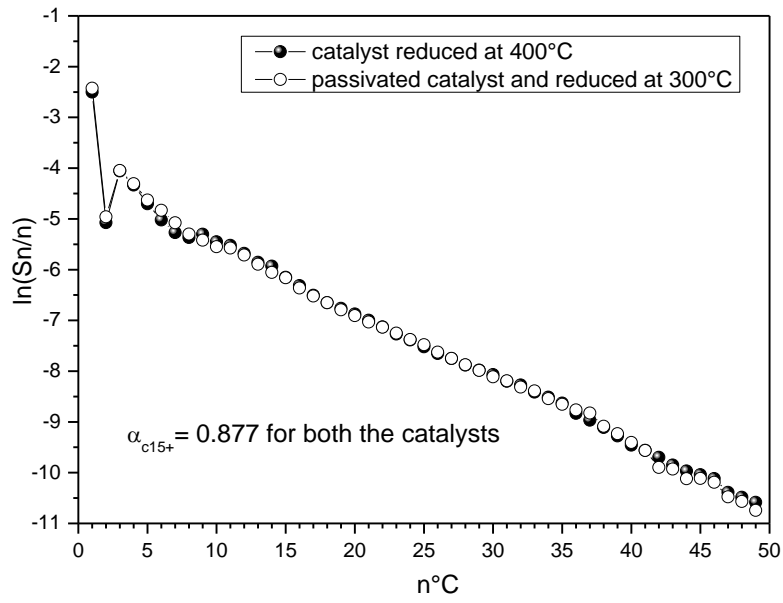


Figure 18. ASF distributions of the catalysts as a function of the carbon number (n).

Process conditions as in Figure 17.

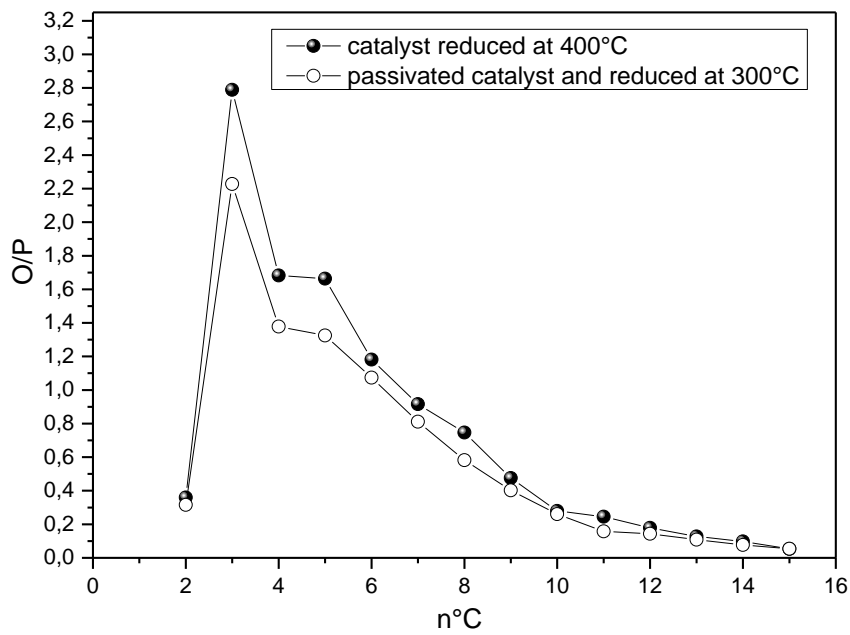


Figure 19. O/P ratio of the catalysts as a function of the carbon number (n).

Process conditions as in Figure 17.

Bibliography

1. L. Fratalocchi, C.G. Visconti, L. Lietti, G. Groppi, E. Tronconi, E. Roccaro and R. Zennaro. 2016, *Catal. Sci. Technol.*, Vol. 6, pp. 6431-6440.
2. L. Fratalocchi, C.G. Visconti, L. Lietti, N. Fischer, M. Claeys. submitted to *Cat. Sci. Technol.*
3. M. Wolf, N. Fischer and M. Claeys. 2016, *Catal. Tod.*, Vol. 275, pp. 135–140.
4. L. Fratalocchi, C.G. Visconti, L. Lietti, N. Fischer, M. Claeys. 2018, *Appl. Catal. A Gen.*, Vol. 556, pp. 92–103.
5. T.C. Rojas, J.C. Sánchez-López, M.J. Sayagués, E.P. Reddy, A. Caballero, A. Fernández. 1999, *J. Mater. Chem.*, Vol. 9, pp. 1011–1017.
6. C.G. Visconti, M. Mascellaro. 2013, *Catal. Today* , Vol. 214 , pp. 61–73.
7. C.G. Visconti, L. Lietti, P. Forzatti, R. Zennaro. 2007, *Appl. Catal. A Gen.* , Vol. 330.

Conclusions

Passivation of highly air sensitive transition metal catalysts is often used to preserve reduced or spent catalysts to allow transfer of samples from the reactor vessel to conventional characterization instruments. The passivation treatment can be also used when the operative conditions adopted during the catalyst activation cannot be reached in the same reactor adopted for the reactivity tests for plant manufacturing limitations. For instance, the temperatures commonly reached (400–450 °C) during the reduction of a Fischer-Tropsch catalyst are significantly higher than those adopted during the reaction (200–240 °C).

In this thesis work, the passivation treatment has been studied in detail in order to compare the performances of a cobalt-based FT catalyst reduced at 400 °C and passivated in a dedicated reactor and eventually transferred into the reactor used for the FTS and re-reduced at a significantly lower temperature of 300 °C, with those of the same catalyst reduced at 400 °C in the same reactor used for the FTS.

The calcined catalyst has been characterized in detail. The Co phases found on the calcined sample are Co_3O_4 and CoAl_2O_4 species. The latter are those belonging to the stabilized support. When the sample is reduced at 400 °C for 17 h under a flow of pure H_2 , all the Co_3O_4 species are converted into Co^0 . In line with the fact that CoAl_2O_4 species are known to be hardly reducible, these species are not reduced at our activation conditions. At lower reduction temperature of 300 °C, the extent of reduction is lower because of the presence of unreduced CoO smallest particles. Accordingly, the Co^0 dispersion is lower than that of the sample reduced at 400 °C as well as the number of Co^0 sites active in the FTS.

The results obtained during the passivation treatment show that by increasing the gas hourly space velocity of 1% O_2/He , the oxygen consumption rate increases due to the shorter residence time into the reactor, while the total amount of O_2 consumed is almost constant. All tests are repeated at least four times, showing excellent reproducibility. Interestingly, the temperature gradients measured at the center of the catalyst bed increase with the flow of O_2 used. This aspect is relevant from an industrial point of view, due to the fact that large amounts of catalyst are used and thus high flow rates of O_2 are involved. For this reason, the lowest GHSV_{O_2} of 11 $\text{Ncc}/\text{min}/\text{g}_{\text{cat}}$ is deeply investigated.

Analyzing all the passivated samples, we found that the Co phase formed after passivation is CoO , in line with the literature. The CoO reduction peak is shifted to lower temperatures if compared with that

of the calcined sample, due to the fact that no Co_3O_4 species are present. The latter is known to hinder the CoO reduction. The passivated catalyst reduced at $300\text{ }^\circ\text{C}$ has a degree of reduction of 100%. Also the Co^0 dispersion reaches the same value of the catalyst reduced directly at $400\text{ }^\circ\text{C}$. The effectiveness of the passivation treatment is also supported by the stability of the passivated catalyst after the exposure to air for one week. Accordingly, no changes are found in the sample after this period of time.

Concerning the results obtained in terms of catalyst reactivity, the same performances in the FTS expressed both in terms of activity and selectivity are obtained with the catalyst reduced in-situ at $400\text{ }^\circ\text{C}$ and the catalyst reduced at $400\text{ }^\circ\text{C}$ and passivated in a different dedicated reactor and eventually transferred into the reactor used for the FTS and re-reduced at $300\text{ }^\circ\text{C}$.